

LIBRARY Michigan State University

This is to certify that the

dissertation entitled

Perpendicular Giant Magnetoresistance in Thin Films with Microfabricated Superconducting Top Contacts

presented by

ROBERT DOUGLAS SLATER

has been accepted towards fulfillment of the requirements for

Ph D degree in Physics

Mutuate Musel

Date 10/25/01

PLACE IN RETURN BOX to remove this checkout from your record.

TO AVOID FINES return on or before date due.

MAY BE RECALLED with earlier due date if requested.

DATE DUE	DATE DUE	DATE DUE
		

6/01 c:/CIRC/DateDue.p65-p.15

PERPENDICULAR GIANT MAGNETORESISTANCE IN THIN FILMS WITH MICROFABRICATED SUPERCONDUCTING TOP CONTACTS

By

ROBERT DOUGLAS SLATER

A DISSERTATION

Submitted to
Michigan State University
in partial fulfillment of the requirements
for the degree of

DOCTOR OF PHILOSOPHY

Department of Physics and Astronomy

2001

ABSTRACT

PERPENDICULAR GIANT MAGNETORESISTANCE IN THIN FILMS WITH MICROFABRICATED SUPERCONDUCTING TOP CONTACTS

Bv

ROBERT D. SLATER

A new method to measure the position of a domain wall in a thin film is proposed. By fabricating micron-size superconducting top contacts to produce micron size areas of perpendicular current flow in exchange bias spin valves (EBSVs) of Co₉₁Fe₉ and Ni₈₄Fe₁₆, the position of a domain wall can be measured using the giant (G) magnetoresistance (MR) effect.

Exchange bias spin valves have the form: antiferromagnet (AF) /ferromagnet (F) /non-magnetic (N) /ferromaget (F). For the purposes of this study the AF was Fe₅₀Mn₅₀, F was Co₉₁Fe₉ or Ni₈₄Fe₁₆, and N was Cu. The AF layer serves to fix the magnetization of the adjoining F layer in one direction. The other F layer is then free to reverse with applied magnetic field. The GMR effect produces a large change in resistance when the F layers magnetizations change from parallel to anti-parallel. As the free F layer reverses, domain walls will move in that layer. If a domain wall moves past a measuring contact, the change in resistance is related to the position of the domain wall and can be used to measure its relative location.

To demonstrate this, a series of 1×10 mm EBSVs were patterned with micron size superconducting top contacts of Nb. The results of transport studies showed that shrinking the area of current flow had no affect on the transport properties of the samples. Then a new series of EBSVs were shaped into long wires with dimensions of order $1 \times 20 \ \mu m$ by electron-beam and photolithography. Micron size top contacts were placed on top of the lithographed features and evidence of domain wall trapping was observed in the MR of the samples.

ACKNOWLEDGEMENTS

I would like to take this space to acknowledge those whose time and effort has contributed significantly to this dissertation.

First, I would like to thank my advisor Prof. William P. Pratt, Jr. The time spent in learning the craft of experiential physics was invaluable. In addition, Prof. Pratt shared the many lessons of being a professional in the world of physics beyond the basics, including producing professional presentations and technical writing.

Second, I would like to acknowledge the help and support of Dr. Reza Loloee, the "Man behind the curtain" within the GMR group. Without the support of Dr. Loloee, much of the research conducted within the GMR group would grind to a halt. His knowledge and assistance to the users of all the critical systems (and sometimes how to deal with life in general) is freely given and always given with smile.

There were a variety of people who were very important to the development of this project. Prof. Anne Reilly and Dr. Juan Caballero were two postdoctoral researchers with whom I worked very closely on the early stages of this project. Secondly I would also like to thank Prof. Norman Birge and Prof. Jack Bass with whom I have had countless discussions about a variety of topics related to this research. Dr. Baokang Bi, manager of the Keck Microfabrication Facility, has provided guidance for many of the fabrication techniques.

Next I would like to thank the remaining members of the "GMR Group" with whom I have worked with during my time at MSU: Khalid Eid, Dr. Jiyeong Gu, Mustafa Al-Haj Darwish, Huseyin Kurt, Antonio Zambano, Dr. Konstantine Nikolaev, Dr. Wanjun Park, and Dr. Maxim Tsoi.

I would also like to thank of those who helped me keep my sanity and provide moments of levity away from work. Fellow Packer supporters Brian Sharpee and Dr. Barton Pritzl have shared many football Sundays in misery and joy. My partners in crime in the physics department, Dr. Charles Moreau, Dr. Peter Peterson, Aaron

Lacluyzé, Dr. Frédéric Pierre, Mike Davis, AJ Rader, Dr. Eric Tryggestad, and Chris Hanley have been indispensable friends. Finally the LAN party crowd has been my source of relief and relaxation for longer than I can remember. Special thanks to Defiant Victim, Mr. Armageddon, Mr. Book, MikeDog, Maxie, Gold, Heywood, 'The Doc,' Slo-Tek, Get-Funk, Digi-Guy, Fry Me2k, Lunchbox, LeFrank, and Happy Fun Ball: the best group of $133t_{-}0n|1||3_{-}vv4n|<3r5$ there is.

Finally I would like to thank my family who have been a source of constant support throughout my education. I would like to especially mention my wife Jennifer and my son Jacob who have been at the center of the maelstrom these last several years. Your patience and support have meant more than words can express.

For my father and mother

It was a dark and stormy night....

Table of Contents

L	IST (OF TABLES	ix
LI	LIST OF FIGURES		
1	Inti	roduction	1
	1.1	Magnetic Domains	3
		1.1.1 Local Energy Contributions	5
		1.1.2 Non-local Magnetic Energy Contributions	5
		1.1.3 Interaction of Energy Contributions	6
		1.1.4 Shape Effects	6
		1.1.5 Domain Walls	8
	1.2	Background of GMR	12
	1.3	CPP Measurements	13
	1.4	Theory of CPP-GMR	16
2	San	aple Fabrication	22
	2.1	Introduction	22
	2.2	Types of Samples	22
		2.2.1 Type-I Samples	24
		2.2.2 Type-II Samples	25
		2.2.3 Type-III samples	26

		2.2.4	Type-IV samples	28
	2.3	Procee	dures	28
		2.3.1	Substrate Cleaning	28
		2.3.2	Sputtering	29
	2.4	Lithog	graphic Procedures	32
		2.4.1	Photolithography	32
		2.4.2	Electron Beam Lithography	34
		2.4.3	Etching	38
		2.4.4	SiO Evaporation	40
	2.5	Measu	rement Equipment	45
		2.5.1	SQUID Based Null Circuit Voltage Measurements	46
		2.5.2	Nanovolt measurements	48
		2.5.3	Area Measurements	49
3	CPI	P-Mul	tilayers with Micron Size Top Contacts	53
			•	
	3.1	Introd	luction	53
	3.2	Initial	Work and Tests	54
		3.2.1	Lithography Test	54
		3.2.2	Current Dependence	56
	3.3	GMR	Transport	59
4	CP	P.Don	nain Wall Tranning	65

LJ	LIST OF REFERENCES		
5	Con	aclusions	81
	4.4	Results	80
	4.3	E-beam Lithography Samples	76
	4.2	Improved Lithography	70
	4.1	Initial Trials	66

List of Tables

2.1	The side dimension of each square listed for the features on the photomask that is shown in figure 2.8. All units are in microns	35
2.2	The side dimension of each square listed for the features on photomask 2 that is shown in figure 2.9. All units are in microns. W40 and W20 refer to the wire geometries of 40 microns length and 20 microns length, respectively, shown in Figure 2.3	35
2.3	Ion milling rates in Å/s for various metals at 10 mA and 20 mA current. For 10 mA, The Ar flow was 3 sccm and for 20 mA, 6 sccm	40

List of Figures

1.1	The basis of this thesis research. A domain wall moves in a ferromagnetic layer (F) that is free to reverse its magnetization (Top F layer). As the wall moves past the top measuring contact the resistance changes in proportion to the location of the wall. The resistance change is from GMR where parallel F-layer magnetizations will give a low resistance and antiparallel magnetizations give a high resistance.	2
1.2	Magnetic hysteresis of a ferromagnet. The rapid changes in magnetization are due to growth of favorably oriented domains by domain wall propagation. The slower changes near saturation are due to coherent magnetization rotation of domains.	4
1.3	Domain formation in a single crystal. (a) A single crystal that is uniformly magnetized. (b) Dividing the crystal into two magnetic domains reduces the stray field energy. (c) Further division into domains will reduce the stray field energy until the energy to create a new domain is greater than the reduction to the stray field. (d) Closure domains can reduce the stray field energy to zero, but can contribute to the anisotropy energy	7
1.4	Shape anisotropy is used to trap a domain wall in patterned wires. In (a) through (c) a domain wall starts in the wider portion of the wall. (a) As an applied magnetic field is increased in the up direction the wall will move towards the narrow portion of the wire. (b) The applied magnetic field does not give a large enough Zeeman energy contribution to allow the wall to enter the narrow portion of the wire. The narrow portion of the wire has much larger stray field energy due to surface and edge effects. (c) The magnetic field is increased enough for the wall to enter the narrow portion of the wire. (d) through (f) repeat this sequence with a narrow neck or notch region. The effect is the same, except once the wall gains enough energy to leave the initial constriction, it most likely has enough energy to move entirely to the end of the wire.	ç
1.5	The two most common types of domain walls. The Nèel wall has the magnetization rotating in x-z plane. The Bloch wall has the magnetization rotate vertically in the z-y plane	11

1.6	An explanation of the basic GMR effect. On the left, when the magnetizations (white arrows) of the magnetic layers, F, are antiparallel, both the spin up and spin down electrons have equal resistance paths. When the magnetizations are parallel, the spin up electrons (in this case) have a lower resistance path compared with spin down electrons. This leads to a much lower overall resistance	13
1.7	A diagram of the CIP geometry vs. the CPP geometry. In the CIP geometry the current (black arrow) flows parallel to the multilayer interfaces. In the CPP geometry the current flows perpendicular the layer interfaces (The diagram dimensions are not to scale, typical layer thickness (vertical dimension here) is 1 - 10 nm, while the width and depth of the samples (horizontal and perpendicular out of plane dimensions) are 0.1 to 10 mm).	14
1.8	A simplified diagram of the 4s and 3d energy bands for Co. The up and down arrows represent the bands for the up and down electrons, respectively. Since the 3d\u03a4 band fills with up electrons first, at the fermi level, the density of states for down electrons is much larger giving a higher resistivity.	17
1.9	A diagram of the two current series resistor model for the AP state. The current is divided into two channels: spin up channel (top) and spin down channel (bottom). One adds the series resistances for each channel and then combines the series resistances as two resistances in parallel to produce the overall resistance for both the AP states	19
2.1	An overview of the fabrication process. A side profile is provided on the left (only half of the lithographic features are shown to conserve space), and a complete top view is provided on the right. The dimensions of the system are not to scale. A multilayer is sputtered onto a cleaned substrate (A). A lithographic pattern/mask is placed onto the multilayer (B). A portion of the multilayer is etched away, an insulting layer deposited and the lithographic pattern removed (C). The top contacts are sputtered onto the sample (D)	23
2.2	An overview of the different types of samples. Type-I has contact made to a Au capping layer. Type-II has a partially etched Au/Nb/Au cap. Type-III has the entire multilayer etched. Type-IV has a separate contact geometry on top of a patterned multilayer	25

2.3	A diagram of the mask for fabricated wires with a neck. There were two sizes of wire designed. Mask b is exactly a factor of two smaller than a. Each is symmetric about the notch region	27
2.4	The difference between a via and a proud column. A via is a trench or window in the insulating layer through which contact with the top superconductor (dashed line) is made. A proud column sticks above the insulating layer. Proud columns become necessary when the feature size is below $2 \mu m$	27
2.5	The layout of the mask system. The rotating mask (inner circle) is rotated to expose a sample to the sputtering plasma. A shadow mask (not shown) over the substrate defines the actual pattern. The 12 o clock and 6 o clock positions correspond to a closed position while the 3 o clock and 9 o clock position will expose the sample. The rotating mask is aligned by lining up the pins of the rotating mask to be in line with the bridges holding down the samples. The mask here is shown in the 9 o clock position while the others are represented with dashed lines	30
2.6	A exploded view of the sample holder. The bridge clamps the heat sink/substrate/shadow mask together. The assembly is attached with screws to the sample holder through the bridge. Each sample holder is designed to hold two assemblies.	30
2.7	A layout of the mask system to deposit top Nb leads. (A) The multi-layer with patterned mask features (exaggerated size, in black). Each feature is spaced so that when the far right opening in the shadow mask (B) is lined up with the protrusion in the multilayer (A), the individual exposed contact areas will each fall within a single Nb contact (C) .	32
2.8	A diagram of the layout and dimensions of the first photomask. A single array of features was arranged as shown. The dimensions of the features are listed in Table 2.1	35
2.9	A diagram of the layout and dimensions of the second photomask. On this mask, the array was repeated multiple times on the mask. The dimensions of the features are listed in Table 2.2	36

2.10	The bilayer of PMMA and Copolymer after evaporation. The development removes the copolymer more than the PMMA causing the undercut. The difference in removal is due the copolymer's stronger sensitivity to the backscattered electrons from the substrate. This allows the deposited Al feature, patterned from the PMMA, to be isolated from the rest of the evaporated material. The bilayer will be removed in the next step by Acetone, and only the Al on the sample will remain.	38
2.11	The setup of the small chamber. The samples can be rotated to the desired position on the sample plate. A shutter, independent of the sample plate, can also be rotated to an open or closed position depending on source to be run. The magnetic arm for loading samples through a load lock is in the upper right	41
2.12	The tantalum boat for SiO evaporation. The SiO is placed in the loading area. The entire boat is heated using a current source. When the SiO begins to evaporate it must flow through a series of baffles that prevent spitting. The evaporated SiO then escapes vertically (side view) toward the sample	43
2.13	SiO_x deposition. The insulator is evaporated at a 15 degree angle with respect to the sample-surface normal. This and the rotation help to eliminate pinholes	44
2.14	Measurement setup and geometry of the sample. Input current and voltage leads are attached to the contact to be measured (#1). Output-current and second-voltage leads are attached to #2 and #3 contacts, respectively. Current flows between contacts #1 and #2 (via solid arrows), and the voltage contact at #3 measures the potential of the bottom superconductor	46
2.15	The SQUID null feedback circuit. An RF SQUID system (SQUID, inductor, RF LC circuit, and semiconductor electronics) balances the circuit so no current flows from point A to point B. The voltage drop across both resistors is equal in this balanced state. From Ohm's law, one can then solve for R_x and in terms of I_A , I_{FB} and R_{Ref} . I_A is applied to the system and is known. This applied current causes the SQUID system to go out of balance. The feedback current from the SQUID system, I_{FB} , is measured by a resistor in series with the reference	
	resistor, R_{Ref} . R_{Ref} is a precision resistor with a known resistance.	47

2.16	The circuit layout of the nanovolt probe. A Keithly 2400 current source (1) is connected to a Keithly 7011 multiplexer card (2) with two electronically isolated banks of connections that allow each wire coming from the probe to be selected as either high or low in combination with any other wire. A Keithly 2182 nanovoltmeter (3) is connected to the voltage leads. However, the Keithly 7168 multiplexer card can only support one voltage connection per voltage lead. Thus half the voltage leads are hardwired as V+ and the others are V- (4a,4b) The wires are then connected to the probe (5,6; see Figure 2.18). Finally the leads are taken to the low temperature portion of the measurement in the measuring probe and connected to the sample	50
2.17	The modular measuring probe used for nanovolt measurements. The magnet, magnet leads, and persistent switch connections are self-contained in a sheath that connects to the I-V portion of the probe via a quick connect. This sheath surrounds the probe and the connection is placed at a pre-determined location to put the sample in the middle of the magnet. The measurement portion of the probe can be used with or without the magnet portion.	51
2.18	A layout of the external connections to the measuring probe (one side only, see items 5 & 6 in Figure 2.16). For both the current and voltage leads, each wire is connected to a grounding system individually. The grounding system is also wired to a switch which chooses between a direct ground or grounding through a 1 $M\Omega$ resistor to minimize currents induced by static charges. The shield for each cable is directly connected to ground. Outside the probe, all current leads are inside a single shielded cable and each pair of voltage leads has its own shielded cable	52
3.1	A plot of the specific resistance for single layer $Co_{91}Fe_9$ samples versus the $Co_{91}Fe_9$ layer thickness. The circles represent samples with a C_I cap that underwent a cleaning procedure without ultrasonic agitation. The triangles represent samples that did have ultrasonic agitation (C_I cap). The squares represent a C_{II} cap with the original (non-ultrasonic) cleaning	55
3.2	An explanation of vias (black areas with white arrows). The portion of the Nb (white, black for vias) where the current (block arrows) flows from the Nb that lies on the SiO (grey) to the portion of Nb in contact with the multilayer. The current only flows along the edges because the penetration depth of the superconducting Nb is ~ 100 nm	57

3.3	The current dependence of several of the smallest contact areas for $\text{Co}_{91}\text{Fe}_{9}$ samples. The right hand vertical line represents the expected Nb limit of 5×10^6 A/cm ² [39]. As the lithography improved over time so did the amount of current that the superconducting contact could support. The sample with $28 \ \mu\text{m}^2$ was one of the earliest samples while the $4.5 \ \mu\text{m}^2$ was one of the last fabricated samples. Also note the high contact resistance of the $9.5 \ \mu\text{m}^2$ sample and how it will not support a high current density	58
3.4	$A\Delta R$ vs Area for several thickness of $Co_{91}Fe_{9}$. The variations in $A\Delta R$ are similar to those seen in previously published data for samples with areas of current flow of 1 mm ² (far right). Note that while the 30 nm data has large variations, individual substrates showed more consistent data, except for substrate 1 which had a poorly defined contact area for one of the contacts (poor-lift-off)	60
3.5	$A\Delta R$ vs Area for several thickness of Py. The variations in $A\Delta R$ are similar to those seen in previously published data for samples with areas of current flow of 1 mm ² (far right hand side)	60
3.6	Minor hysteresis loops of CPP resistance versus magnetic field for one of the smallest contact-area Py samples compared with a 1×1 mm sample ($t_{Py} = 6$ nm for both samples). The saturation and coercive fields have been affected by processing	61
3.7	Minor hysteresis loops of CPP resistance versus field for (a) $t_{Py}=15$ nm and (b) $t_{CoFe}=18$ nm samples. Here the magnetic properties are very similar to those at 1 mm ² samples	62
3.8	The effect of the spin diffusion length l_{sf} on $A\Delta R$. The experimental results show that l_{sf} is indeed finite	63
3.9	$A\Delta R$ versus t_{CoFe} for 1×1 mm (solid squares) and micron-size (open circles) CoFe EBSVs	64
3.10	$A\Delta R$ versus t_{Py} for Py EBSVs with 1×1 mm (solid triangles) and micron-size (open circles) areas	64

4.1	The layout of different wires used for domain wall trapping. (a) A poor candidate for domain wall trapping as the ends will not easily produce domain wall nucleation. Many of the initial 2- μ m-wide samples were shaped like this due to poor contact in the mask aligner. (b) The flat ends will be better for domain wall nucleation. This was the goal of the photolithography trials. (c) The best option is to provide a source of domain walls. The diamond on the end will be multidomain and nearly always inject a domain wall into the sample. This configuration was used for e-beam samples	67
4.2	A Ni ₈₄ Fe ₁₆ EBSV ($t_{Py}=60$ nm) in the large photolithography geometry. There is poor evidence of domain wall trapping	68
4.3	A $Co_{91}Fe_9$ EBSV ($t_{CoFe}=30$ nm) from earlier transport studies (Chapter 3) that gives indications of domain wall trapping behavior. Note the plateau (in the transitions) between the P and AP states	69
4.4	The best domain wall trapping sample with the initial lithography. Although decent results were obtained, they were not reproducible, as evidenced by these two runs on the same structure. This is a $Co_{91}Fe_9$ EBSV with $t_{CoFe} = 18$ nm	71
4.5	Removing the buildup of photoresist with acetone and a q-tip greatly increased the resolution of the photolithography. Before this improvement, the photoresist along the edges was much thicker and hindered good contact with the mask	72
4.6	A domain wall trapping sample with the smaller of the 2 wire geometries. Although decent results were measured they were not reproducible, as evidenced by these two runs on the same structure. This data is from a $Co_{91}Fe_9$ EBSV with $t_{CoFe}=6$ nm	73
4.7	A 5 μ m contact on the small wire configuration for a Co ₉₁ Fe ₉ EBSV (t _{CoFe} = 12 nm). The large plateaus in between the P and AP states are likely the domain wall trapping. ΔR_{Notch} is roughly the same for both intermediate states. Based on the total ΔR and the resistance noise, one can locate the domain wall in this sample to about 10 nm.	74
4.8	An SEM picture of a Type-IV sample. Notice that the top contact (square) is off center. The location of the notch in top contact region determines where the intermediate state will occur in the MR transition.	75

4.9	The pattern for e-beam lithographed samples. A diamond at the end of each wire is patterned to provide a source of domain wall injection. The aspect ratio of each wire has also been increased to facilitate single domain wires. Ideally the wide wire would have 40 μ m segments, but the pattern would exceed the range of the writing microscope	77
4.10	A single MR curve for a $Ni_{84}Fe_{16}EBSV$ ($t_{Py}=12$ nm). Notice the intermediate state located nearly at the half way point	78
4.11	Repeated MR curves for a single sample 1 μ m wide (Py EBSV with $t_{Py}=12$ nm). The trapping appears reproducible. Complete curves were not obtained in some cases due to problems with the electronics .	79
4.12	The motion of a domain wall (grey) after it becomes pinned by defect or geometry (black circles). The ends of the wall tend to stay fixed while the center will bow out.	80
5.1	A proposed top view of the new fabrication to put Nb only in certain areas of the sample. (a) Photolithography patterned leads are made by sputtering an entire EBSV onto a substrate photoresist mask. The mask allows features down to several μ m to be patterned. Note: extensions of these patterned leads to mm size contact pads are not shown here. (b) Using the unattached leads as rough alignment marks, a wire mask feature is patterned on the center lead by e-beam lithography. The sample is then ion milled to the bottom Nb (Au coated) leaving the EBSV structure only underneath the mask (including alignment marks). (c) The sample is planarized. (d) The alignment marks are used to align a pattern (photo- or e-beam lithography) that will expose the notch region and a connection to the remaining leads. Sputtering Nb into the exposed region completes the sample	83

Chapter 1: Introduction

One of the most important areas of magnetic technology today is the study of small features where the size of the ferromagnetic (F) elements used in a device is comparable to the domain size. As those elements shrink those sizes, the mechanism of domain switching and domain wall motion are strongly affected, and the physics of such mechanisms is of great interest.

The goal of this research is to make high resolution studies of domain wall motion. As the direction of magnetization switches in a magnetic element in the presence of a changing magnetic field, a domain wall, representing the boundary between favorably oriented magnetic moments and non-favorable magnetic moments, will move through the sample. By using a giant (G) magnetoresistance (MR) multilayer with the current perpendicular to the plane (CPP), it is possible to study the motion of the wall on a scale of a few nm (Figure 1.1).

The GMR effect is a large change in resistance for a multilayer that depends on the relative orientation of the magnetizations of the F layers within the multilayer. Although the details are provided later, the basic effect is that when the magnetizations of the F layers are aligned parallel (P), the resistance is low; when the magnetizations are aligned anti-parallel (AP), the resistance is high. In these studies the magnetization of one layer is fixed, while the other is free to respond to an applied field. When the switching of the free layer takes place, it typically occurs by the propagation of a domain wall. As that domain wall moves past the measuring contact, the movement of the wall will be sensed as a resistance change since the regions of P and AP magnetization are changing.

In order to provide a background for what this research encompasses, a brief introduction to the subject of magnetic domains and the basic physics of GMR will be given.

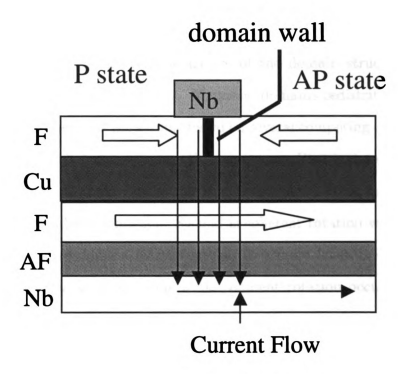


Figure 1.1: The basis of this thesis research. A domain wall moves in a ferromagnetic layer (F) that is free to reverse its magnetization (Top F layer). As the wall moves past the top measuring contact the resistance changes in proportion to the location of the wall. The resistance change is from GMR where parallel F-layer magnetizations will give a low resistance and antiparallel magnetizations give a high resistance.

1.1 Magnetic Domains

When placed in a sufficiently strong magnetic field, ferromagnets show a very large magnetization. In addition, they can remain magnetized even when the applied field is returned to zero. However, an ordinary piece of ferromagnetic material can at first be demagnitized. Such a demagnetized initial state is due to the presence of magnetic domains with randomly oriented magnetizations. When exposed to a slowly varying magnetic field, the domain structure will change so that the sample becomes magnetized. Due to the irreversible nature of the domain structure changes, the magnetization will exhibit hysteresis. Magnetic domains redistribute themselves to reduce the overall energy of the sample based on several competing energies. There are two methods by which domains change their structure. First is the growth of favorably oriented domains. Domain 'walls' move to incorporate more moments that have switched to a favorable orientation. Second is coherent rotation where the magnetic moments of an entire domain rotate together to a more favorable orientation. Wall propagation happens at lower fields while coherent rotation occurs at higher fields (Figure 1.2).

Domains form in ferromagnets due to competing energies. These energies can be divided into local and non-local contributions. Local terms are derived from energy densities which depend on the local value of the magnetization. The energy associated with each can be calculated by a single integral of the form $\int f(\mathbf{m})dV$ where $f(\mathbf{m})$ is a function of the magnetization direction $\mathbf{m}(\mathbf{r}) = \mathbf{J}(\mathbf{r})/J_S$, where $\mathbf{J}(\mathbf{r})$ is the magnetization [1].

Non-local energies are torques on the magnetization vector at each point that depend on the magnetization vector at every other point. Generally, these energies cannot be calculated with a single integral [1].

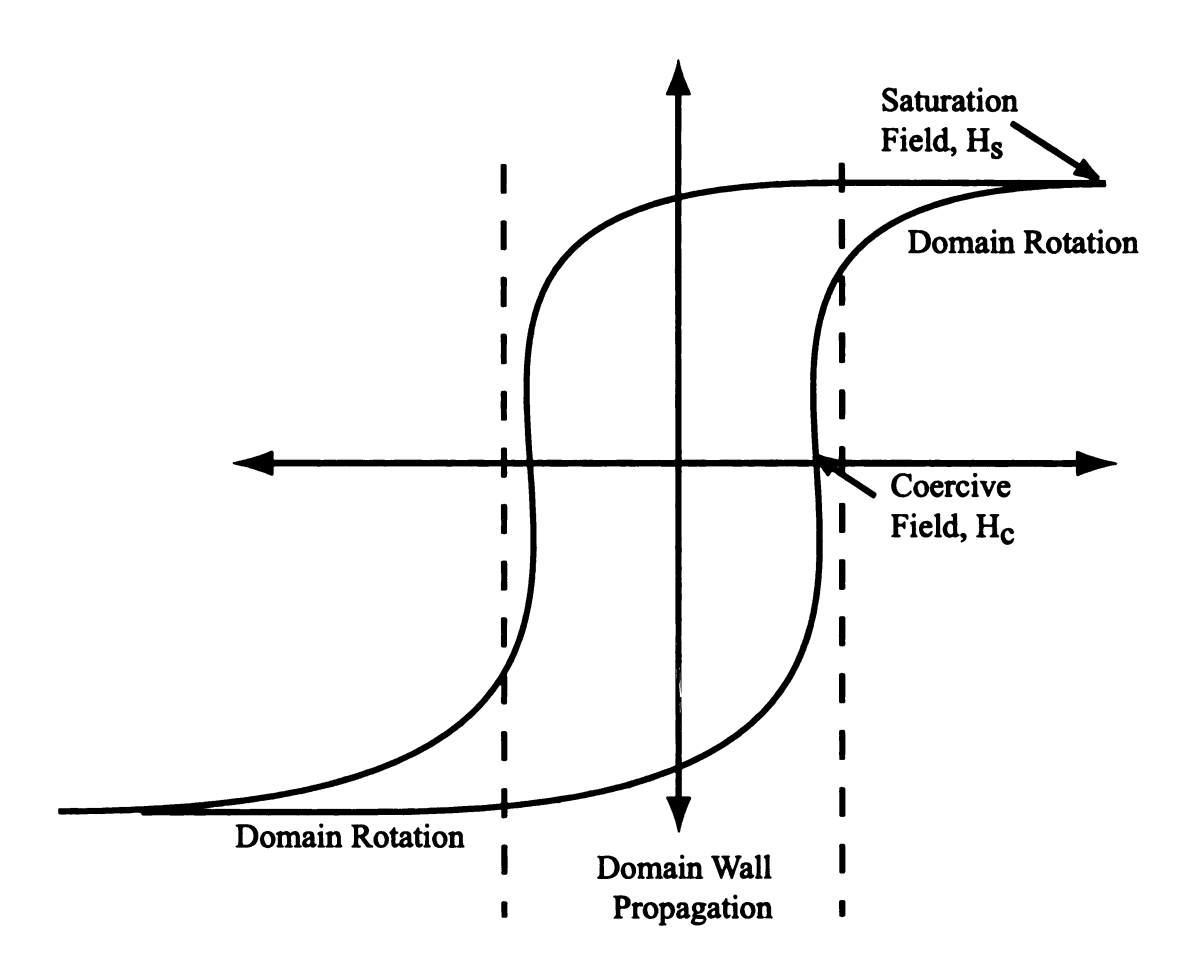


Figure 1.2: Magnetic hysteresis of a ferromagnet. The rapid changes in magnetization are due to growth of favorably oriented domains by domain wall propagation. The slower changes near saturation are due to coherent magnetization rotation of domains.

1.1.1 Local Energy Contributions

The first local energy contribution is the exchange energy. The exchange energy causes a preference for a constant direction of magnetization. Changes from this equilibrium produce an energy of the form:

$$E_{Ex} = A \int (\nabla \mathbf{m})^2 \ dV \tag{1.1}$$

where A is a constant that depends upon the material. A is referred to as an exchange stiffness constant and gives a measure of the strength of the coupling between the spins in the material [1].

The second local energy contribution is the anisotropy energy E_a . A ferromagnetic crystal will have preferred axes of magnetization. These preferred directions arise from the band structure of the material and the spin-orbit interaction [1,2]. The form of the anisotropy energy is highly dependent on the crystal symmetry and is discussed in detail elsewhere [3,4].

The third local energy contribution is the external field or Zeeman energy. This is the contribution from the interaction of the external applied field $\mathbf{H_{ap}}$ and the magnetization [1]:

$$E_Z = -J_s \int \mathbf{H_{ap}} \cdot \mathbf{m} \ dV \qquad . \tag{1.2}$$

1.1.2 Non-local Magnetic Energy Contributions

There is one large and one small non-local energy contribution. The large contribution is the stray field energy or the energy of the magnetic field $\mathbf{H_m}$ created by the magnetization. This usually takes the form [1]:

$$E_{St} = \frac{1}{2}\mu_0 \int \mathbf{H_m}^2 dV = -\frac{1}{2} \int \mathbf{H_m} \cdot \mathbf{J} dV \qquad (1.3)$$

The other is magnetostriction, which is the energy associated with the elastic motion due to magnetic fields. This latter energy will not be an important contribution in this research.

1.1.3 Interaction of Energy Contributions

All of the above energy components combine to give a domain structure. The best way to explain this is with an example. Consider a square crystal magnetized entirely in a single direction (Figure 1.3a). By dividing the configuration into two separate oppositely magnetized domains, the stray field energy of the example has roughly been reduced by a factor of two (Figure 1.3b). The addition of more oppositely magnetized domains will continue to reduce the stray field energy until the energy to produce a new boundary (both the exchange and anisotropy energies) between domains is greater than the stray field energy reduction in the field (Figure 1.3c).

It is possible to form domain arrangements where the magnetic field is zero and thus the stray field energy is zero outside the sample. By forming triangular domains at the ends of the example with magnetization at 90° to the original domains, there will be no surface poles of magnetization and the stray field energy will then be zero (Figure 1.3d) externally. These types of domains are known as domains of closure. The anisotropic energy may hinder the formation of the closure domains, since the magnetization may fall along a hard axis of magnetization.

1.1.4 Shape Effects

Altering the external shape of a sample can also affect the domain structure of a sample. In Figure 1.3 the example was a rectangle. It is well known the external shape can significantly affect the preferred axis of magnetization, and it is also possible to trap a domain wall using shape effects. For long narrow wires it is well known that the magnetization prefers to align only along the long axis of the wire. This is so-called

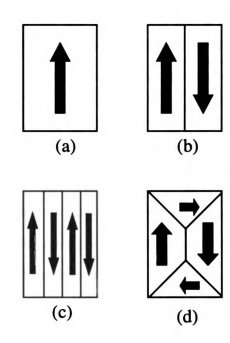


Figure 1.3: Domain formation in a single crystal. (a) A single crystal that is uniformly magnetized. (b) Dividing the crystal into two magnetic domains reduces the stray field energy. (c) Further division into domains will reduce the stray field energy until the energy to create a new domain is greater than the reduction to the stray field. (d) Closure domains can reduce the stray field energy to zero, but can contribute to the anisotropy energy.

shape anisotropy and is a consequence of the stray field energy [1].

Consider a long narrow wire with a domain wall located in the lower half (Figure 1.4). As an applied field is reversed, the domain wall will move along the wire to accommodate the growth of the favorably oriented domain. If a narrow region is placed along the wire, the wall will enter that region and if the field is being increased slowly, the wall will remain in the notch area since the wall energy itself is reduced, and the energy to facilitate domain growth in the narrow region is greater than the wide region. Extra energy is needed to overcome this barrier. The wall will then stay in the neck (trapped) until the applied field contributes enough stray field energy to drive the wall out of the notch.

1.1.5 Domain Walls

The boundaries between domains are known as domain walls. These are regions where the magnetic moment changes from one orientation to another. There are several types of walls that form based on the previously mentioned competing energies. Before the different types of walls are described, it is important to see why the competing energies lead to the formation of walls.

As mentioned before, it is energetically favorable to have domains. However, the exchange interaction energy makes it more favorable for the transitions between the differently oriented domains to be gradual rather than abrupt transitions. As shown in standard physics texts [5,6], a gradual transition from one orientation to another will reduce the overall energy of the system.

Starting with the Heisenberg model for the exchange energy E_{Ex} , we have

$$E_{Ex} = -2J\mathbf{S_i} \cdot \mathbf{S_j} \quad , \tag{1.4}$$

where J is the exchange integral. Replacing $\cos \theta$ with the small angle approximation

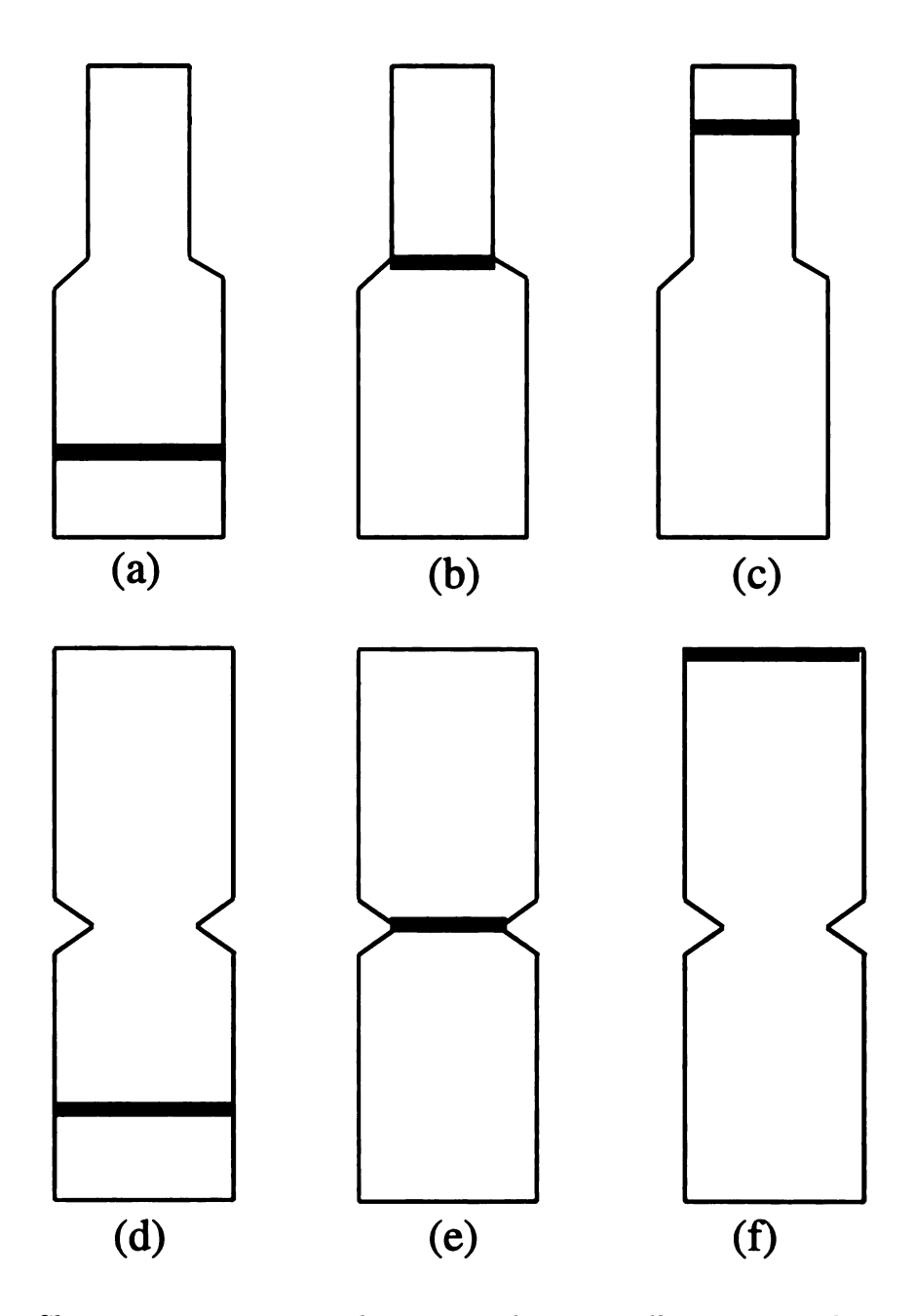


Figure 1.4: Shape anisotropy is used to trap a domain wall in patterned wires. In (a) through (c) a domain wall starts in the wider portion of the wall. (a) As an applied magnetic field is increased in the up direction the wall will move towards the narrow portion of the wire. (b) The applied magnetic field does not give a large enough Zeeman energy contribution to allow the wall to enter the narrow portion of the wire. The narrow portion of the wire has much larger stray field energy due to surface and edge effects. (c) The magnetic field is increased enough for the wall to enter the narrow portion of the wire. (d) through (f) repeat this sequence with a narrow neck or notch region. The effect is the same, except once the wall gains enough energy to leave the initial constriction, it most likely has enough energy to move entirely to the end of the wire.

gives an exchange energy between two spins of $JS^2\theta^2$. Using π/N as the angle between nearest neighbors of a wall N atoms thick, one obtains that each neighboring pair contributes $JS^2(\pi/N)^2$. The total energy of N+1 atoms would then be $JS^2(\pi^2/N)$ for large N. If there were no anisotropy energy, the wall would thicken to infinity, but generally the spins are directed away from the easy axis of magnetization and thus contribute an addition anisotropy energy [2, 5].

Two of the most common walls in thin films are the Bloch and Neèl walls (Figure 1.5). Although Bloch walls are energetically favorable in thicker materials, Nèel walls become preferred as the layer thickness decreases, since the Bloch wall will produce poles at the surface, creating a stray field energy (at the surface) which increases with decreasing layer thickness. The Neel wall avoids this problem at the cost of a large stray field energy inside the magnetic region (which makes the Nèel wall unfavorable in bulk materials). For the samples studied in this research, the Nèel wall is energetically more favorable [7].

The width of the wall depends on both the exchange and anisotropy energies. There is no widespread agreement on what defines the wall "width." However, for the current studies a precise definition of the width is not necessary. It has also been proposed that a geometrically constrained wall in thin films may be a new type of wall that has Néel tails extending several nm [8]. It is the domain wall propagation or movement that is of interest to this study. One et al. showed by using a current-in-plane GMR that observing domain wall trapping was possible [9,10]. CPP-GMR can also be used to study the domain wall propagation down a long narrow ($\sim 1\mu$ m wide) wire. By using external shape to create pinning sites (Figure 1.4), a domain wall can be trapped in a narrow neck placed in the above-mentioned wire. For a GMR sandwich with two F layers and well defined P and AP states, the trapping of a domain wall in one of the layers will create an intermediate state where the resistance is between the P and AP resistances. A further advantage of CPP-GMR is that the

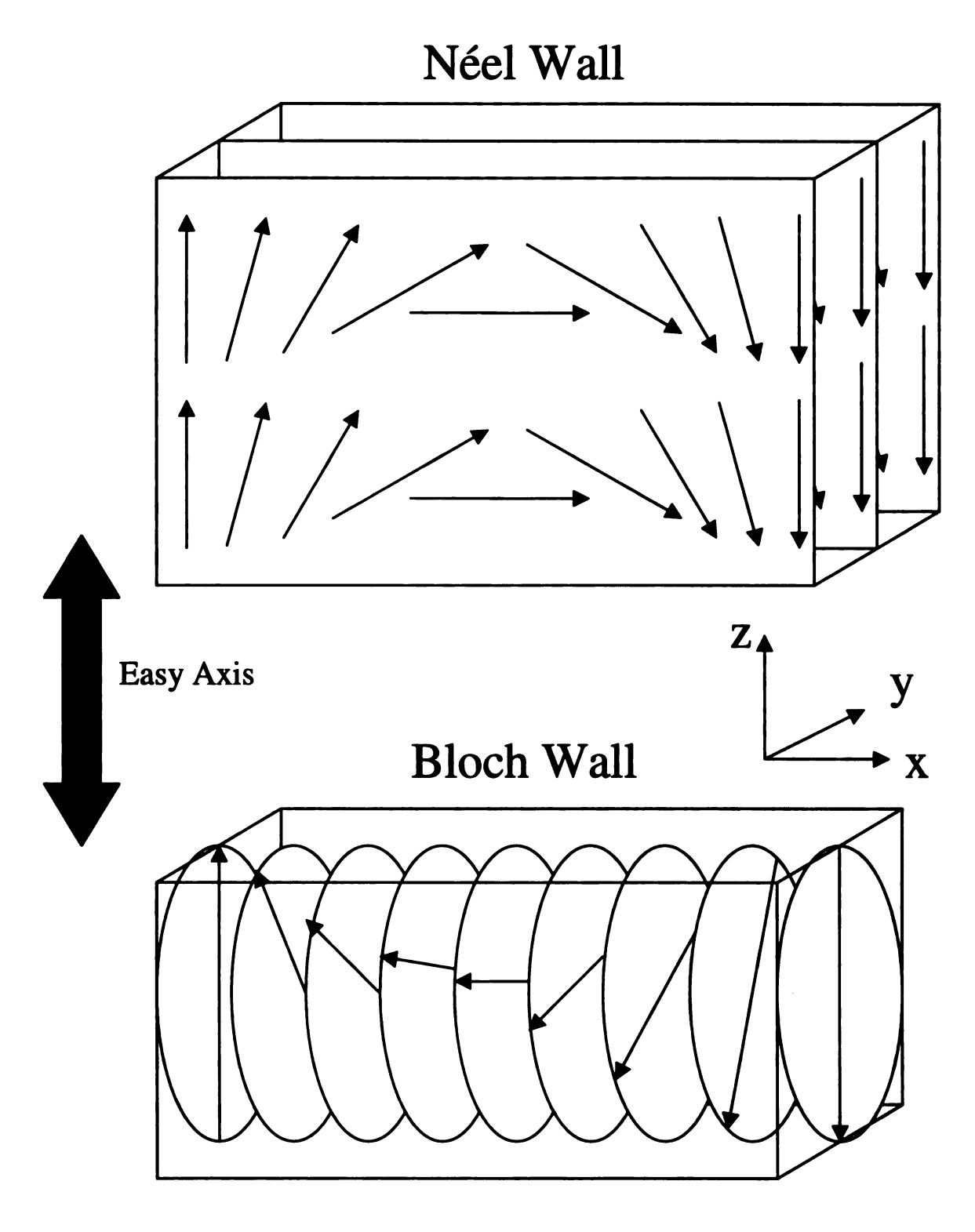


Figure 1.5: The two most common types of domain walls. The Nèel wall has the magnetization rotating in x-z plane. The Bloch wall has the magnetization rotate vertically in the z-y plane.

current may be confined to the trapping region instead of flowing through the entire sample, as occurred for the Ono samples.

1.2 Background of GMR

Magnetoresistance (MR) is the change in resistance in a conductor due to an applied external magnetic field. Giant magnetoresistance (GMR) is a specific MR effect in multilayers due to spin dependent scattering. Current in a ferromagnetic / non-magnetic (F/N) multilayer can be thought as having two current components: one current composed of up electrons (with spin parallel to the magnetization) and one composed of spin down electrons (with spin anti-parallel to the magnetization). Due to spin dependent scattering, the resistivity of one channel of electrons is less than the resistivity of the other spin channel in the F layers (normally spin up has a much less resistivity than spin down, but this is not always the case). When the magnetizations of all F layers in the multilayer are parallel (P), the up electrons have a much lower total resistance path than the down electrons. The total resistance is 'shorted,' similar to two resistances in parallel, the total circuit resistance will be approximately the lesser of the two resistances if one resistance is much smaller than the other. If the F layers have an anti-parallel configuration (AP), both current paths have identical resistances and the overall resistance is higher. A simple explanation of GMR is shown in Figure 1.6. This effect can lead to resistance drops by a factor of two or more in some layer configurations. This large change in resistance has many practical applications such as magnetic read heads for hard drive storage, magnetic sensors, and magnetic random access memories.

GMR was discovered in 1988 in a superlattice multilayer with alternating Fe and Cr layers [11, 12]. This discovery has opened a new field of research in the area of multilayer structures, which is now known as spin electronics or spintronics. These

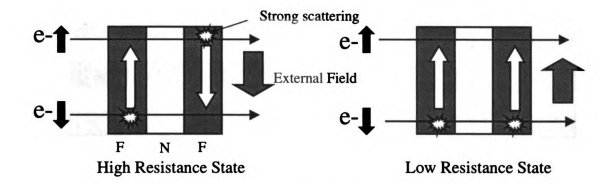


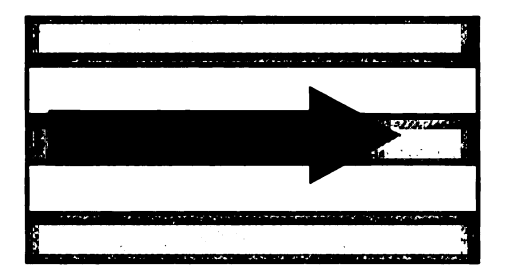
Figure 1.6: An explanation of the basic GMR effect. On the left, when the magnetizations (white arrows) of the magnetic layers, F, are antiparallel, both the spin up and spin down electrons have equal resistance paths. When the magnetizations are parallel, the spin up electrons (in this case) have a lower resistance path compared with spin down electrons. This leads to a much lower overall resistance.

first experiments were done on single crystal samples grown with molecular beam epitaxy. Later investigations reproduced the results of the Fe/Cr multilayer as well as Co/Ru and Co/Cu multilayers using polycrystalline samples deposited by sputtering [13]. In addition, the first experiments were done in a geometry where the current flows parallel to the planes of the multilayer (Figure 1.7).

The geometry where the current flows in the plane (CIP) of the multilayer is difficult to model experimentally. In order for an electron to show the GMR effect it must sample several different magnetic layers. Since the current is travelling along the multilayer, scattering must be responsible to get the electron to move across interfaces and into several different layers. The mean free path is thus a very important parameter with CIP geometry experiments.

1.3 CPP Measurements

An alternative geometry has been developed [14–22]. By passing the current perpendicular to the planes (CPP), the electron current must now travel through every layer. Since scattering is no longer required to move electrons across interfaces,



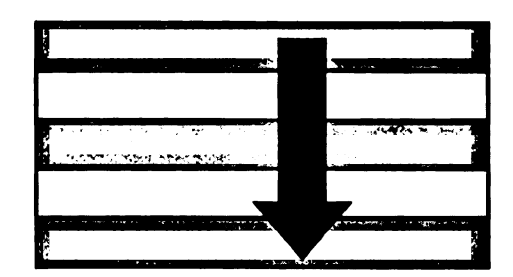


Figure 1.7: A diagram of the CIP geometry vs. the CPP geometry. In the CIP geometry the current (black arrow) flows parallel to the multilayer interfaces. In the CPP geometry the current flows perpendicular the layer interfaces (The diagram dimensions are not to scale, typical layer thickness (vertical dimension here) is 1 - 10 nm, while the width and depth of the samples (horizontal and perpendicular out of plane dimensions) are 0.1 to 10 mm).

the mean free path is no longer an important parameter. Instead, the spin diffusion length, l_{sf} , becomes the dominating length scale. l_{sf} is the distance an electron will hold its spin direction while it is diffusing in a given material. Once electrons start to spin flip scatter, the GMR effect is reduced.

CPP-GMR presents several advantageous over CIP-GMR. First, the GMR effect is larger in the CPP geometry. Second, the CPP geometry allows easier access to the fundamental parameters of GMR. The disadvantage of CPP-GMR is the very low resistance of the samples. For example, a typical 100-nm-thick single layer of Co₉₁Fe₉, 1 mm wide and 1 cm long in the CIP geometry will have a resistance of

$$R = \frac{\rho l}{A} = \frac{7\mu\Omega cm \times 1cm}{.1cm \times (100 \times 10^{-7}cm)} = 7\Omega \qquad ; \tag{1.5}$$

for the CPP configuration a typical geometry is 1 mm \times 1 mm for a 100 nm thick $\text{Co}_{91}\text{Fe}_{9}$ sample, which gives a resistance of

$$R = \frac{\rho l}{A} = \frac{70\mu\Omega cm \times 100nm}{.1cm \times .1cm} = 7n\Omega \tag{1.6}$$

well outside the range of traditional resistance measurements.

There are several methods used to experimentally measure CPP-GMR. Because of the very small layer thickness, these fall into two major categories: (1) very sensitive measurement techniques can be used; or (2) the area of current flow can be reduced to produce resistances measurable by more traditional means.

The first measurements of CPP-GMR were done at Michigan State University [14] by sandwiching a multilayer between two 1-mm-wide crossed superconducting strips composed of Nb. This geometry provides a uniform current flow through the multilayer, and a SQUID based self-balancing potentiometer circuit is used to detect the $n\Omega$ resistance. Because of the use of superconductors, measurements are generally done at liquid helium temperatures.

Additional techniques [16–18,22] have been developed which rely on lithographically microfabricated samples to eliminate the need for superconducting contacts. This type of sample is several μ m in diameter and $\leq 1~\mu$ m thick. This type of measurement is not straightforward since there are significant and not well defined contributions from the contact resistance and additional resistance from the leads. Also, the current flow is complex and not necessarily perpendicular to the planes of the multilayer. Despite these drawbacks the first temperature dependent CPP-GMR measurements were performed with this method. Later efforts [22] including superconducting contacts to improve current flow, but this method used many (100) contacts in series, providing an additional constraint of high yield lithography, since a single poor contact in the series chain can ruin the measurement.

Another microfabrication method to produce small size samples is to use electrode-posited nanowires formed in nuclear-track-etched polycarbonate membranes [19–21]. The very high aspect ratio, with a length of $\sim 10~\mu m$ and diameter of 20-100 nm, provides a more perpendicular current flow than the previous microfabricated samples. It is difficult, however, to determine the number of nanowires being measured in

parallel [23]. This makes it difficult to determine the absolute value of the resistance of an individual wire.

This thesis proposes a new type of CPP-sample measurement. By employing microfabricated superconducting contacts, micron size areas of current flow can be used to study initially otherwise macroscopic (1 × 10 mm) samples. This method can additionally be used to study multiple areas of the same sample. These microfabricated contacts will provide uniform current flow through a small cross sectional area, combining many advantages of superconducting leads and small areas of current flow, while avoiding complex lithography. A secondary goal of this research is to produce samples whose resistance is large enough to measure with a nanovolt system. Finally, as the sample size is reduced, it will be possible to do high-resolution 'imaging' of domain wall trapping.

1.4 Theory of CPP-GMR

The present theory of CPP-GMR has two forms based on the relative size of l_{sf} and the layer thickness, t. The first form describes [24] why the two current series resistor (2CSR) model holds when $l_{sf}\gg$ t. The second form was developed [24, 25] for $l_{sf}\simeq$ t and includes an extension of the 2CSR model for short l_{sf} .

Before going into the details of CPP-GMR, it is useful to provide a simple picture of the physics occurring in the multilayer. For example, in this simple picture, Co can be thought of in terms of 4s and 3d parabolic electron bands [24, 26, 27]. It is the 4s band that will be the primary conduction carrier, since the band has a very low effective mass. The 3d electron bands can be split into spin up and spin down bands. Because of the exclusion principle, electrons with spin up will begin filling the 3d-bands of the metals. Once all the spin up states are occupied the spin down states will become partially occupied. From Fermi's golden rule, the rate of scattering of the

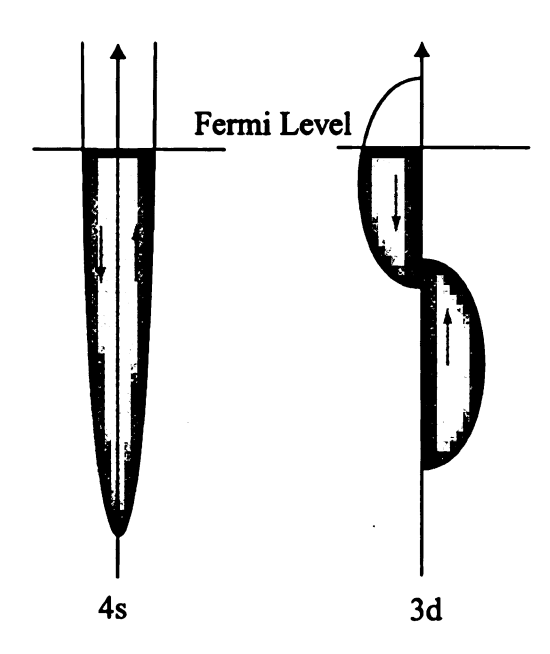


Figure 1.8: A simplified diagram of the 4s and 3d energy bands for Co. The up and down arrows represent the bands for the up and down electrons, respectively. Since the 3d[†] band fills with up electrons first, at the fermi level, the density of states for down electrons is much larger giving a higher resistivity.

4s electrons (and thus resistivity) will be proportional to the density of states of the 3d electrons, so spin down electrons, having a higher density of states at the Fermi level, will have a higher resistivity (Figure 1.8).

In the 2CSR model, the resistance of a multilayer is obtained by dividing the current into independent spin up and spin down contributions and calculating the resistance each current encounters in both the parallel (P) and anti-parallel (AP) states. Each bulk and interface resistance can be thought of as a separate resistor. To calculate the GMR one adds up the resistance contributions in series for each current channel and combines them as two overall resistors in parallel. When the resistances from both the P and AP magnetic states are known a simple calculation of the specific resistance $A\Delta R = Area \times (R_{AP} - R_P)$ can be made, where A is the area of CPP current flow.

Before taking a closer look at the 2CSR model it is important to define several parameters used to make calculations and model the multilayer. (This review follows

the notation and spirit of the original work by Fert as well as several review papers on the matter [24, 26, 28].) The resistivity of each channel in a F layer is denoted as ρ_F^{\uparrow} for electrons with their spins parallel to the magnetization and ρ_F^{\downarrow} for electrons with their spin parallel anti-parallel to the magnetization. A useful parameter for such a material is

$$\rho_F^* = \frac{\rho_F^{\dagger} + \rho_F^{\downarrow}}{4} \tag{1.7}$$

which provides a measure of the average resistivity for spin up and down electrons. In addition, the spin asymmetry variables α , and β are also important:

$$\alpha = \frac{\rho^{\downarrow}}{\rho^{\uparrow}} \; ; \tag{1.8}$$

$$\beta = \frac{\rho_F^{\downarrow} - \rho_F^{\uparrow}}{\rho_F^{\uparrow} + \rho_F^{\downarrow}} = \frac{\alpha - 1}{\alpha + 1} \ . \tag{1.9}$$

The resistance of each channel can then be related to ρ^* by using β :

$$\rho_F^{\uparrow} = 2\rho_F^*(1-\beta) ; \qquad (1.10)$$

$$\rho_F^{\downarrow} = 2\rho_F^*(1+\beta) \ . \tag{1.11}$$

It is important to note for non-magnetic materials such as Cu that $\beta = 0$, giving

$$\rho_N^{\uparrow\downarrow} = 2\rho_N^* \tag{1.12}$$

There is an interface resistance counterpart to β . Instead of a resistivity, γ refers to a specific resistance AR (= Area × Resistance; A is the area of current flow). γ relates the average AR^{*}_{F/N} to AR[†]_{F/N} for the individual spin up and spin down channels.

$$AR_{F/N}^{\uparrow} = 2AR_{F/N}^{*}(1-\gamma) \tag{1.13}$$

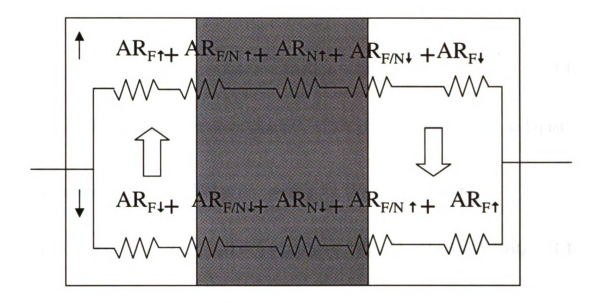


Figure 1.9: A diagram of the two current series resistor model for the AP state. The current is divided into two channels: spin up channel (top) and spin down channel (bottom). One adds the series resistances for each channel and then combines the series resistances as two resistances in parallel to produce the overall resistance for both the AP states.

$$AR_{F/N}^{\downarrow} = 2AR_{F/N}^{*}(1+\gamma)$$
 (1.14)

Using these relations one can determine the resistivity for a F/N multilayer in terms of ρ_N^* , ρ_T^* , γ , β , and $AR_{F/N}^*$ where the subscripts denote which layer the parameter represents.

If one takes the case of a F/N/F multilayer with layer thicknesses t_F , t_N , and t_F respectively (shown in Figure 1.9), the calculation is done in the following way. Taking the case of the spin up channel in the AP state, one adds up the various resistances from both the bulk and interface.

$$AR_{AP}^{\dagger} = 2\rho_F^*(1-\beta)t_F + 2AR_{F/N}^*(1-\gamma) + 2\rho_N^*t_N + 2AR_{F/N}^*(1+\gamma) + 2\rho_F^*(1+\beta) \quad (1.15)$$

This can be simplified to

$$AR_{AP}^{\dagger} = 4\rho_F^* t_F + 4AR_{F/N}^* + 2\rho_N^* t_N \qquad (1.16)$$

Then one calculates the spin down channel, which gives the same result as Equation 1.16.

Calculating for the parallel state one gets for the spin up channel:

$$AR_P^{\uparrow} = 2\rho_F^*(1-\beta)t_F + 2AR_{F/N}^*(1-\gamma) + 2\rho_N^*t_N + 2AR_{F/N}^*(1-\gamma) + 2\rho_F^*(1-\beta)t_F , \quad (1.17)$$

while the spin down channel gives:

$$AR_P^{\downarrow} = 2\rho_F^*(1+\beta)t_F + 2AR_{F/N}^*(1+\gamma) + 2\rho_N^*t_N + 2AR_{F/N}^*(1+\gamma) + 2\rho_F^*(1+\beta)t_F . \quad (1.18)$$

The overall resistance of each magnetic state is a parallel addition of the spin-up and spin-down channels resistances. The resistance of the parallel state, AR_P , is:

$$AR_P = \frac{AR_P^{\uparrow} AR_P^{\downarrow}}{AR_P^{\uparrow} + AR_P^{\downarrow}} \,, \tag{1.19}$$

and the specific resistance of the AP state, AR_{AP} , is computed in the same manner. $A\Delta R$ is then just $AR_{AP} - AR_P$, and the GMR ratio is $\equiv (AR_{AP} - AR_P)/AR_P$.

This model holds as long as $l_{sf}\gg$ t, as shown by Fert and Valet [24]. However, for l_{sf} not \gg than t_F (such as in the material Ni₈₄Fe₁₆) one must take into account spin relaxation [24,25]. The 2CSR model must then be modified, and for many cases only numerical solutions exist. However, for a F/N multilayer with M F/N bilayers, where M is large, an algebraic solution exists [24]:

$$AR_{P,AP} = M(AR_0 + 2AR_{P,AP}^{SI})$$
 , (1.20)

with
$$AR_0 = (1 - \beta^2)\rho_F^* t_F + \rho_N^* t_N + 2(1 - \gamma^2)AR_{F/N}^*$$
 (1.21)

and

$$AR_{P}^{SI} = \frac{\frac{(\beta - \gamma)^{2}}{\rho_{N}^{*} l_{sf}^{N}} \coth\left[\frac{t_{N}}{2l_{sf}^{N}}\right] + \frac{\gamma^{2}}{\rho_{F}^{*} l_{sf}^{F}} \coth\left[\frac{t_{F}}{2l_{sf}^{F}}\right] + \dots}}{\frac{1}{\rho_{N}^{*} l_{sf}^{N}} \coth\left[\frac{t_{N}}{2l_{sf}^{N}}\right] \frac{1}{\rho_{F}^{*} l_{sf}^{F}} \coth\left[\frac{t_{F}}{2l_{sf}^{F}}\right] + \dots}} \Rightarrow \frac{1}{\frac{1}{\rho_{N}^{*} l_{sf}^{N}} \coth\left[\frac{t_{N}}{2l_{sf}^{N}}\right] + \frac{\beta^{2}}{AR_{F/N}^{*}}}}{\dots + \frac{1}{AR_{F/N}^{*}} \left\{\frac{1}{\rho_{N}^{*} l_{sf}^{N}} \coth\left[\frac{t_{N}}{2l_{sf}^{N}}\right] + \frac{1}{\rho_{F}^{*} l_{sf}^{F}} \coth\left[\frac{t_{F}}{2l_{sf}^{F}}\right]\right\}}$$

$$(1.22)$$

$$(\beta - \gamma)^{2} + 1 \left[\frac{t_{N}}{N}\right] + \gamma^{2} + 1 \left[\frac{t_{F}}{N}\right] + \frac{1}{N} \left[\frac{t_{F}}{N}\right] + \frac{$$

$$AR_{AP}^{SI} = \frac{\frac{(\beta - \gamma)^{2}}{\rho_{N}^{*} l_{sf}^{N}} \tanh \left[\frac{t_{N}}{2l_{sf}^{N}} \right] + \frac{\gamma^{2}}{\rho_{F}^{*} l_{sf}^{F}} \coth \left[\frac{t_{F}}{2l_{sf}^{F}} \right] + \dots}}{\frac{1}{\rho_{N}^{*} l_{sf}^{N}} \tanh \left[\frac{t_{N}}{2l_{sf}^{N}} \right] \frac{1}{\rho_{F}^{*} l_{sf}^{F}} \coth \left[\frac{t_{F}}{2l_{sf}^{F}} \right] + \dots}} \Rightarrow \frac{\dots + \frac{\beta^{2}}{AR_{F/N}^{*}}}{\dots + \frac{1}{AR_{F/N}^{*}} \left\{ \frac{1}{\rho_{N}^{*} l_{sf}^{N}} \tanh \left[\frac{t_{N}}{2l_{sf}^{N}} \right] + \frac{1}{\rho_{F}^{*} l_{sf}^{F}} \coth \left[\frac{t_{F}}{2l_{sf}^{F}} \right] \right\}} . (1.23)$$

Both the two current series resistor model and the extension for short l_{sf} are supported by experimental evidence [15, 26].

Chapter 2: Sample Fabrication

2.1 Introduction

All samples were prepared and measured at Michigan State University. Although there were four separate procedures for lithography, each sample underwent the same basic fabrication procedure (Figure 2.1). The samples (in sequential processing order) were: cleaned, sputtered with a multilayer, lithographically patterned, etched, planarized with an insulating layer, cleaned to remove the lithographic pattern, and finally sputtered with top Nb leads. The details of each specific sample type, or category, are contained below.

2.2 Types of Samples

Four categories of photolithography sample were made (Figure 2.2). The samples differed in the top portion of the multilayer or "cap" and whether the giant magnetoresistance structure was etched or not. The multilayer consists of a bottom, 250 nm thick Nb layer, followed by an exchange bias spin valve (EBSV) or a hybrid spin valve (HSV). The exchange bias spin valve structure is (beginning with the previously mentioned Nb layer): Nb (250) / Cu (10) / Fe₅₀Mn₅₀ (8) / F (x) / Cu (20) / F (x) / Cu (10), where $F = Ni_{84}Fe_{16}$ or $Co_{91}Fe_{9}$, x = 3-40, all units are nm. The HSV structure is: Nb (250) / Cu (10) / F (x) / Cu (10) / F (y) / Cu (10), x = 3-30 and y is 5-30, but $x \neq y$. The EBSV uses the Fe₅₀Mn₅₀ layer, which is an antiferromagnet, to bias the adjacent F layer's magnetization in a 'pinned' direction. This causes the coercivity of that F layer to be very large. The other F layer is free, or unpinned, and has a relatively low coercivity. For low magnetic fields the free layer will align with the applied magnetic field while the pinned magnetization will remain fixed.

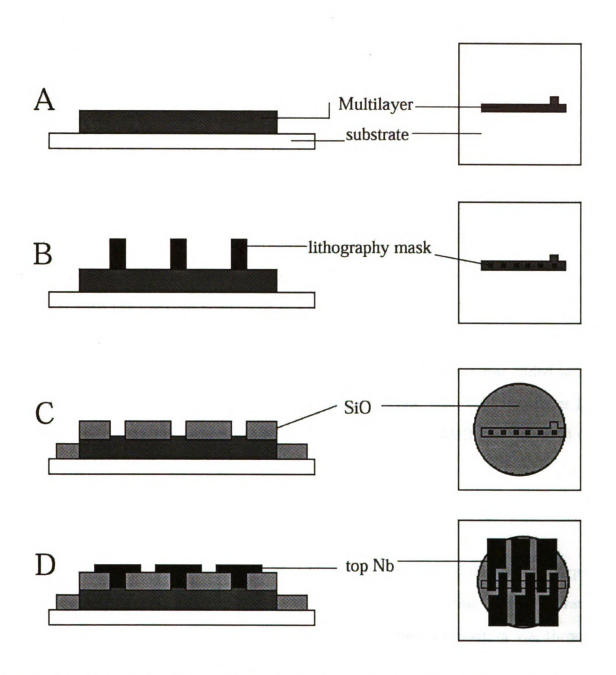


Figure 2.1: An overview of the fabrication process. A side profile is provided on the left (only half of the lithographic features are shown to conserve space), and a complete top view is provided on the right. The dimensions of the system are not to scale. A multilayer is sputtered onto a cleaned substrate (A). A lithographic pattern/mask is placed onto the multilayer (B). A portion of the multilayer is etched away, an insulting layer deposited and the lithographic pattern removed (C). The top contacts are sputtered onto the sample (D).

This setup allows good control of the anti-parallel and parallel states for GMR. The HSV uses different layer thicknesses to achieve the same results. Since layer thickness (especially when the lateral layer dimensions are small) will affect the coercivity, by choosing one layer to be very thin and one very thick, good control of the anti-parallel state can also be achieved using this method. Each spin-valve was then finished with one of two types of "caps." A layer of Au, 15 nm thick (although for some samples this was increased to up to 150 nm), formed a type-I cap (C_I) . A type-II cap (C_{II}) was formed by a trilayer of Au (10 nm)/ Nb (20-250 nm), Au (15 nm). (The final Au layer on the surface prevents oxidation during lithographic processing.) The C_I cap was easy to process, requiring no etching, but needed extensive cleaning to make contact with the final Nb layer. The C_{II} cap required etching, but more easily provided low contact resistances with the final Nb layer. Each spin valve and its cap were processed using techniques described below. A final Nb layer was added to the top of the multilayer stack to complete the sample. Thus, each final multilayer has three parts: 1) the initial(bottom) Nb layer followed by the GMR spin valve; 2) the cap; 3) the top Nb layer.

2.2.1 Type-I Samples

Type-I samples were multilayer with a C_I cap of 15 nm Au on the surface. Type-I samples had the photomask placed on the Au, and the insulating layer evaporated onto the entire sample. Removal of the photoresist exposed a trench, or via, through the insulating layer to the multilayer. Through this via, sputtered Nb (through a shadow mask) would make electrical contact with the multilayer below. This type of sample was simple to process, but could suffer from interface resistance problems if the Au/Nb interface was polluted due to insufficient cleaning.

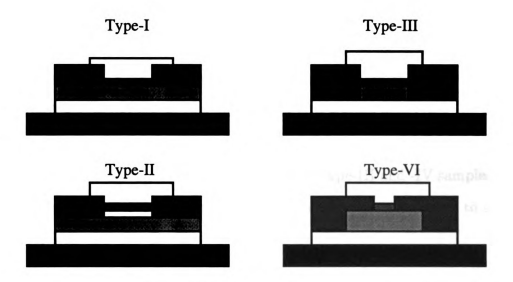


Figure 2.2: An overview of the different types of samples. Type-I has contact made to a Au capping layer. Type-II has a partially etched Au/Nb/Au cap. Type-III has the entire multilayer etched. Type-IV has a separate contact geometry on top of a patterned multilayer

2.2.2 Type-II Samples

Type-II samples consisted of multilayers capped with a C_{II} cap. After placing a photolithography mask on the sample, the Nb/Au part of C_{II} was removed by various methods depending on the thickness of each layer. Initially, Au was wet etched with a KI / I_2 solution. However, this solution also attacked other portions of the multilayer and therefore an ion milling process was introduced that did not have these difficulties. The ion mill was then exclusively used for later samples. The Nb layer, if 20 nm or less, was also ion milled. If thicker than 20 nm, the Nb layer would take too long to remove using ion milling (up to several hours) and was instead removed by reactive ion etching (RIE). This entire process left a short column of Nb(x)/Au(20 nm), where x = 20 - 100 nm, underneath the patterned features. An insulating layer was evaporated and the lithographic features were removed. Last, the top Nb layer was sputtered onto the sample. This type of sample, in theory, makes it easier to eliminate contact resistances, since the Nb/Au/Nb interface should be

superconducting by proximity [29,30]. In addition, the important F/Au/Nb interface is in effect 'buried,' and not exposed to lithographic processing. Type-II samples were proposed before type-I samples, but due to problems with Reactive Ion Etching (RIE), type-I samples were developed to eliminate the RIE step. These problems were later solved (the details can be found in the reactive ion etching section). Both type-I and -II samples were integral in the development of the type-III and -IV samples. Type-I and -II samples were used exclusively in CPP-transport measurements to study the $A\Delta R$ behavior.

2.2.3 Type-III samples

The type-III and type-IV geometries were used to detect domain wall trapping. Whereas type-I and -II samples always employed square lithographic patterns, type-III samples had a more complex wire geometry (Figure 2.3). Typically, the type-III samples were multilayers with a C_I cap for photolithography and a modified C_I cap (with cap Au now 100-150 nm thick) for e-beam lithography. The increase in Au thickness was needed because electrical contact into a 'trench' or via becomes difficult or impossible once the dimensions are reduced below 2 μ m. The thicker Au creates a 'proud' column (Figure 2.4) that, after ion milling, exceeds the level of the insulating layer and avoids the contact problem with vias (Figure 2.2 shows a photolithgraphy sample and thus shows a via instead of a proud column). After the lithographic mask was placed onto the sample (this was done by both e-beam and photolithography), the entire GMR spin-valve was ion milled to the bottom Nb superconductor. An insulating layer was then evaporated onto the sample. Following removal of the mask, Nb was sputtered onto the sample. This left the entire in-plane geometry of the patterned multilayer in contact with the top superconductor. In order to study only part of the wire, it was necessary for the superconducting contact and the spin-valve to have different geometries.

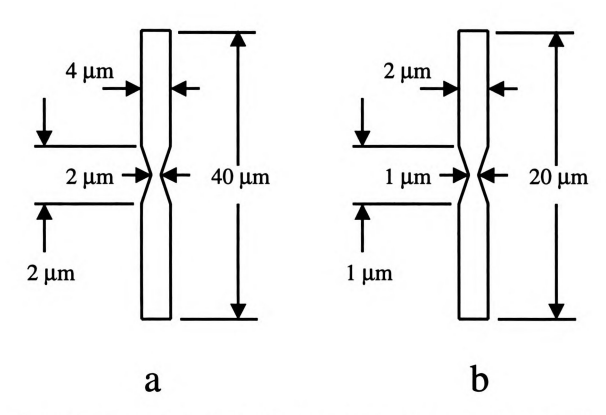


Figure 2.3: A diagram of the mask for fabricated wires with a neck. There were two sizes of wire designed. Mask b is exactly a factor of two smaller than a. Each is symmetric about the notch region.

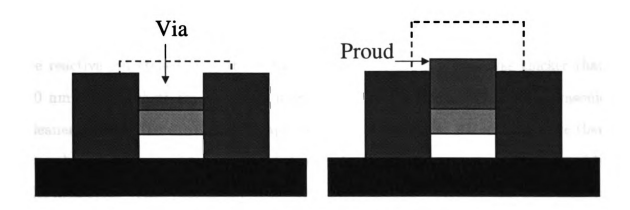


Figure 2.4: The difference between a via and a proud column. A via is a trench or window in the insulating layer through which contact with the top superconductor (dashed line) is made. A proud column sticks above the insulating layer. Proud columns become necessary when the feature size is below 2 µm.

2.2.4 Type-IV samples

Type-IV samples underwent type-III processing up to and including the removal of the lithographic mask, and then a second lithography step was used to produce a top contact of different geometry (a square) than the original patterned multilayer feature from the first set of lithographic procedures. This small square type-I contact allowed study of particular regions of the previously patterned wire structure. The second lithographic pattern was placed on the previously patterned features, SiO was deposited, the lithographic mask was then removed and finally the top Nb layer was deposited. In this dual procedure, a variety of different multilayer and contact geometries could be produced.

2.3 Procedures

2.3.1 Substrate Cleaning

The sample fabrication process began by cleaning sample substrates in a class 100 cleanroom (measured to be class 100, although certified class 1000). Either silicon (100) or c-axis oriented sapphire substrates were used. Silicon was used for the majority of samples. Sapphire was employed only for samples that needed to be reactive ion etched (i.e., that had a Nb layer in the cap that was thicker than 20 nm). The substrates were first immersed in Alconox[®] at 40°C. An ultrasonic cleaner agitated the substrates for approximately 15 minutes. All samples were then rinsed in water to avoid a reaction between the Alconox[®] and the acetone used in the next step. When mixed, Alconox[®] and acetone produce a dark film that hinders lithography because it is difficult to remove. After rinsing with water, substrates were placed in acetone at 40°C, agitated in an ultrasonic cleaner for 15 minutes, dried, and visually inspected using a Olympus BX60 optical microscope at 20-100X. Samples

were scrubbed in acetone by rubbing the surface with a Q-tip and inspected again. If non-removable defects such as scratches were present the substrate was discarded. Substrates that passed inspection were placed in isopropyl alcohol (IPA) at 40°C and agitated in the ultrasonic cleaner for 15 minutes. Finally, samples were immersed in deionized water at 80°C for at least 15 minutes and left in water until placed in the ultra high vacuum system for sputtering (a time of minutes to a few hours at most). Thus samples were not stored for long periods of time in this cleaned state.

2.3.2 Sputtering

Sputtering was done in an ultra high vacuum system equipped with a cryopump capable of producing pressures of 10⁻⁸ Torr after 24 hours of pumping [31]. Sample substrates were loaded onto a position and movement assembly (SPAMA) plate that contained eight holders, each holder having the capability to hold two samples. The holders sat in holes in the SPAMA plate and were attached to the plate via two screws. In addition, a circular stainless steel rotating mask was attached to the base of the sample holder which allowed the user to expose or protect the substrate by rotating the mask to an open or closed position (Figure 2.5). A separate shadow mask (stainless steel) was placed in the holder first, allowing the formation of a pattern during sputtering. The sample substrate was placed on top of the shadow mask. Copper heat sinks were placed on top of the substrates, and the entire stack was held in place by removable "bridges" that attached to the holder with screws, to apply pressure to the top of the heat sink (Figure 2.6). Any alignment of the shadow mask with a previously made pattern on the substrate had to be done visually and before the entire stack was secured.

After the substrates were loaded onto the SPAMA plate, the plate was placed above a system of movable chimneys that allows the user to control sample exposure

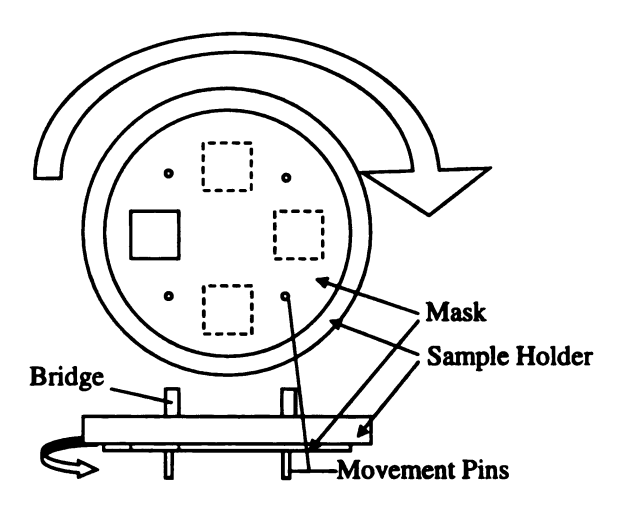


Figure 2.5: The layout of the mask system. The rotating mask (inner circle) is rotated to expose a sample to the sputtering plasma. A shadow mask (not shown) over the substrate defines the actual pattern. The 12 o clock and 6 o clock positions correspond to a closed position while the 3 o clock and 9 o clock position will expose the sample. The rotating mask is aligned by lining up the pins of the rotating mask to be in line with the bridges holding down the samples. The mask here is shown in the 9 o clock position while the others are represented with dashed lines.

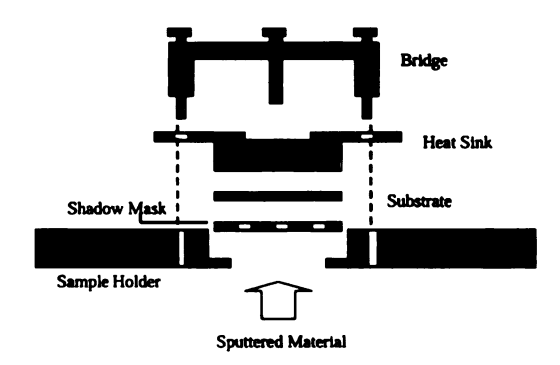


Figure 2.6: A exploded view of the sample holder. The bridge clamps the heat sink/substrate/shadow mask together. The assembly is attached with screws to the sample holder through the bridge. Each sample holder is designed to hold two assemblies.

to the sputtered material. The system was pumped down to 4×10^{-8} Torr. A overnight baking of the chamber sped up the pump down process. Before sputtering, a cold trap using liquid nitrogen was activated to reduce the overall pressure to 2×10^{-8} Torr.

Sputtering was done at an Ar pressure of 2.5 mTorr. Samples were cooled to -30° C by a capillary system using cold compressed flowing N₂ gas. The pressurized gas is allowed to expand in a network of capillary tubes, causing the system to cool. A purifier produces ultra-pure Ar gas for sputtering. Samples were sputtered at temperatures between -30 and 30°C. The sample to be made was exposed by rotating the bottom mask to an open position using a wobble stick. The holder was then rotated, via the SPAMA plate, over the gun containing the material to be sputtered; and, when in place, the system of chimneys would rotate to allow deposition for a specified time. When the desired thickness was reached, the chimneys were rotated to their previous position to prevent deposition. The SPAMA plate was then rotated so that the sample was over the next sputtering gun. This was repeated until the sample was finished, and then the rotating mask positioned to prevent further deposition on the sample.

Final Top Nb

When depositing the top Nb layer on a sample with completed microfabricated features, a special alignment step was necessary. As shown in Figure 2.7, the protrusion on the sample strip had to line up with the first hole in the top contact shadow mask. The layout of the lithographic features was intentionally designed to have one sample contact within each top Nb window of the shadow mask.

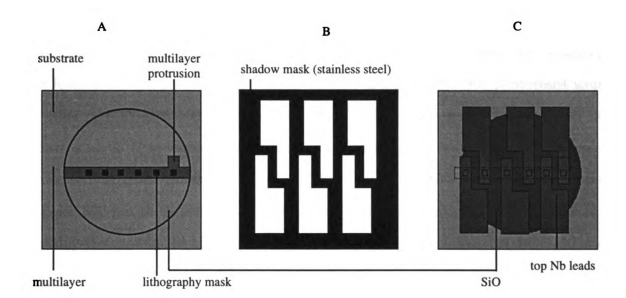


Figure 2.7: A layout of the mask system to deposit top Nb leads. (A) The multilayer with patterned mask features (exaggerated size, in black). Each feature is spaced so that when the far right opening in the shadow mask (B) is lined up with the protrusion in the multilayer (A), the individual exposed contact areas will each fall within a single Nb contact (C)

2.4 Lithographic Procedures

The lithographic procedures described here employ a patterned resist mask on the sample. Depending on the geometry and processing of the mask, the same exposure procedure can create different types (Type-I,-II, etc...) of samples. Lithography defines small features from 75 to $.3~\mu m$

2.4.1 Photolithography

Photolithography began by placing a sample with a sputtered multilayer on a vacuum spinner. The vacuum in the spinner chuck holds the sample in position on top of a chuck while the sample is spun. A large drop, ~.1mL, of Shippley 1813 or 1805 photoresist is placed by a pipette on the surface of the sample, and the sample is immediately spun for 60 seconds. The rate of spinning, in addition to the type of photoresist, affects the thickness of the photoresist layer. For initial samples, Shippley

1813 resist was spun at a rate of 4000 rpm to give a photoresist thickness of 1.3 to 1.5 μ m. (Measured by exposing large features, developing the photoresist and scanning the features with a profile stylus.) Later samples had Shippley 1805 photoresist spun at 5000 rpm to give a thickness of 500 nm. The samples were then baked for 40 minutes at 95°C to harden the photoresist. Feature sizes from 10 to 75 μ m were processed using the thicker photoresist. When smaller 1- μ m features were made, the thinner 500 nm thick photoresist was used. For a contact aligner, diffraction is the limiting factor, and the critical dimension, or smallest feature size, can be estimated as:

$$d = \sqrt{k \times \lambda \times z} \tag{2.1}$$

where k is 1.6 (index of refraction for the photomask), λ is the wavelength of radiation, and z is the distance between the mask and substrate. Using λ of 365 nm and z of 1.5 μm gives d \approx 1 μm . A z of .5 μm gives a d \approx .5 μm . Physical limitations, such as buildup of photoresist on the corners of the substrate and the inability of the substrate to flex which allows better contact with the mask, limited the resolution of the 1.5 μ m photoresist layer to 7-10 μ m and the 500 nm photoresist layer to 1 μ m. After baking, the samples were placed in a contact mask aligner (ABM, INC). Using a photomask from Align-Rite corporation, the samples were exposed in selected areas to ultraviolet radiation of wavelength 365 to 400 nm. Both of the photoresists were 'positive,' meaning that the photoresist forms strong chemical bonds (crosslinked). When exposed to ultraviolet light, the chemical bonds of the positive photoresist break down, making the exposed resist soluble in certain chemicals known as developers. For these photoresists the developer was KOH (Shippley 452 developer). The portion of resist underneath the mask is still crosslinked and insoluble in the developer. Two different photomasks were used to expose patterns on the photoresist for our samples. Both photomasks were clear field masks. That is the majority of the mask is clear or transparent to ultraviolet light, while the features are dark chrome. The first

photomask (layout shown in Figure 2.8 and Table 2.1) had only square patterns ranging from 75×75 to $6 \times 6 \mu$ m. The second photomask (layout shown in Figure 2.9 and Table 2.2) had square features from 75×75 to $2 \times 2 \mu$ m in addition to two wire geometries (Figure 2.3). The change in photomasks was made to produce dimensions closer to the theoretical limit of the contact alignment system and give the possibility to pattern wire geometries of appropriate size in the multilayer for domain-wall trapping. In addition, the features on the second mask were produced with a smaller spot size (the masks are produced with dedicated electron-beam writers) which made the smaller features at higher resolution

After aligning the mask so that a pillar was aligned with the protrusion of the 1 \times 10 mm strip, the samples were exposed to ultraviolet light for a fixed period of time. The samples with 1.5 μ m thick photoresist were exposed for 6 seconds. The samples with 500 nm thick photoresist layer were exposed for 1.5 seconds. The exposed photoresist was removed using Shippley 452 developer (KOH solution). Each sample was placed in a bath of developer at room temperature for 25 seconds, next immediately placed in a second bath of developer for an additional 25 seconds, and then rinsed in a bath of deionized water. The two developer steps were used to avoid contamination by removed photoresist redepositing on the surface of the multilayer. Ideally, this process will reproduce the mask pattern on the photoresist. The photoresist is now ready to be used as a mask for selecting which areas of the sample will be processed. Any area underneath the photo resist is protected from processing while the photoresist remains.

2.4.2 Electron Beam Lithography

When the limits of the photolithography equipment were reached, the procedures employed were adopted to electron beam (e-beam) lithography. The basic principle of the photolithography employed for this research was that the photoresist itself was

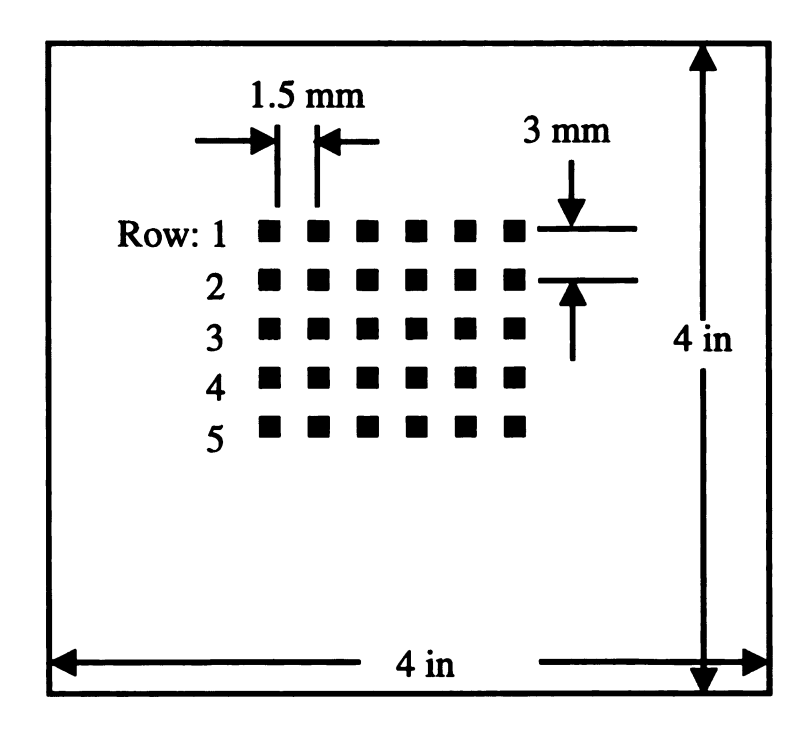


Figure 2.8: A diagram of the layout and dimensions of the first photomask. A single array of features was arranged as shown. The dimensions of the features are listed in Table 2.1

_							
1	Row 1	75	75	75	75	75	75
	Row 2	75	40	40	40	40	75
١	Row 3	75	20	20	20	20	75
	Row 4	75	6	6	6	6	75
١	Row 5	75	75	40	20	6	75

Table 2.1: The side dimension of each square listed for the features on the photomask that is shown in figure 2.8. All units are in microns.

Row 1	75	75	75	75	75	75
Row 2	75	10	10	10	10	75
Row 3	75	5	5	5	5	75
Row 4	75	2	2	2	2	75
Row 5	75	20	10	5	2	75
Row 6	75	W40	W40	W20	W20	75
Row 7	75	W40	W40	W20	W20	75

Table 2.2: The side dimension of each square listed for the features on photomask 2 that is shown in figure 2.9. All units are in microns. W40 and W20 refer to the wire geometries of 40 microns length and 20 microns length, respectively, shown in Figure 2.3.

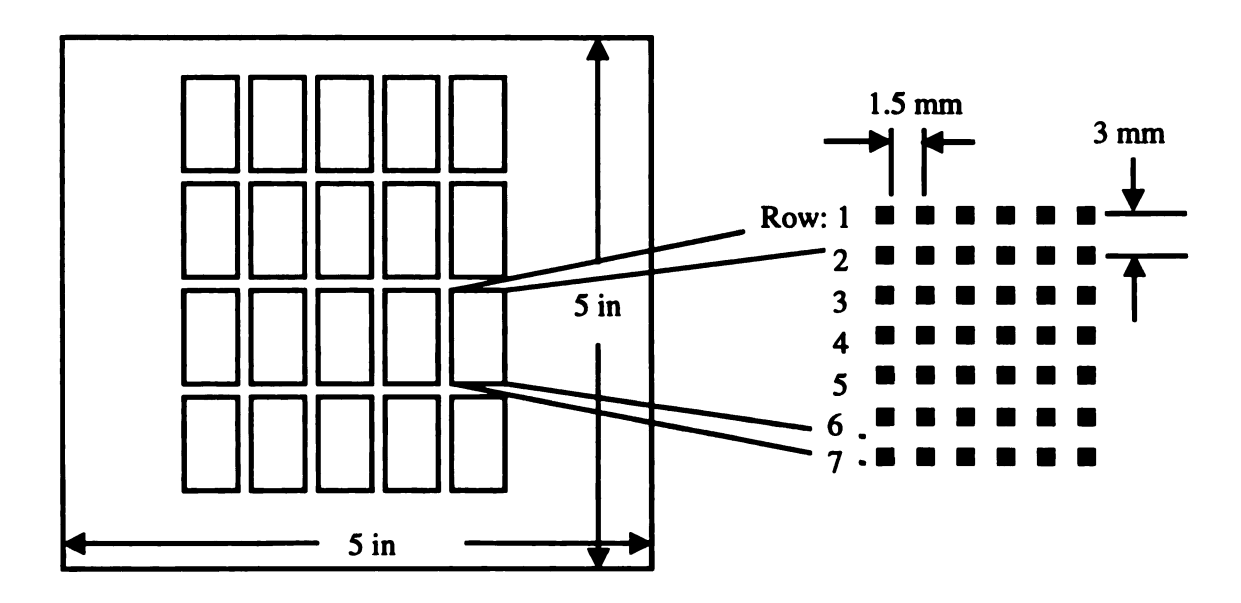


Figure 2.9: A diagram of the layout and dimensions of the second photomask. On this mask, the array was repeated multiple times on the mask. The dimensions of the features are listed in Table 2.2

the mask that protected the multilayer or contact area. Because the nature of e-beam lithography is one of much smaller exposed areas and since a reliable negative resist process is difficult to develop, the e-beam mask instead patterns a secondary mask of Al that protects the sample in a similar manner as the photoresist. The actual limits of e-beam lithography are a function of the spot size which was much smaller (5 to 10 nm in diameter) than the feature size (500 to 2000 nm). Even though the spot size was much smaller than the pattern, there are still parameters which need to be adjusted to produce well-defined exposed areas. This was done by varying the parameters of the exposure, such as the line to line and center to center spacing as well as the dosage, and adjusting or tweaking the layout of the pattern. The e-beam exposure has a proximity effect in that regions near the electron beam also get exposed. In order to establish a well defined pattern, a small amount of trial and error is needed. To select the correct exposure setting a line to line distance was chosen. Then a series of identical patterns was made using dosages from 200 to 500 μ C/cm². This process was repeated for the next line to line spacing to cover all the combinations of line

to line spacing and dosage. In this manner the combination of 247 Å line to line spacing and 300 μ C/cm² dosage were selected as producing the best pattern. Since the pattern itself was simple and relatively large compared to the beam spot size, no further modification of the writing pattern was needed to correct for proximity effects. To create this mask, a layer of 9% copolymer in chlorobenzene was spun at 3000 rpm onto the sample and baked for at least 1 hour at 155°C. (Copolymer is polymethyl methacrylate (PMMA), 495k molecular weight, and 8.5% methacrylic acid (MAA).) The sample was spun again, this time with 2% PMMA (in chlorobenzene) at 4900 rpm, and again baked at 155°C for at least 1 hour. The bilayer resist was then exposed in a JOEL 840 electron microscope with a dose of 300 μ C/cm² for features that were in the .5 - 2 micron range at a 5 pA current. Since the current varied from session to session, it was measured first, and the writing system would then adjust the timing to produce an exposure of 300 μ C/cm² at 1000X. The sample was then developed for 65 seconds in a 1:3 methyl isobutyl ketone (MIBK) to IPA mixture. The copolymer is much more sensitive to secondary electrons from the multilayer and substrate than the PMMA, and thus more of the copolymer is exposed, producing a large undercut in the resist system after developing (Figure 2.10). After developing, the sample was rinsed in IPA for 25 seconds and water for 30 seconds. The samples were then dried and placed in a Edwards evaporator to have aluminum deposited.

Aluminum was evaporated at setting 2.2 A, giving a deposition rate of 6-10 Å per second. An Al layer, 150 nm thick, was deposited onto the sample. After removal from the deposition system, the sample was placed in acetone at 40°C to remove the Al that was not in contact with the surface. After approximately 1 hour, the excess Al was removed and the mask was complete for further processing procedures.

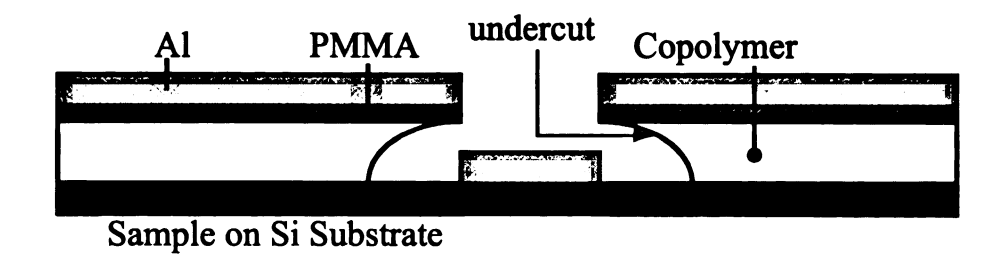


Figure 2.10: The bilayer of PMMA and Copolymer after evaporation. The development removes the copolymer more than the PMMA causing the undercut. The difference in removal is due the copolymer's stronger sensitivity to the backscattered electrons from the substrate. This allows the deposited Al feature, patterned from the PMMA, to be isolated from the rest of the evaporated material. The bilayer will be removed in the next step by Acetone, and only the Al on the sample will remain.

2.4.3 Etching

Once a sample had a lithographic mask in place portions of the thin film were removed using one or both of the following techniques. Reactive Ion Etching (RIE) was the only practical choice to remove thick (> 200 nm) Nb layers. Ion milling removed thin (≤ 20 nm) Nb and any other thin metal film.

Reactive Ion Etching

Samples to be reactive ion etched were taken to the Plasma-Therm BatchTop Reactive Ion Etcher. This machine is capable of producing flows of SF₆ from 0 to 50 sccm and had a base pressure of 20 mTorr. Before the etching run, the entire chamber was cleaned to remove debris from previous samples. The cleaning procedure began by pumping down the vacuum chamber of the RIE to 20 mTorr. SF₆ was then bled into the chamber at 5 sccm. The RIE was turned on with a power of 50 W. This initial cleaning etch was performed for 10 minutes to remove any leftover debris from previous SF₆ etches. After this, the chamber was purged with N₂ gas and again pumped to the base pressure of 20 mTorr. 5 sccm of SF₆ and O₂ each were bled into the chamber. The plasma cleaning was started with a power of 50 W and again allowed to run for 10 minutes to remove hardened debris that SF₆ alone could not

remove. The chamber was then purged and bled with pure O₂ at 5 sccm. This final O₂ etch was designed to remove any organic material left in the chamber and was done with a power of 20 W for 10 minutes. This entire procedure was successful at providing a clean system, although an ideal finishing step would be a physical bombardment with Ar-plasma. (Ar gas was not installed on this system.) (Although developed independently, a more detailed discussion of why this cleaning procedure works is described elsewhere [32].)

After purging the chamber with N_2 gas and raising the pressure back to an atmosphere (again with N_2 gas), the sample was placed in the vacuum chamber of the RIE. The top Nb layer was removed by using a 5 sccm flow of SF_6 at a pressure of 60 mTorr with a power of 50W. The etch was run until the multilayer was viewed to have changed color—a sign the Nb was completely removed. The actual rate of etching was not calculated, because when the Nb was removed, the etch will not continue; SF_6 will not etch copper or Au under these conditions. Since SF_6 also reacts with Si, SiO and SiO₂, sapphire substrates had to be substituted for silicon to prevent redeposition of Si etch byproducts on top on the multilayer.

This redeposition of etched Si onto the substrate, including the multilayer, led to the development of type-I samples where no processing of the cap was needed. After fine tuning the cleaning process and switching to sapphire substrates, successful type-II samples were made using RIE. However, the RIE still did not give consistent results, so the process of etching Nb was moved to ion milling, which gave more consistent results.

Ion Milling

Samples which were ion milled were placed in holders consisting of a mask/sample holder, copper heat sink, and magnetic disk. The holders were placed in a vacuum chamber containing an evaporation boat for SiO and a 3 cm ion source for ion milling

	Nb	Au	Cu	CoFe	Py	FeMn
						5.20
20 mA	3.92	38.5	25.8	9.0	13.1	17.2

Table 2.3: Ion milling rates in Å/s for various metals at 10 mA and 20 mA current. For 10 mA, The Ar flow was 3 sccm and for 20 mA, 6 sccm.

(Commonwealth Scientific Corporation). The system was continuously pumped down to $< 1 \times 10^{-6}$ Torr. Samples were loaded through a load lock with a magnetic arm.

Ion milling was performed at a base pressure $< 5 \times 10^{-6}$ Torr. To start the ion milling, Ar gas was bled into the chamber at 3 or 6 sccm giving a pressure of 3×10^{-4} Torr. A shutter shielded the samples while the ion gun was started. The current was first increased to the desired level, either 20 or 10 mA and the voltage was then increased to 500V. When ready, the samples were rotated via the sample plate over the ion mill with the shutter open (Figure 2.11). Although sample heating took place, the temperature of the substrates was measured to remain below 40°C for 3 sccm of Ar flow and 70°C for 6 sccm Ar flow. Ion milling rates were calibrated beforehand, and the sample exposure was timed to mill to the desired thickness. Ion milling rates were measured by etching single layers of material patterned with a photo mask and then etched for a predetermined amount of time. After etching, the photomask was removed and the resulting profile height measured with a profile stylus. This was done for multiple time intervals for each material, and then a linear regression was plotted to calibrate the milling rate [33]. Those rates for specific conditions are listed in Table 2.3.

2.4.4 SiO Evaporation

Once the samples were etched, an insulating layer of SiO was evaporated to planarize and insulate the microfabricated features from the as-yet undeposited top Nb-layer. (The material is only nominally SiO; it actually is SiO_x , with x=1 to 1.5, measured via its index of refraction [34].) If one uses the same deposition rate and

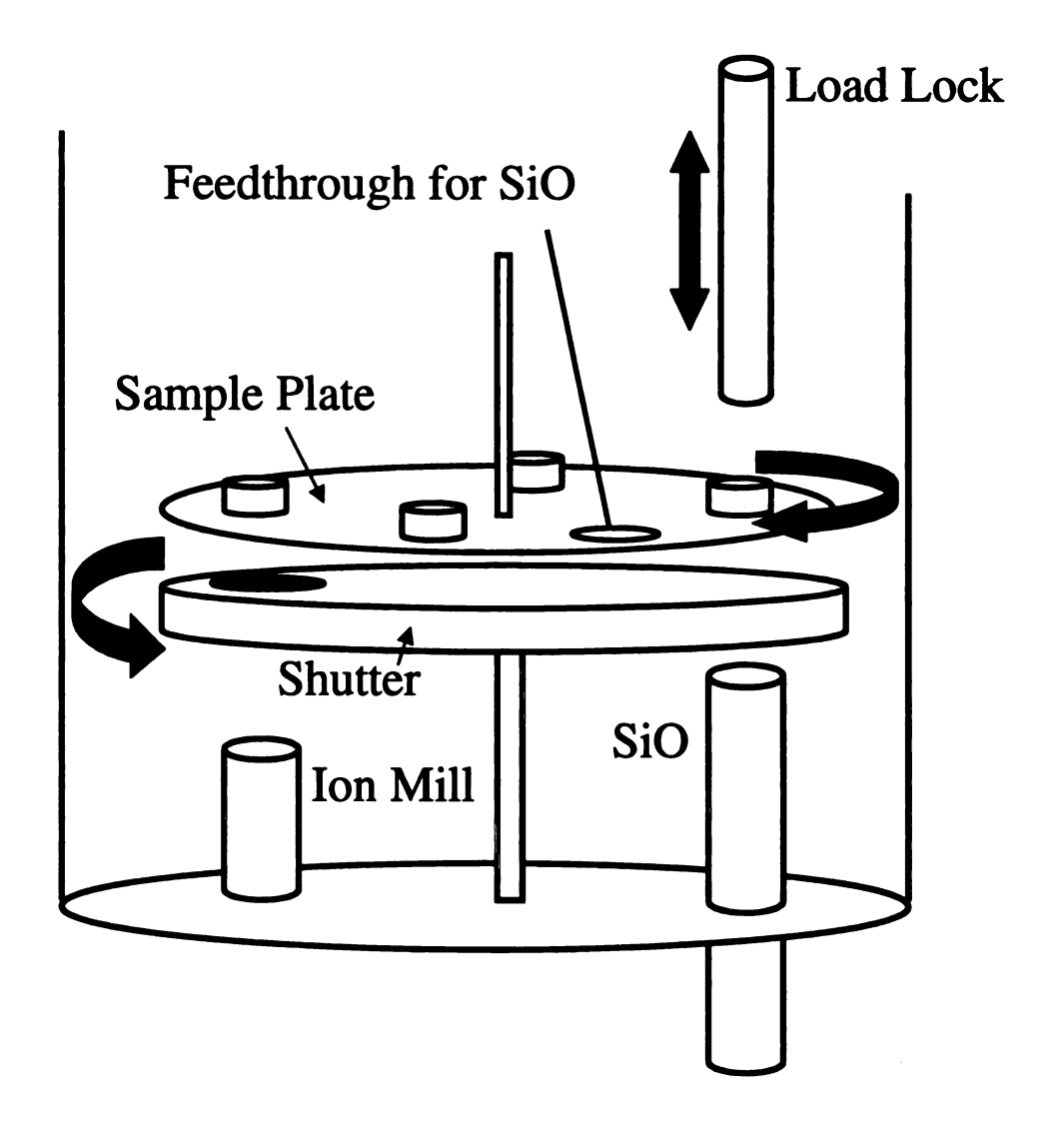


Figure 2.11: The setup of the small chamber. The samples can be rotated to the desired position on the sample plate. A shutter, independent of the sample plate, can also be rotated to an open or closed position depending on source to be run. The magnetic arm for loading samples through a load lock is in the upper right.

pressure, fairly reproducible results can be achieved.) Deposition of SiO took place in the same chamber as ion milling (Figure 2.11) at pressures $< 2 \times 10^{-6}$ Torr. A special tantalum boat (Figure 2.12) was slowly heated at a rate of .15 A per 30 seconds (primary current) using a variac. When the primary current reached 2.66 A, the boat was sufficiently hot to evaporate SiO. The SiO was 99.99% pure (metals basis) 3 to 6 mm diameter rocks from Alfa Æsar. The SiO was placed in one end of the boat. Between the SiO and the chimney of the boat were a series of baffles which prevent spitting and provide a uniform deposition rate. (Much of the background for this setup can be found in an article by Blevis [35].)

Heating the boat by the above method gave a deposition rate of 15 to 20 Å/s. Above the boat chimney was an additional 10 cm long chimney to prevent contamination of the other devices in the vacuum chamber. The same shutter protecting the samples during ion milling was also used to start and finish the SiO deposition. Each sample had a deposited SiO layer thickness of 200 to 350 nm to provide insulation from top contacts. During deposition, the sample was spun via the magnetic arm at a rate of 60-100 rpm, and the evaporation source was offset at a 15 degree angle with respect to the normal of the substrate to prevent the formation of pinholes (Figure 2.13).

Lift Off

Once the microfabracited features are planarized, the mask is removed by a procedure known as lift-off. Lift off or removal of the photoresist (Al for e-beam samples) was done in a class 100 cleanroom. The samples with photoresist for a mask were placed in an acetone bath, while samples with an Al mask were placed in a bath of KOH (Shippley 452 developer). Each sample with photoresist was individually cleaned with a acetone dipped Q-tip to remove the hardened photoresist. (It was sufficient to immerse samples with an Al mask in KOH for 5 minutes.) The sample

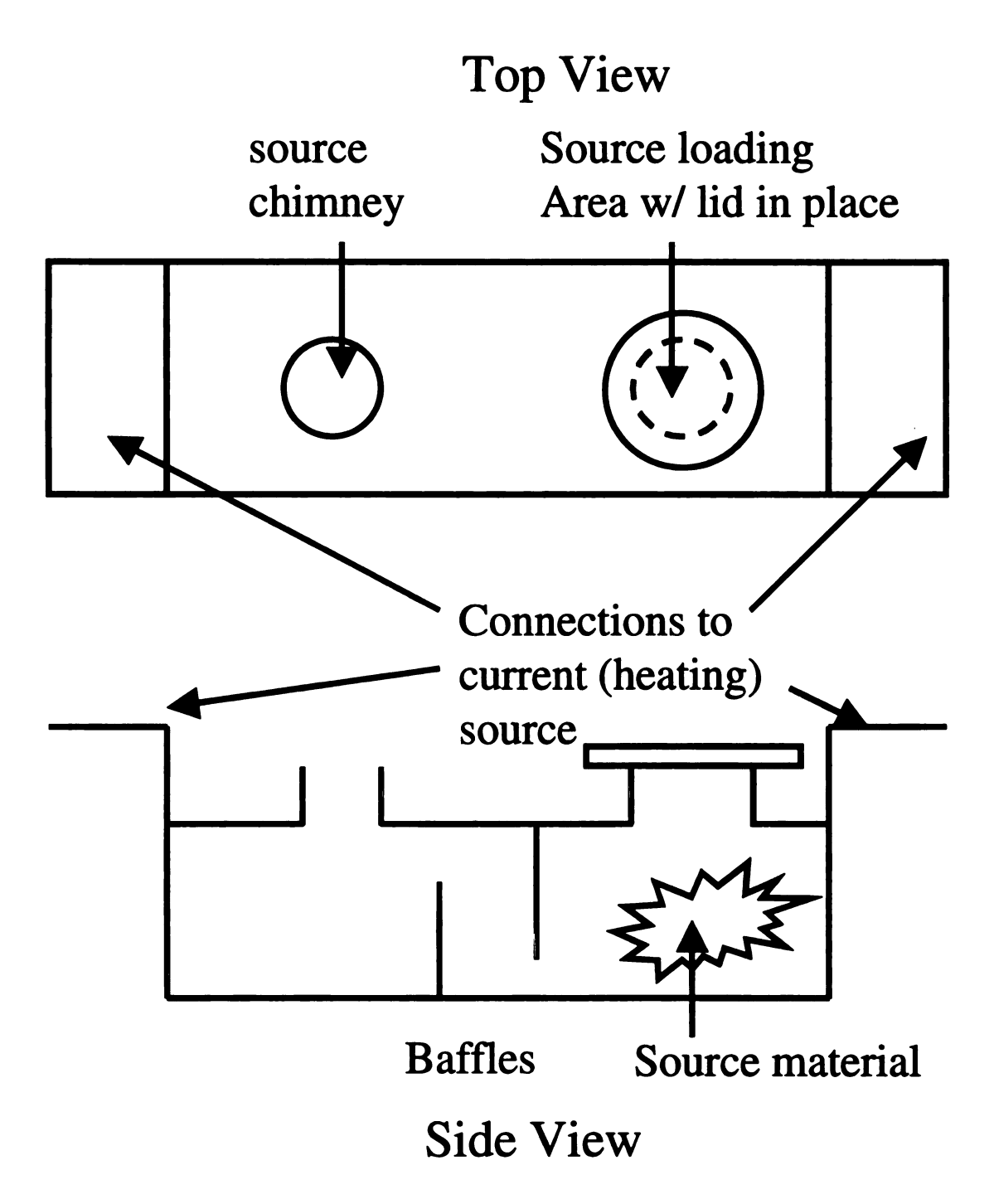


Figure 2.12: The tantalum boat for SiO evaporation. The SiO is placed in the loading area. The entire boat is heated using a current source. When the SiO begins to evaporate it must flow through a series of baffles that prevent spitting. The evaporated SiO then escapes vertically (side view) toward the sample.

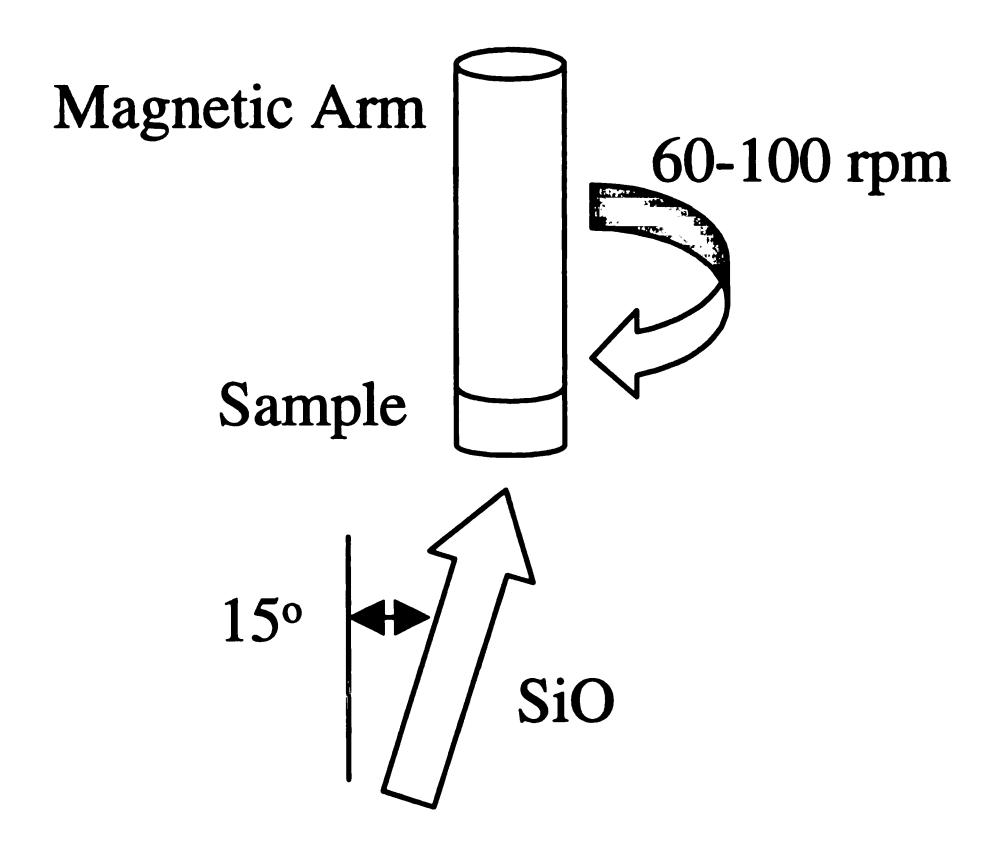


Figure 2.13: SiO_x deposition. The insulator is evaporated at a 15 degree angle with respect to the sample-surface normal. This and the rotation help to eliminate pinholes.

was then visually inspected using an optical microscope at 20-100X to ensure that the mask was removed. After confirmation that the bulk of the mask was removed, the samples were again immersed in 40°C acetone or room temperature KOH and agitated in an ultrasonic cleaner for 15 minutes. Samples with an Al mask were rinsed with water and immersed in acetone (40°C) for 15 minutes. All samples were then rinsed (with IPA) and immersed in 40°C IPA. Again, the samples were agitated using an ultrasonic cleaner. Finally, the samples were rinsed in deionized water and placed in 80°C deionized water, agitated for 10 minutes in the ultrasonic cleaner and allowed to cool to room temperature. After this, the samples were taken for a final sputtering deposition of Nb superconductor. Since the contact of the Nb to the multilayer was critical, the Nb deposition was done as soon as possible after lift-off to help prevent contamination processes which might increase the contact resistance.

2.5 Measurement Equipment

For a fully prepared sample, MR measurements were made by connecting three separate pillars to the measuring apparatus. Although both a nanovolt and SQUID null detection system were employed, the connections from the sample to both systems were identical. The contact (and thus area of current flow) to be measured (#1) was connected to both a voltage (V+) and current lead (I+). A second contact (#2) was connected to the other current (I-) lead. The third contact (#3) was connected to the final voltage lead (V-). This allows current to pass from contact 1 to contact 2 (via the bottom Nb superconductor) without creating a potential drop in contact 3 (Figure 2.14). Placing two leads on each contact allows one to permute the leads connected to the voltage and current measuring devices and thus measure each individual contact.

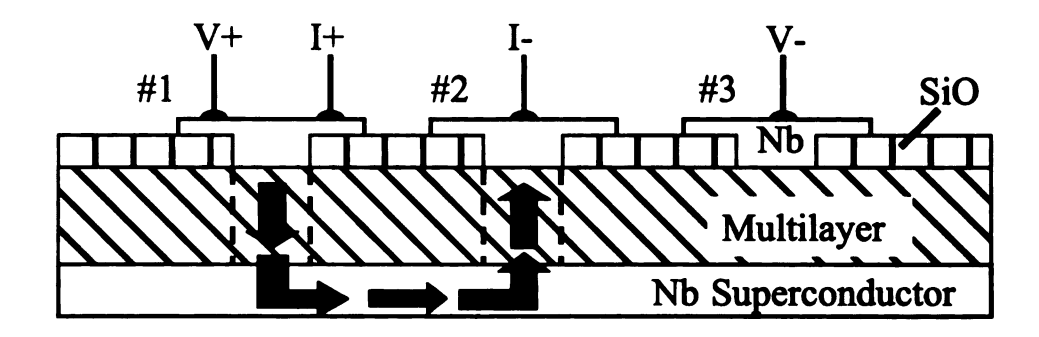


Figure 2.14: Measurement setup and geometry of the sample. Input current and voltage leads are attached to the contact to be measured (#1). Output-current and second-voltage leads are attached to #2 and #3 contacts, respectively. Current flows between contacts #1 and #2 (via solid arrows), and the voltage contact at #3 measures the potential of the bottom superconductor.

2.5.1 SQUID Based Null Circuit Voltage Measurements

Most field dependent resistance measurements were done on a low temperature probe containing a superconducting quantum interference device (SQUID) null circuit and a superconducting magnet. Samples were cooled to 4.2 K while connected to a SQUID feedback circuit. This potentiometer circuit allows measurements of resistance in the $n\Omega$ range (Figure 2.15). A known current, I_A is applied through the unknown resistor R_x . The SQUID, coupled to an inductor between points A and B provides a very sensitive feedback current I_{FB} which balances the circuit so that points A and B are at an equipotential. The feedback current through the reference resistor R_{Ref} (= 100 $\mu\Omega$) is then measured with a 10 k Ω feedback resistor (not pictured) in series with the reference resistor. The equipotential balance gives $R_x \times I_A = R_{Ref} \times I_{FB}$. R_x can then be calculated. Because of the sensitive nature of the measurement, all leads connecting R_x and R_{Ref} are superconducting.

The applied magnetic field in the probe can range over \pm 1.5 Tesla. This was

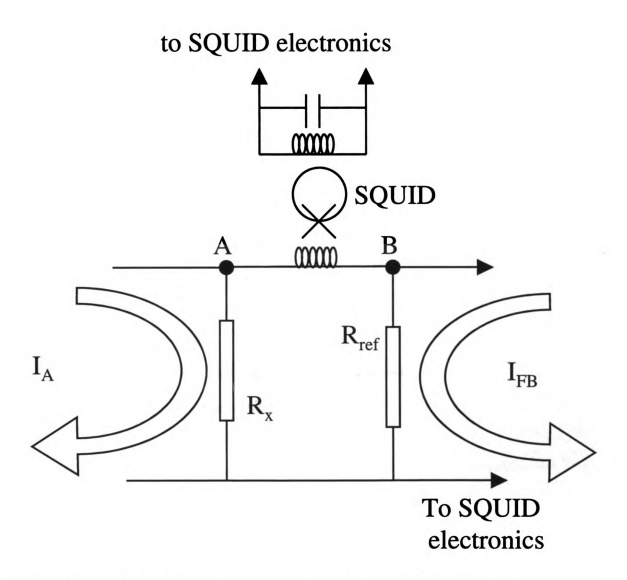


Figure 2.15: The SQUID null feedback circuit. An RF SQUID system (SQUID, inductor, RF LC circuit, and semiconductor electronics) balances the circuit so no current flows from point A to point B. The voltage drop across both resistors is equal in this balanced state. From Ohm's law, one can then solve for R_x and in terms of I_A , I_{FB} and R_{Ref} . I_A is applied to the system and is known. This applied current causes the SQUID system to go out of balance. The feedback current from the SQUID system, I_{FB} , is measured by a resistor in series with the reference resistor, R_{Ref} . R_{Ref} is a precision resistor with a known resistance.

accomplished by applying a known current through a superconducting coil operating in persistent mode (the sample sat inside the magnetic coil). The magnetic field was calculated by using the known coil constant (533.2 Gauss/A) of the magnet.

2.5.2 Nanovolt measurements

A new multiplexer system with 12 current channels and six voltage channels was built for four point MR measurements on samples with resistances > than 100 $\mu\Omega$ (Figures 2.16, 2.17, and 2.18). A Keithly 2400 current source supplied current while a Keithly 2182 nanovoltmeter measured voltage. The sample was measured in liquid He (4.2 K), and measurements were taken over a wider range of currents than was possible with the SQUID system. The multiplexer system was designed to allow different samples to be measured on a single substrate without removing the probe from the liquid He dewar.

The probe consisted of six current and voltage Cu leads (12 total) that were connected to the external measuring equipment at room temperature. Each connection included shorting and grounding (including direct to ground and ground through a 1 M Ω resistor) switches for each individual wire. These switches were installed for future applications where static charges could have enough energy to burn out narrow wires or features made by e-beam lithography. Each lead was then connected to the multiplexer system. The current leads were connected via a Fisher seven-pin connector, while three all-Cu Ω -Engineering thermocouple connectors were used to connect the voltage leads (2 leads per connector, plus a ground connection). This all-Cu wire and connection system minimizes voltage offsets and drifts due to the thermoelectric effects at room temperature.

The Keithly 7001 multiplexer with 7011 card was used to switch the current leads, while the voltage leads were connected to a Keithly 7168 low thermal offset card. Due to the layout of the 7168 card only eight channels with low thermal offsets

were available for voltage multiplexing which meant that half of the channels were hardwired as voltage high (or V+) connections and half hardwired as voltage low (V-). The current connections had 40 channels and each wire could be connected to the current high (I+) or low (I-) channel.

As shown in Figure 2.17, the measuring probe fits inside a separate sheath for low temperature measurements with a superconducting solenoid of coil constant 506.6 Gauss/A. For room temperature measurements the probe can be separated from the sheath and inserted into a standard electromagnet.

A LabView program was written to automate the measurement process. Using the already existing computer code from the SQUID system to control the persistent-mode magnet, seven measurements were made at each field setting by measuring DC voltage versus DC current, where the current was reversed each time to null-out thermoelectric offsets. In addition, each sample was given an overall current dependence check to ensure that the resistance was not current dependent

2.5.3 Area Measurements

The areas of contacts were measured using a JOEL 840 electron microscope. Samples were photographed at an appropriate magnification and areas measured using IP Lab software or a vernier caliper to measure dimensions and compare with the distance marker placed by the microscope. (No self-consistent measurements were possible.) These measurements were only good to 10% due to operational parameters of the microscope [36]. Accuracy of the microscope is dependent on keeping parameters such as the beam current, aperture size and magnification identical from image to image. For our purposes this was not feasible. Every effort was made to minimize these effects and obtain reproducible results.

Figure 2.16: The circuit layout of the nanovolt probe. A Keithly 2400 current source (1) is connected to a Keithly 7011 multiplexer card (2) with two electronically isolated banks of connections that allow each wire coming from the probe to be selected as either high or low in combination with any other wire. A Keithly 2182 nanovoltmeter (3) is connected to the voltage leads. However, the Keithly 7168 multiplexer card can only support one voltage connection per voltage lead. Thus half the voltage leads are hardwired as V+ and the others are V- (4a,4b) The wires are then connected to the probe (5,6; see Figure 2.18). Finally the leads are taken to the low temperature portion of the measurement in the measuring probe and connected to the sample.

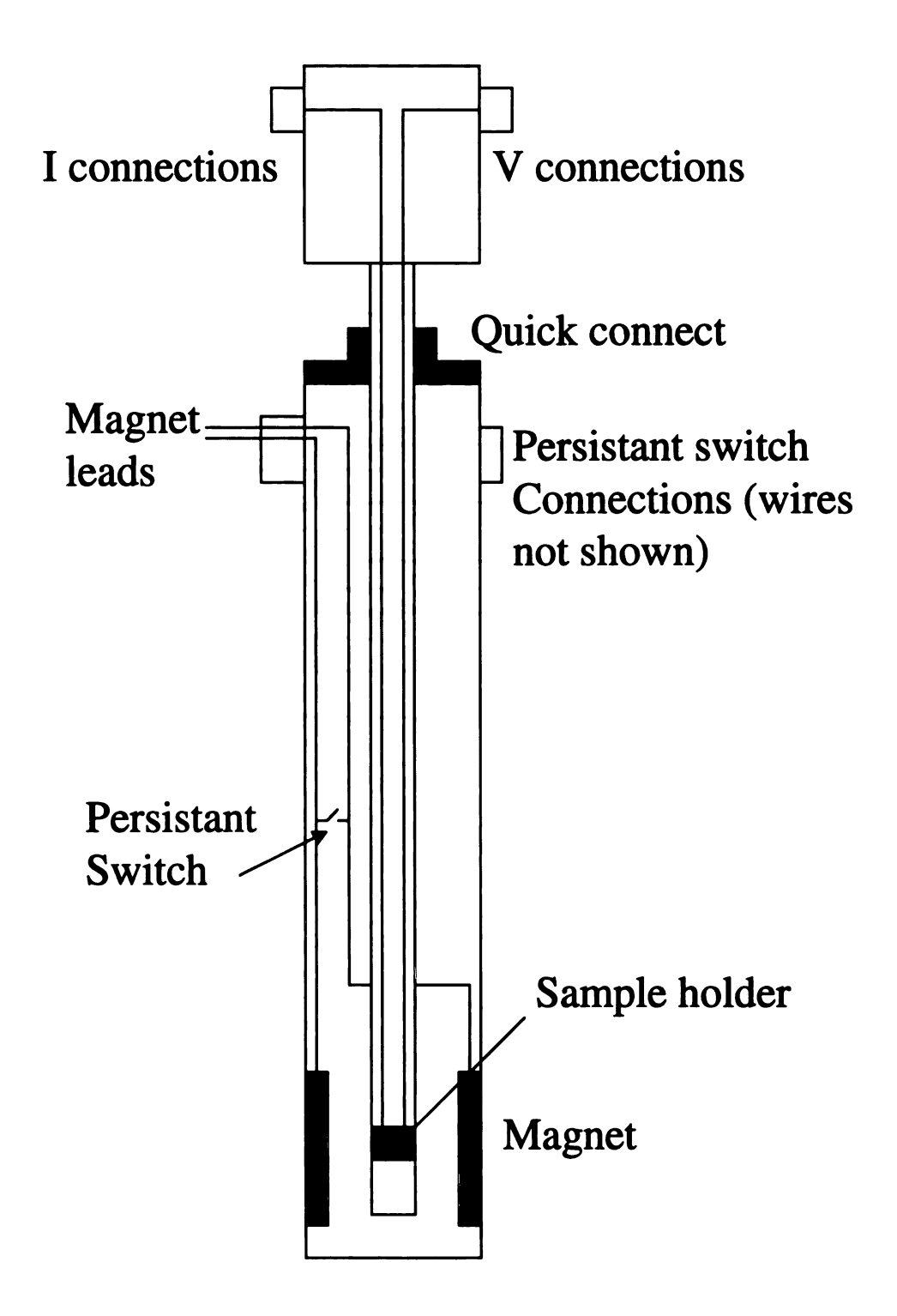


Figure 2.17: The modular measuring probe used for nanovolt measurements. The magnet, magnet leads, and persistent switch connections are self-contained in a sheath that connects to the I-V portion of the probe via a quick connect. This sheath surrounds the probe and the connection is placed at a pre-determined location to put the sample in the middle of the magnet. The measurement portion of the probe can be used with or without the magnet portion.

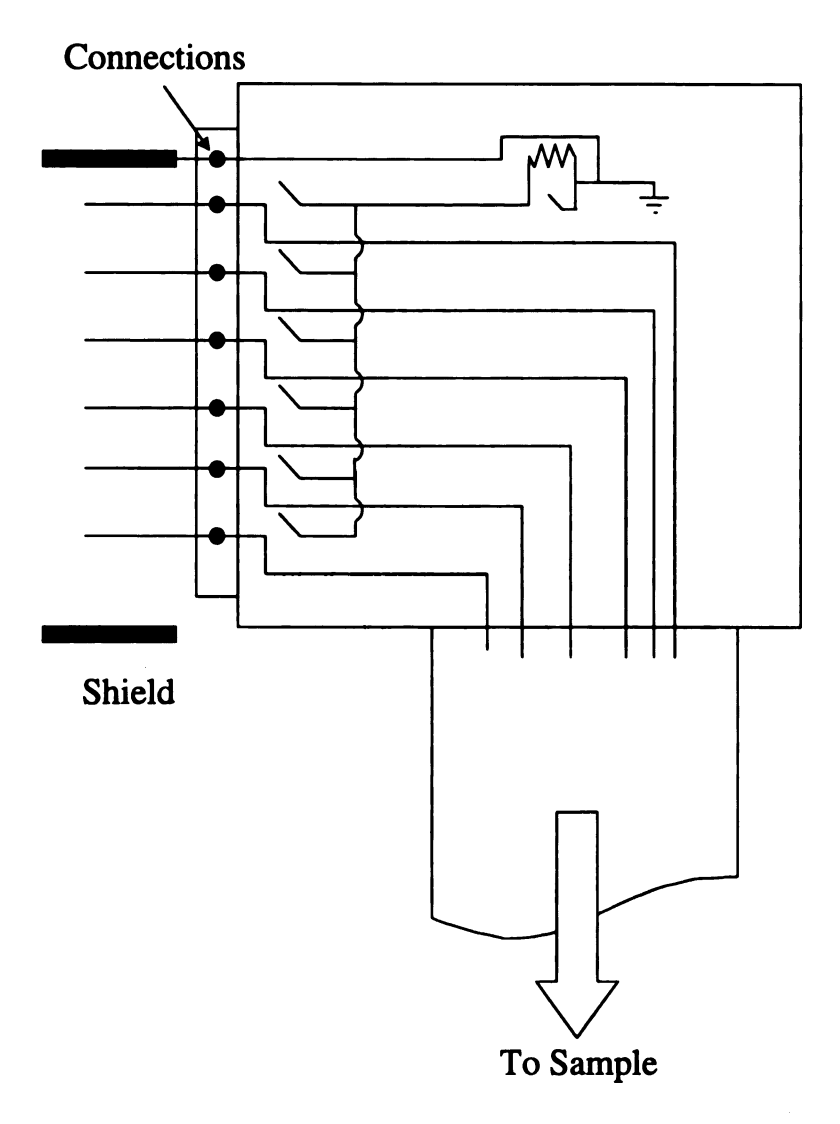


Figure 2.18: A layout of the external connections to the measuring probe (one side only, see items 5 & 6 in Figure 2.16). For both the current and voltage leads, each wire is connected to a grounding system individually. The grounding system is also wired to a switch which chooses between a direct ground or grounding through a 1 $M\Omega$ resistor to minimize currents induced by static charges. The shield for each cable is directly connected to ground. Outside the probe, all current leads are inside a single shielded cable and each pair of voltage leads has its own shielded cable

Chapter 3: CPP-Multilayers with Micron Size Top Contacts

3.1 Introduction

Since the initial work of Pratt et al. [14], CPP multilayers have been the source of intense study. As mentioned previously several different methods have been developed to cope with the inherently low resistance of the multilayer due to the very short current path. These typically fall into two major categories: samples which employ superconducting contacts; and those which employ lithography.

Recently Cyrille et al. [22] made initial attempts to join lithography and superconducting contacts in hopes of combining the advantages of both. However, the complex lithography involved gave a very poor yield of useful samples. Part of this difficulty was due to the geometry—many (100) lithographed areas were connected in series, and a single bad contact could render the entire chain useless.

A new geometry was developed here [37], that combines simple lithography with superconducting contacts. In addition to a simplified geometry, the size of the contacts can be reduced to the physical limits of the lithography equipment. This should increase the resistance of a single contact to a point were a nanovolt system may be employed to perform magnetoresistance measurements. The process employed to fabricate these samples (type-I & -II) was described in Chapter 2.

3.2 Initial Work and Tests

3.2.1 Lithography Test

In order to test the initial fabrication procedure, several trial multilayers were made of the form: Nb(250) / Cu(100) /Co₉₁Fe₉ (x) / Cap / Nb(250) , all units in nm, x = 10-60, Cap was type C_I (Au (15 nm)) or C_{II} (Au (10 nm) / Nb (20-50 nm) / Au (15 nm)). The thickness of the Co₉₁Fe₉ layers was varied in order to measure both the resistivity of the Co₉₁Fe₉ layer and Nb/Co₉₁Fe₉ interface resistance, since the initial assumption is that the interlayers of Au will be superconducting by the proximity effect.

The results of the test are shown in Figure 3.1 [37]. From the 2CSR model, one can model the resistance as twice the Nb/Co₉₁Fe₉ interface specific resistance plus the specific resistance of the Co₉₁Fe₉ single layer:

$$AR = 2AR_{Nb/CoFe} + AR_{CoFe} (3.1)$$

$$= 2AR_{Nb/CoFe} + \rho_{CoFe}t_{CoFe} \tag{3.2}$$

The resistivity of Co₉₁Fe₉ can be found by plotting the specific resistance versus the layer thickness where the resistivity is the slope of the line and the Nb/CoFe interface resistance is half the intercept of the y-axis.

The resistivity of $Co_{91}Fe_9$ in all cases agrees well with previously reported data [38]. Here the value is calculated from a linear regression for the two sets of samples with multiple values of $Co_{91}Fe_9$ layer thickness. For the type-I samples, the resistivity was $71 \pm 5 \text{ n}\Omega\text{m}$. Type-II samples gave a value of $61 \pm 8 \text{ n}\Omega\text{m}$. The previously reported value of $70 \pm 10 \text{ n}\Omega\text{m}$ was performed using Van der Pauw techniques.

The Nb/Co₉₁Fe₉ interface resistance is also in agreement with previously reported results. Type-I samples give $2AR_{Nb/CoFe} = 8.0 \pm 0.1 \text{ f}\Omega\text{m}^2$. The data for ultrasoni-

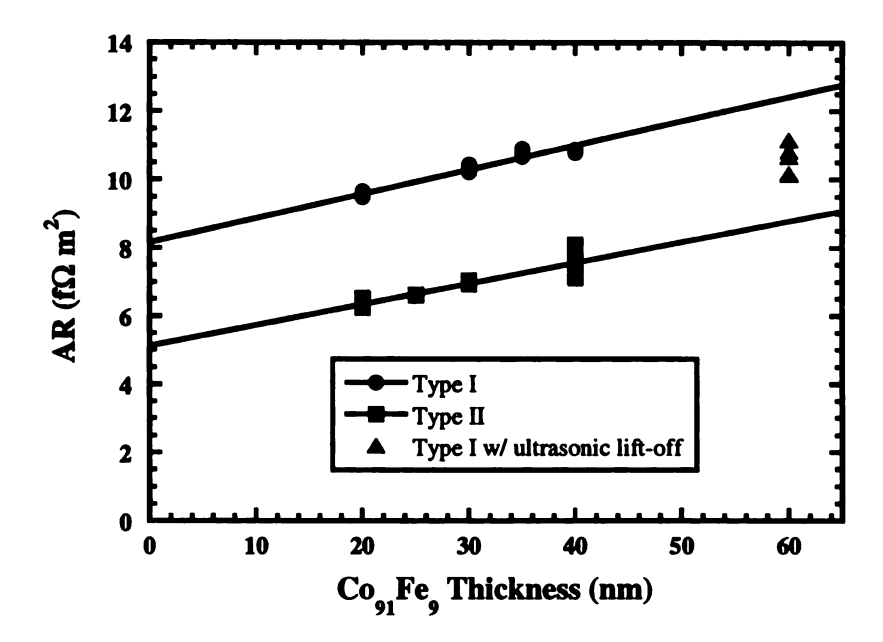


Figure 3.1: A plot of the specific resistance for single layer $Co_{91}Fe_{9}$ samples versus the $Co_{91}Fe_{9}$ layer thickness. The circles represent samples with a C_{I} cap that underwent a cleaning procedure without ultrasonic agitation. The triangles represent samples that did have ultrasonic agitation (C_{I} cap). The squares represent a C_{II} cap with the original (non-ultrasonic) cleaning.

cally agitated type-I samples extrapolate (using the slope for previous type-I samples) to $2AR_{Nb/CoFe} = 6.4 \pm .4 \text{ f}\Omega\text{m}^2$. Both type-I values are not significantly different than the previously published value of $7.0 \pm 1 \text{ f}\Omega\text{m}^2$ for the $2 \times \text{Nb/Co}_{91}\text{Fe}_{9}$ interfaces [38]. However, it appears that the ultrasonic agitation lowered the Nb/Co₉₁Fe₉ interface value, indicating that the final cleaning step is most likely very important to produce a clean-interface resistance [37].

It was concluded from earlier studies [29,30] that the middle Nb layer (in C_{II}) is superconducting at 4.2 K, and thus most of the CPP resistance will come from the metallic multilayer stack that was sputtered under UHV conditions. Since $2AR_{Nb/CoFe}$ = 5.1 ± 0.2 f Ω m² (solid squares in Figure 3.1) for such type-II structures, it appears that direct contact between CoFe and Au (10 nm) (in place of 10-nm-thick Cu in 1 × 1 mm samples) lowers the effective Nb/CoFe interface resistance [37].

In addition, as previously mentioned, the ability to perform self-consistent mea-

surements in the electron microscope was limited, and thus the accuracy of our measurements is at best 10 % (verified by the manufacturer) [36]. However, because most of the measurements were taken with similar setups: constant aperture size; constant working distance (focal length); similar magnification; and similar current, the precision of the measurements is probably much better than 10%.

3.2.2 Current Dependence

For superconducting contacts, the CPP current density J_{CPP} will likely be limited to a maximum of $\sim 5 \times 10^6$ A/cm² (observed in our laboratory for sputtered Nb films [39]). Below this range it is expected that there will be no current dependence in the resistance of the sample. In order to confirm this, the resistance of the sample was measured using our nanovoltmeter-based 4 point V-I technique. Only the smallest samples have resistances large enough to be measured with this method. Because of the limited nature of the SQUID feedback system, a large range of currents was not available in that setup, especially at the high current densities.

The highest the current density will most likely occur is in the vias of the samples—between the top Nb contact and the multilayer. (Figure 3.2). Because of the ~100-nm penetration depth of our Nb [39], current will only flow along the perimeter of the vias. Thus the cross sectional area for current flow is roughly given by the product of the penetration depth and the perimeter of the contact (feature size \times 0.4 μ m²).

The measurements for several Co₉₁Fe₉ EBSV samples are shown in Figure 3.3. A secondary judge of the lithography is how close to the critical J_{CPP} of Nb can a contact sustain a superconducting current. The 9.5 μ m² and 28 μ m² samples exhibit a significantly lower critical J_{CPP} of 10^5 A/cm², but these samples were fabricated in the earlier stages of the lithographic processing. In contrast, the 4.5 μ m² data do approach the expected critical J_{CPP} of the Nb without significant increases in resistance. This shows that the lithography again is not significantly affecting our

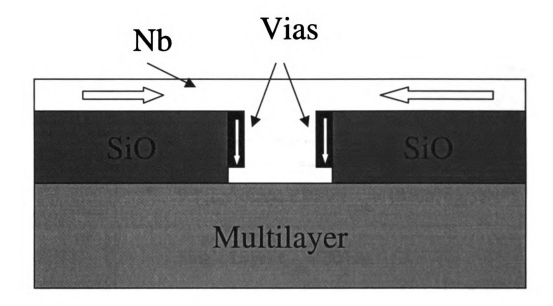


Figure 3.2: An explanation of vias (black areas with white arrows). The portion of the Nb (white, black for vias) where the current (block arrows) flows from the Nb that lies on the SiO (grey) to the portion of Nb in contact with the multilayer. The current only flows along the edges because the penetration depth of the superconducting Nb is ~100 nm.

ability to perform CPP transport studies with a nanovoltmeter.

Ideally, one would like to take advantage of the ultra-sensitive SQUID based measuring system mentioned in Chapter 2 (Figure 2.15) for these small-contact samples. However, the electronics of the SQUID setup limit the feedback current to ~ 1 mA. The current through a 1 m Ω sample (a typical resistance for the smallest contacts) will then be 0.1 m $\Omega \times$ 1ma / 1 m $\Omega = 100~\mu A$. If one increases the reference resistor to 1 m Ω , the sample current will then be increased to 1 m $\Omega \times$ 1mA / 1 m $\Omega = 1$ mA. For a 1 μm^2 contact this gives $J_{CPP} = 10^5$ A/cm², an acceptable current density even for the worst of the samples shown in Figure 3.3. Since the voltage across the sample is now 10 times larger than before, the precision of the measurement is significantly increased.

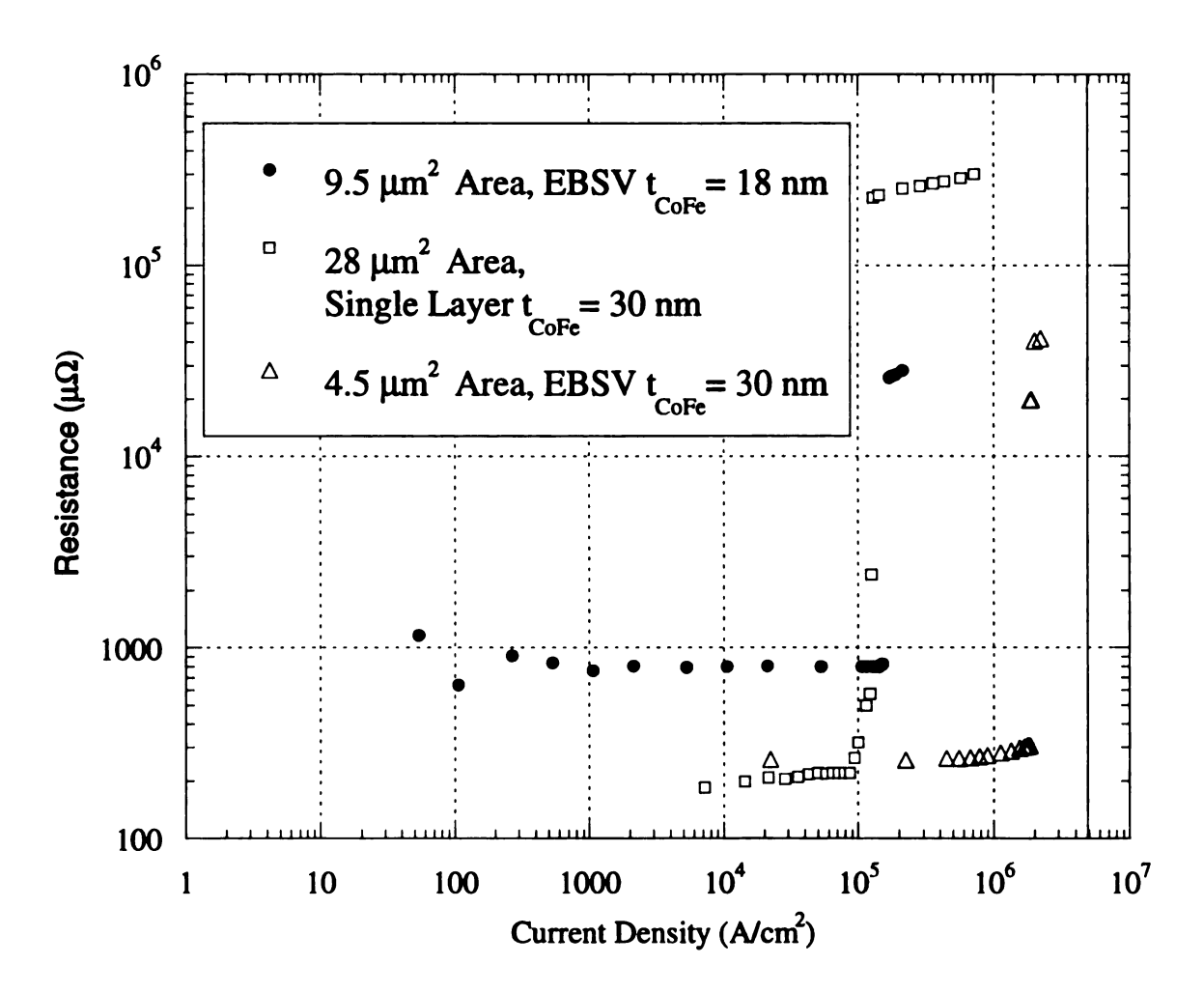


Figure 3.3: The current dependence of several of the smallest contact areas for $\text{Co}_{91}\text{Fe}_{9}$ samples. The right hand vertical line represents the expected Nb limit of 5×10^6 A/cm² [39]. As the lithography improved over time so did the amount of current that the superconducting contact could support. The sample with $28~\mu\text{m}^2$ was one of the earliest samples while the $4.5~\mu\text{m}^2$ was one of the last fabricated samples. Also note the high contact resistance of the $9.5~\mu\text{m}^2$ sample and how it will not support a high current density.

3.3 GMR Transport

Using the information gathered from these first experiments, exchange bias spin valves (EBSVs) of permalloy and $Co_{91}Fe_{9}$ were fabricated: Nb(250) / Cu(10) / $Fe_{50}Mn_{50}$ (8) / X(t) / Cu(20) / X(t) / Cap; with X = $Co_{91}Fe_{9}$ (= 'CoFe') or Ni₈₄Fe₁₆ (= Permalloy or 'Py'). The majority of these are type-II samples with a 20 nm thick Nb layer in the cap. This change was made to allow ion milling of a thin Nb layer as opposed to reactive ion etching of a thick Nb layer. Initially, RIE was a difficult process to control and gave inconsistent results due to a leak in the vacuum system, and the reactivity between the gas used, SF₆, and Si which caused redepositing of Si on the multilayer. Switching to sapphire substrates eliminated the second problem, but ion milling gave a yield rate of nearly 100% while RIE gave only 60-75%.

One of the most important predictions of the 2CSR model is that $A\Delta R$ should be unaffected by area of current flow. The results of the $Co_{91}Fe_{9}$ and permalloy EBSVs [37] are shown in Figures 3.4 and 3.5. The variance of $A\Delta R$ with area is similar to that of sputtered samples with current flow areas of 1 mm² (data points along the far right hand side of the graph). The variances in the 30 nm data in Figure 3.4 correspond to pillars on different substrates. Each single substrate has pillars that exhibit only small changes in $A\Delta R$ as A decreases.

Notice the Py data appear to have smaller variations in $A\Delta R$ (especially the 3 nm data). This is due to the implementation of refined lithography process and a new mask (described in the Chapter 2). The introduction of the higher resolution photomask greatly stabilized contact area and gave much better lift-off results. This resulted in much better estimations of the area since irregular breaks or rounding of the edges were much less common.

Most of the variations in $A\Delta R$ can be attributed to 2 sources. First, as can be seen from the 1 x 1 mm data included at the far right of each figure, $A\Delta R$ sometimes varies from sample to sample by more than the 5% uncertainty of the areas. Such variations

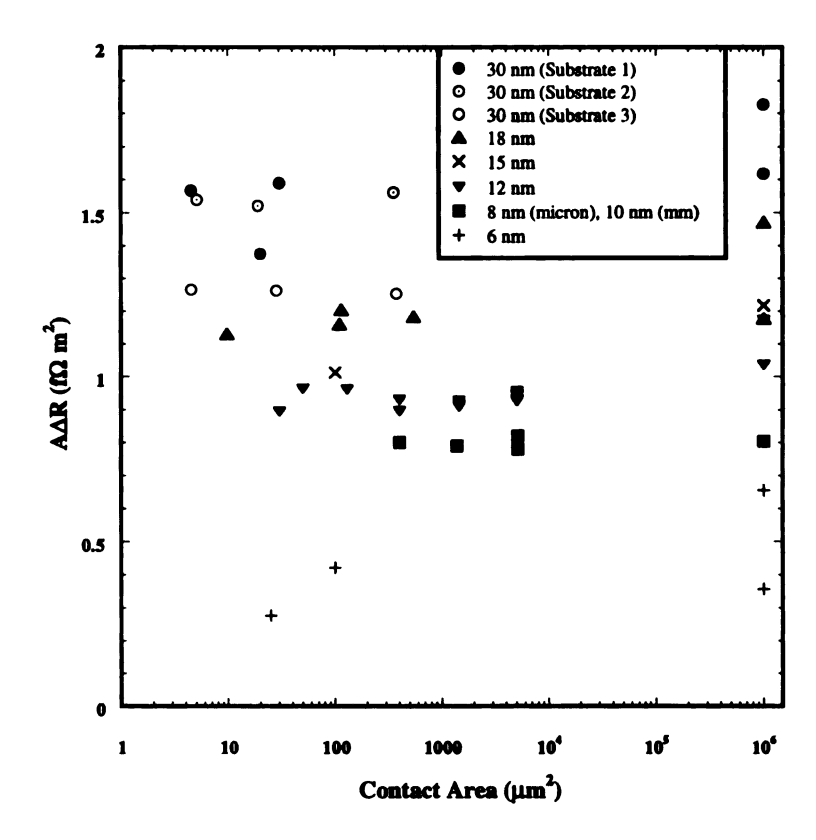


Figure 3.4: $A\Delta R$ vs Area for several thickness of $Co_{91}Fe_{9}$. The variations in $A\Delta R$ are similar to those seen in previously published data for samples with areas of current flow of 1 mm² (far right). Note that while the 30 nm data has large variations, individual substrates showed more consistent data, except for substrate 1 which had a poorly defined contact area for one of the contacts (poor-lift-off)

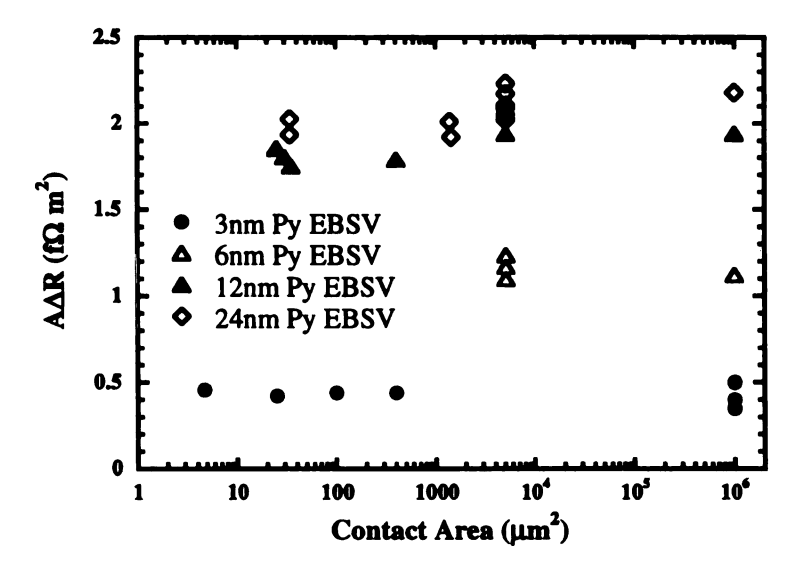


Figure 3.5: $A\Delta R$ vs Area for several thickness of Py. The variations in $A\Delta R$ are similar to those seen in previously published data for samples with areas of current flow of 1 mm² (far right hand side).

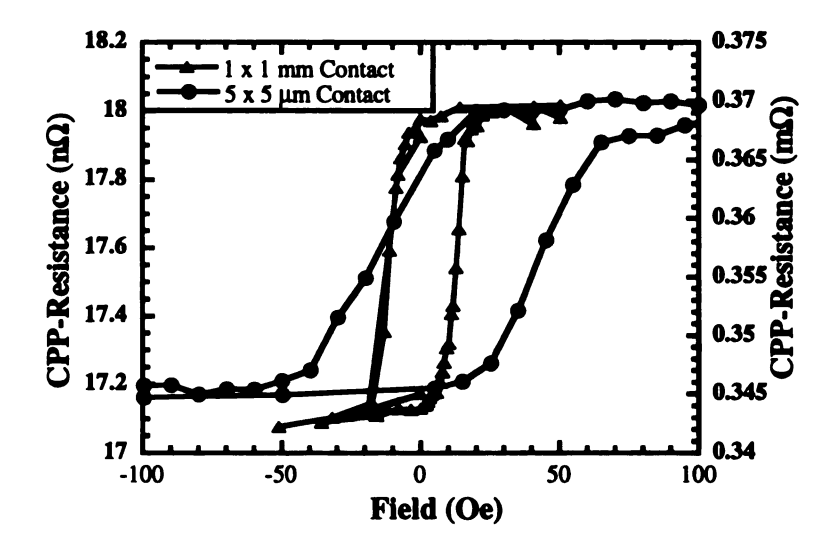


Figure 3.6: Minor hysteresis loops of CPP resistance versus magnetic field for one of the smallest contact-area Py samples compared with a 1×1 mm sample ($t_{Py} = 6$ nm for both samples). The saturation and coercive fields have been affected by processing.

are probably due to subtle changes in the sputtering conditions during deposition. Second, irregular holes or improper lift-off makes the contact area difficult to measure for the lithographed samples. When the lift-off of the resist is clean, the area is very easy to measure as it is a square with well-defined borders.

During the study of Area versus $A\Delta R$, it was discovered that while $A\Delta R$ was reasonably constant the magnetic properties were affected by the fabrication process [37]. Ion milling increased the saturation and coercive fields of Py EBSVs when t_{Py} was less than 12 nm. (Figure 3.6). The change was not as significant in samples that were: (1) reactive ion etched; (2) $Co_{91}Fe_9$ samples; and (3) Py samples with Py layer thickness greater than 12 nm. Better heat sinking of the sample during ion milling also reduced this change. An extra piece of silicon substrate was placed in the sample holders (Chapter 2) to be sure the sample was thermally anchored to the copper heat sink.

A final test of the transport properties was to demonstrate that the spin diffusion length remained unchanged in the new samples [37]. Previous work on Ni₈₄Fe₁₆and

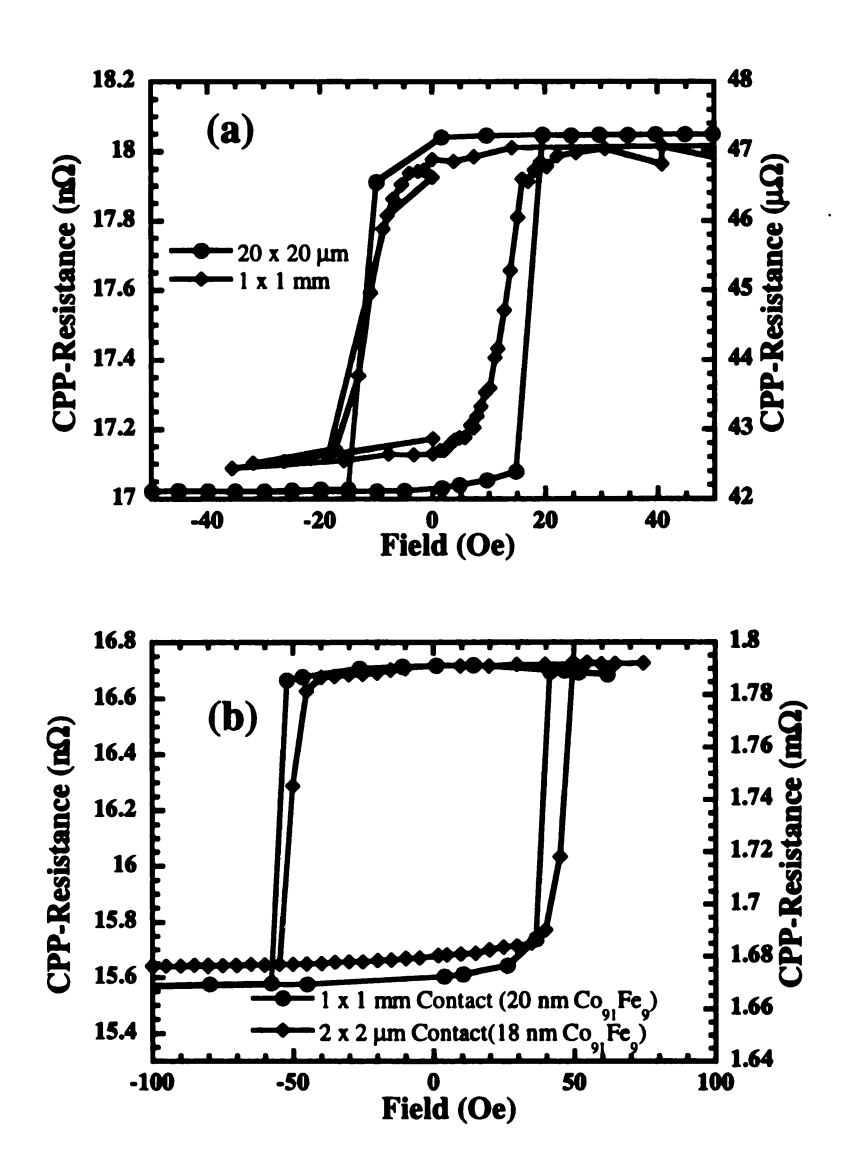


Figure 3.7: Minor hysteresis loops of CPP resistance versus field for (a) $t_{Py}=15$ nm and (b) $t_{CoFe}=18$ nm samples. Here the magnetic properties are very similar to those at 1 mm² samples.

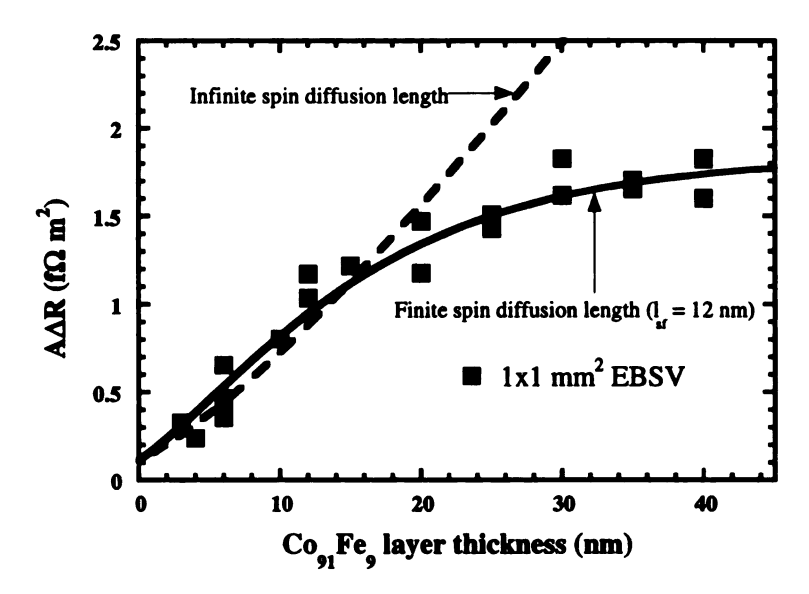


Figure 3.8: The effect of the spin diffusion length l_{sf} on $A\Delta R$. The experimental results show that l_{sf} is indeed finite.

 $Co_{91}Fe_9$ [38,40] showed a finite diffusion length in both materials. This was shown by comparing $A\Delta R$ and the layer thickness. If the spin diffusion length is infinite, $A\Delta R$ will continually increase with increasing layer thickness. If l_{sf} is finite, then after a certain layer thickness, $A\Delta R$ will no longer increase. This effect is shown in Figure 3.8 for 1×1 mm samples [38].

The results from the lithographed spin valves [37] and those from previous work [38, 41](1 \times 1 mm samples) show good agreement. (Figures 3.9 and 3.10). The finite spin diffusion length for both ferromagnetic alloys is demonstrated again by the micron size data where the areas range from \sim 5100 to 4 μ m². In addition the variation of A Δ R for fixed thickness is the same as or better than that for the 1 \times 1 mm EBSVs. This improvement is likely due to the fact that multiple-size contacts are available on the same multilayer (fabricated under identical conditions), while each 1 mm² data point represents a separate multilayer deposition. These figures clearly demonstrate that CPP-GMR transport is unaffected by the lithographic processing.

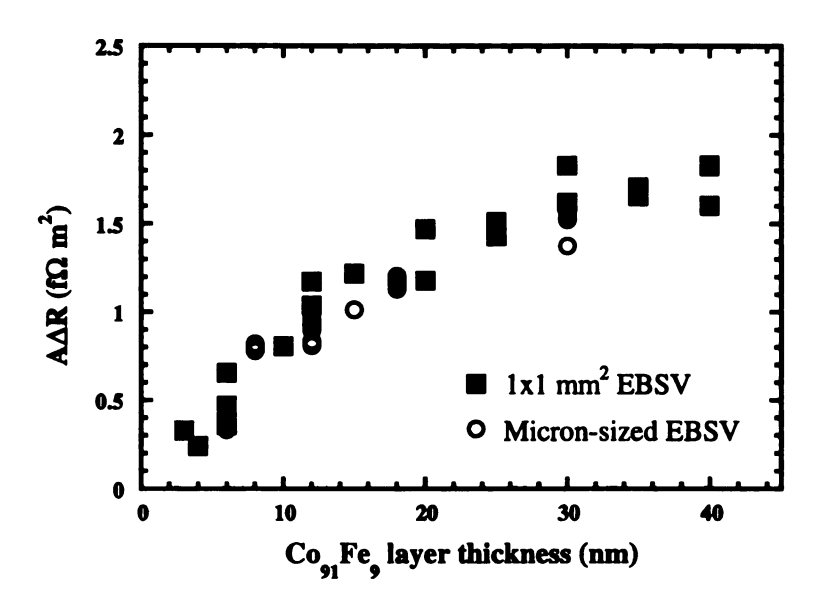


Figure 3.9: $A\Delta R$ versus t_{CoFe} for 1×1 mm (solid squares) and micron-size (open circles) CoFe EBSVs.

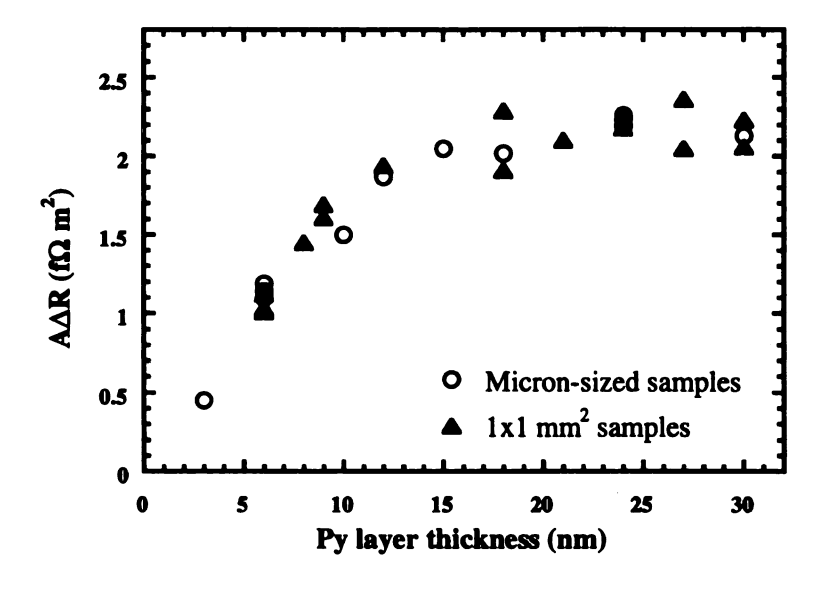


Figure 3.10: $A\Delta R$ versus t_{Py} for Py EBSVs with 1 × 1 mm (solid triangles) and micron-size (open circles) areas.

Chapter 4: CPP-Domain Wall Trapping

One et al. showed [9], using a trilayer of Ni₈₀Fe₂₀ (5)/Cu(10)/Ni₈₀Fe₂₀ (20) and a CIP geometry, that domain wall trapping was possible in the narrow neck of a wire of sub micron width. Based on MR measurements as the field was swept from negative to positive, an intermediate "state" between the P and AP state was achieved where a domain wall was trapped in a narrow neck of the long wire. Further work showed that a source of domain walls was needed to provide a reliable method of injecting a domain wall into the narrow wire [42]. Using a diamond shape F-pad [43] at the end of a long wire helped to facilitate this injection and the eventual trapping of a wall at the neck region.

By transferring this experiment into the CPP geometry, it may be possible to study specific regions of the wire by using localized superconducting contacts. The contacts in the CPP geometry can be made to lie only in the region of interest. This allows a localized current to probe the area of trapping, and the resistance changes from such a measurement as a domain wall sweeps past the contact would allow one to study the relative position of the wall based on the size of the GMR in the AP and P states.

The initial geometry of the sample was a long wire with flat ends (Figure 4.1). Continuing studies on domain wall formation show that flat ends of the wire are more likely to produce domain wall nucleation. As mentioned before, a study by the Shinjo group showed that placing a domain wall 'source' [42] at the end of the wire further improves the likelihood of domain wall propagation. Otherwise it is uncertain where the wall nucleates in the sample. Additional study showed that a diamond-shaped pad on one end of the wire is most successful at injecting a domain wall into the

sample [43]. This work was not published at the time of the initial photolithography study but was incorporated into e-beam lithography samples fabricated later.

4.1 Initial Trials

A series of Ni₈₄Fe₁₆exchange bias spin valves was fabricated as type-III samples. Applying the previous photolithography work of superconducting contacts, the EBSV was shaped into a wire geometry using the previously described methods for the high resolution mask. This time, as mentioned in the fabrication section, all of the EBSV layers were ion milled (excepting the portions under the photolithography mask). After planarization with SiO, the entire wire was covered with a superconducting contact. When measured, these Ni₈₄Fe₁₆EBSVs did not show conclusive evidence of domain wall trapping (Figure 4.2). Only the larger of the two photolithography geometries were successfully fabricated at this time. The smaller samples were poorly defined due to the buildup of photoresist along the edges of the sample which limits the resolution of the mask aligner. These small samples had ends that resembled Figure 4.1a; poor choices to study for domain wall trapping.

Previously measured $Co_{91}Fe_9$ EBSVs, for the study of superconducting contacts on macroscopic multilayers (Chapter 3), did show some evidence for domain motion at small contact sizes. Very small, and unrepeatable states were visible at the smaller contact sizes (Figure 4.3). Since this is comparable to the size of the wire geometry, the decision was made to use $Co_{91}Fe_9$ in the EBSVs for photolithography samples with both pattern sizes.

Using Co₉₁Fe₉ in the experiment was more successful. An initial experiment with the Co₉₁Fe₉ EBSVs showed some evidence of domain wall trapping. Although not entirely reproducible, the experiment left a hint of the direction to go (Figure 4.4). Clearly the domain wall was becoming trapped, not only in the notch but in other

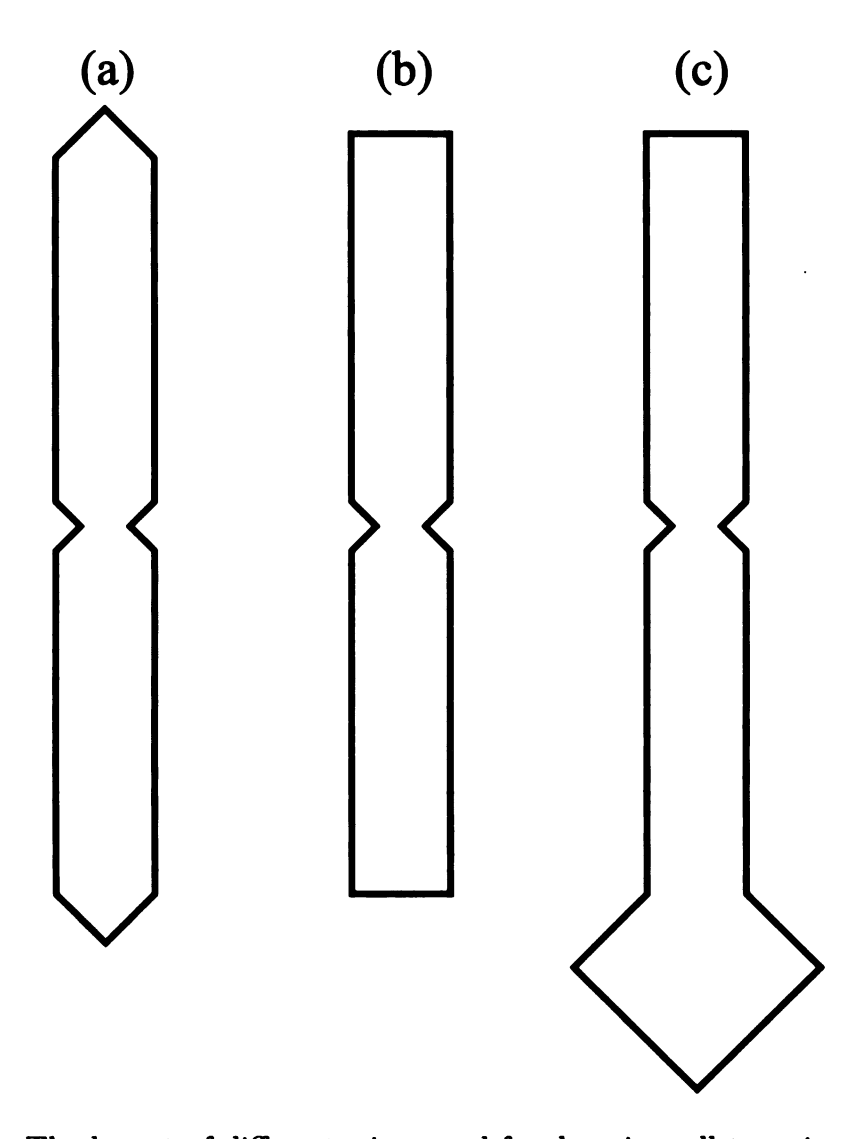


Figure 4.1: The layout of different wires used for domain wall trapping. (a) A poor candidate for domain wall trapping as the ends will not easily produce domain wall nucleation. Many of the initial 2- μ m-wide samples were shaped like this due to poor contact in the mask aligner. (b) The flat ends will be better for domain wall nucleation. This was the goal of the photolithography trials. (c) The best option is to provide a source of domain walls. The diamond on the end will be multidomain and nearly always inject a domain wall into the sample. This configuration was used for e-beam samples.

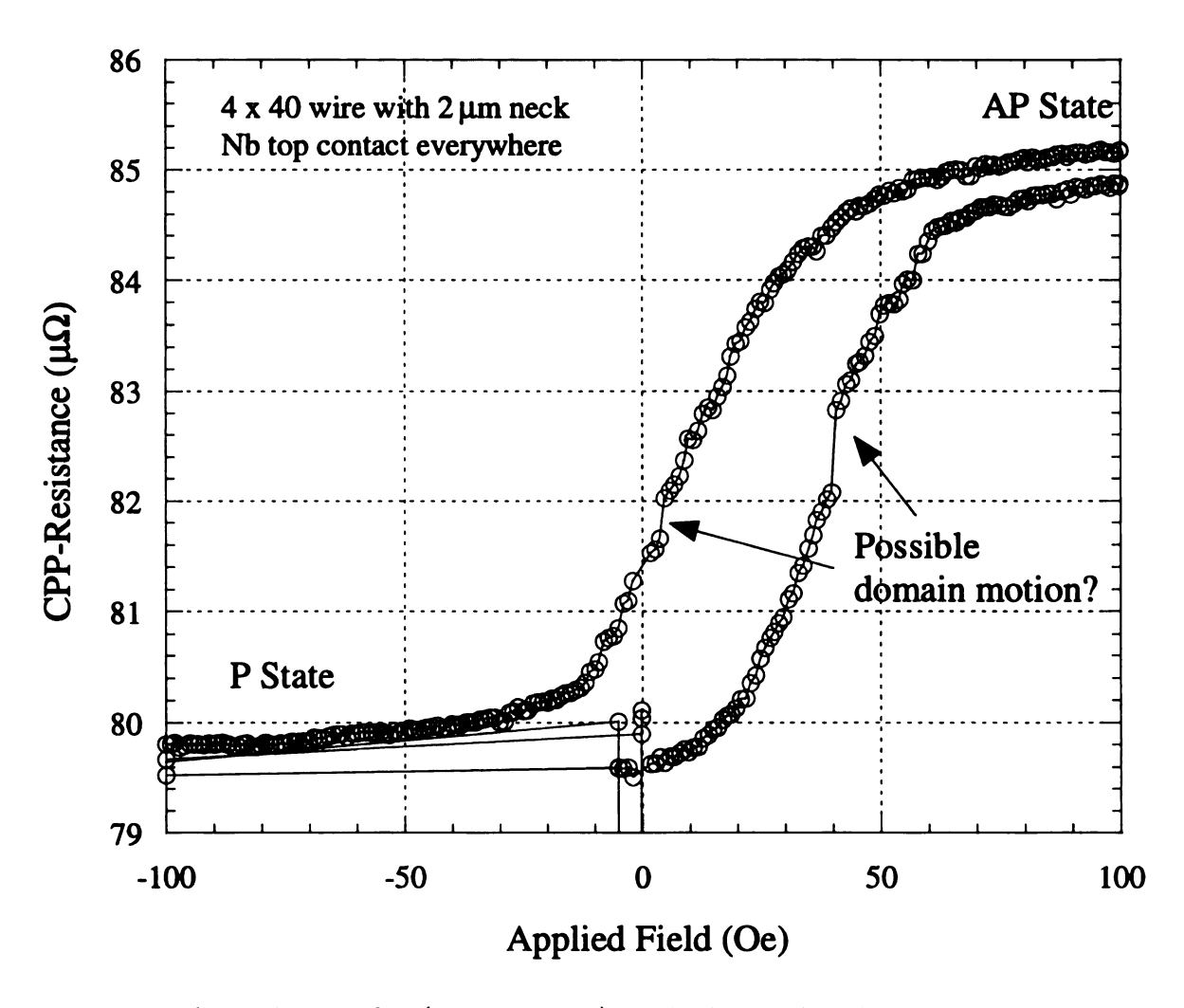


Figure 4.2: A Ni₈₄Fe₁₆EBSV ($t_{Py}=60$ nm) in the large photolithography geometry. There is poor evidence of domain wall trapping

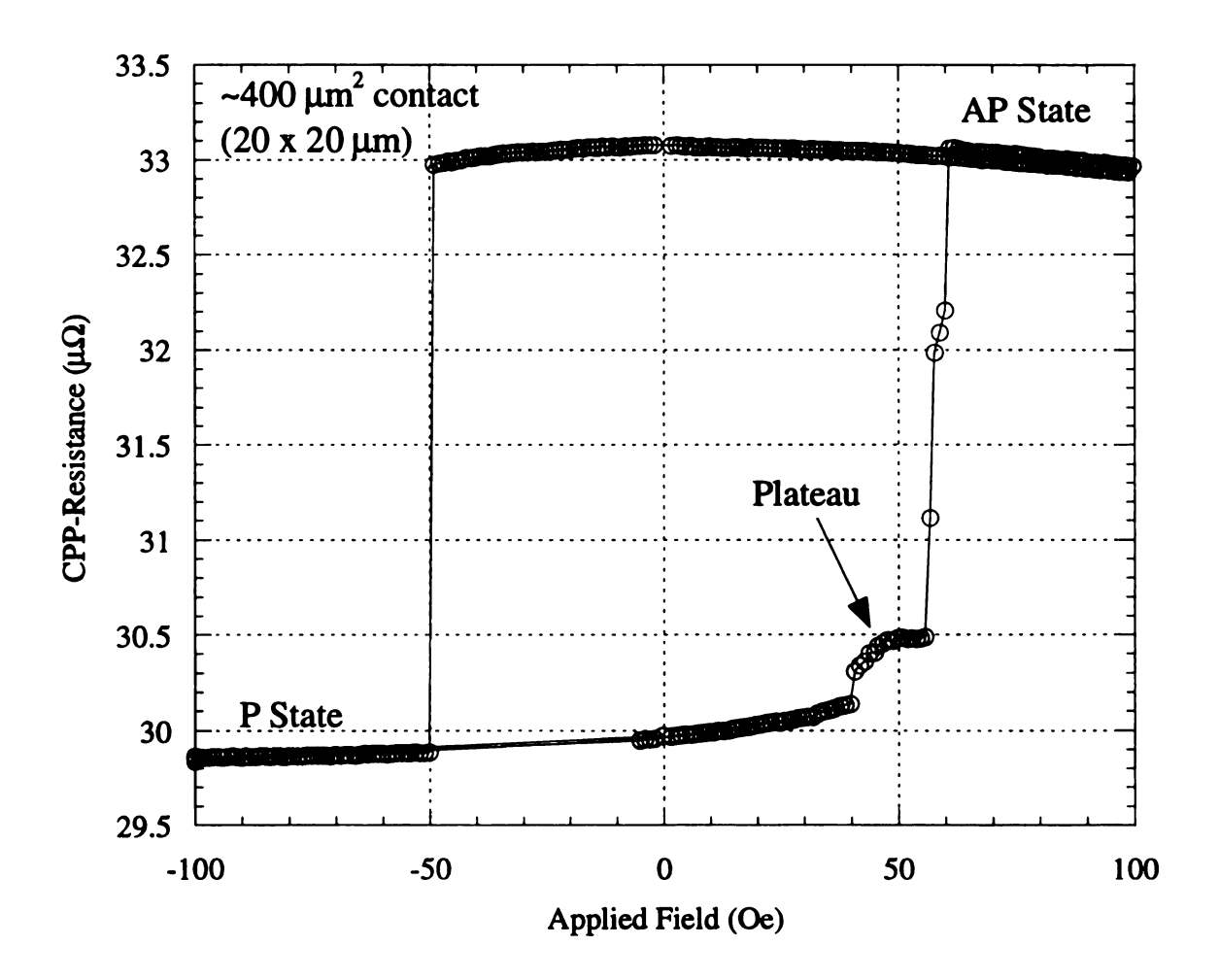


Figure 4.3: A $Co_{91}Fe_9$ EBSV ($t_{CoFe} = 30$ nm) from earlier transport studies (Chapter 3) that gives indications of domain wall trapping behavior. Note the plateau (in the transitions) between the P and AP states.

places along the wire as well. This happened because the photolithography process left the wire with edges that were not sharp, and the wire was populated with many small "necks." This occurrence of multiple intermediate states was evidence that either the photolithography had to be refined further, or a transfer to an electron-beam process was needed.

4.2 Improved Lithography

An attempt to improve lithography was made by reducing the buildup of photoresist along the edges of the square substrate. Using acetone and a Q-tip to remove the excess buildup along the edge reduces the contact distance and ensures that the resist is of uniform thickness over the entire sample (Figure 4.5).

This process improved the overall resolution by a roughly a factor of 2. The smallest photoresist patterns (2 microns wide with a 1 micron neck) were now better defined and produced better results (Figure 4.6). Still the results were not as clean as the original CIP work by One *et al.* Several non-reproducible intermediate steps were still observed in-between the P and AP states.

Type-IV samples combine all of the above mentioned techniques with the addition of a second lithography process that independently defines the top contact area. The first lithography procedure now shapes the multilayer feature into the wire geometry. All of the previously described methods are used (unchanged) to produce the shaped wire. Instead of a final step of sputtering top Nb contact, the sample is again processed using the same procedures; this time, however, a square photolithographic mask is used. The square features are placed directly over the notch area. A type-I procedure is employed to shape a 'window' in the notch area, while the rest of the wire is insulated from electrical contact. Now, only the area in the window is in contact with the final sputtered Nb layer. This arrangement uses the current flow properties of

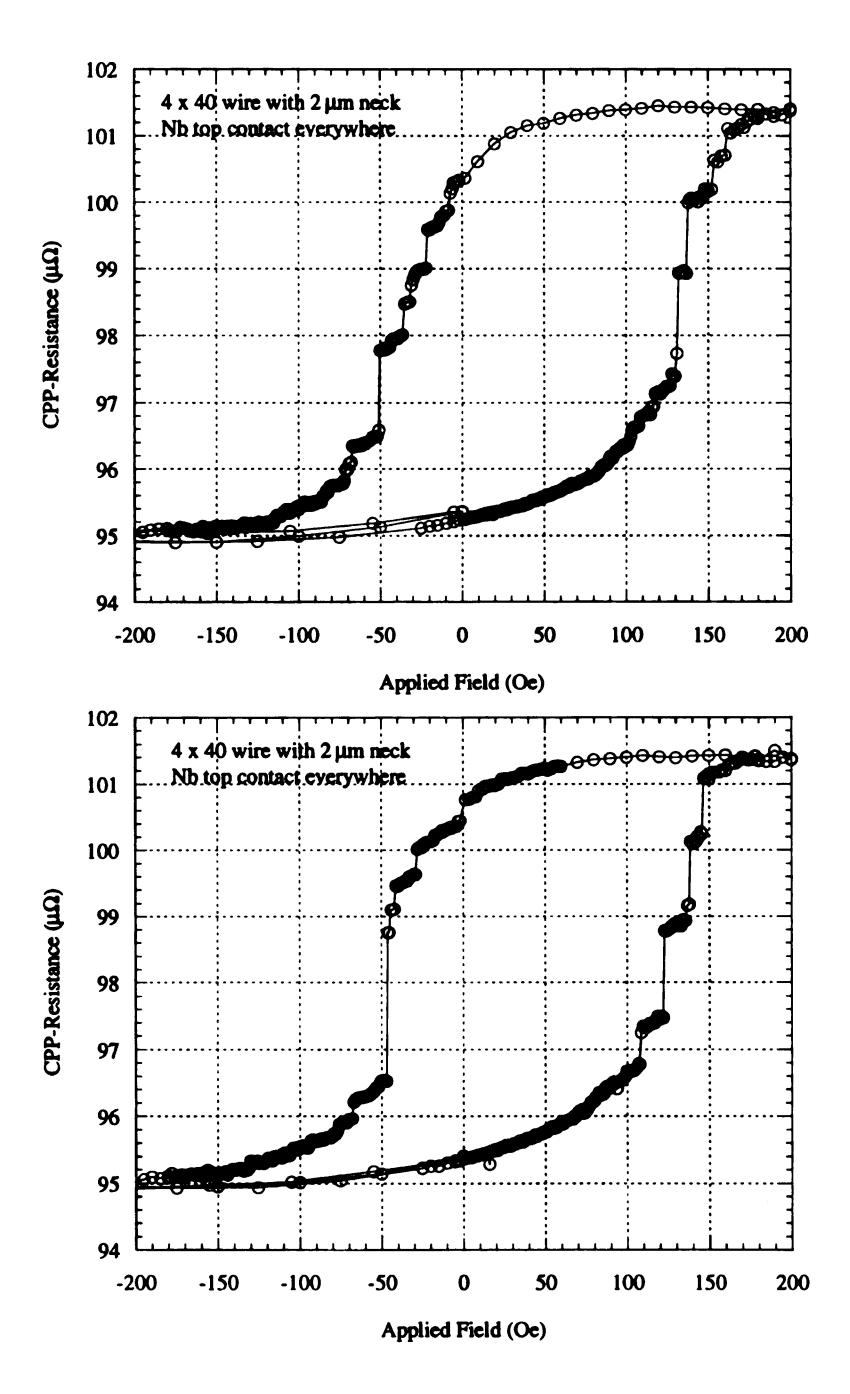


Figure 4.4: The best domain wall trapping sample with the initial lithography. Although decent results were obtained, they were not reproducible, as evidenced by these two runs on the same structure. This is a $Co_{91}Fe_9$ EBSV with $t_{CoFe}=18$ nm.

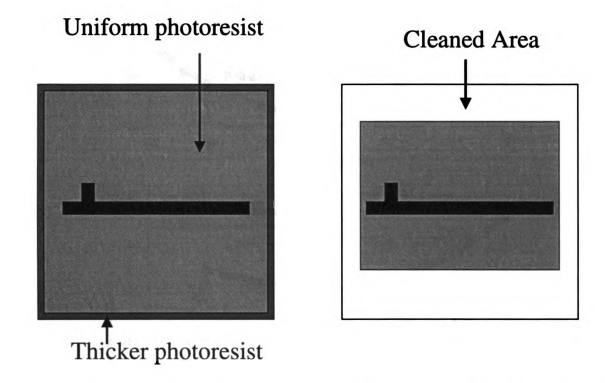


Figure 4.5: Removing the buildup of photoresist with acetone and a q-tip greatly increased the resolution of the photolithography. Before this improvement, the photoresist along the edges was much thicker and hindered good contact with the mask.

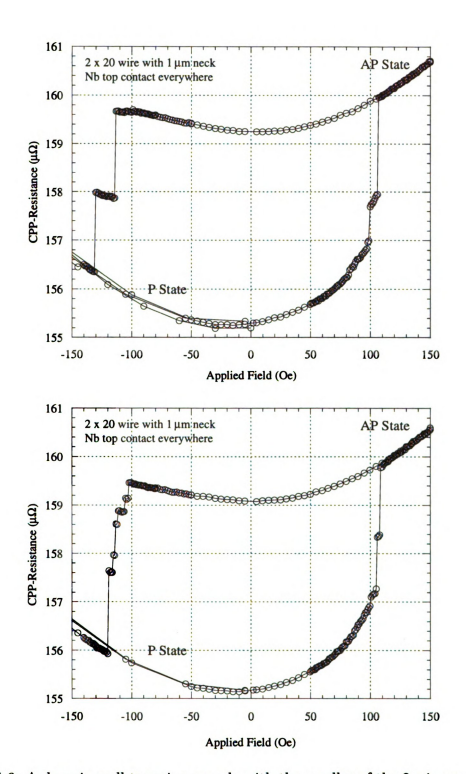


Figure 4.6: A domain wall trapping sample with the smaller of the 2 wire geometries. Although decent results were measured they were not reproducible, as evidenced by these two runs on the same structure. This data is from a $Co_{91}Fe_9$ EBSV with $t_{CoFe}=6$ nm.

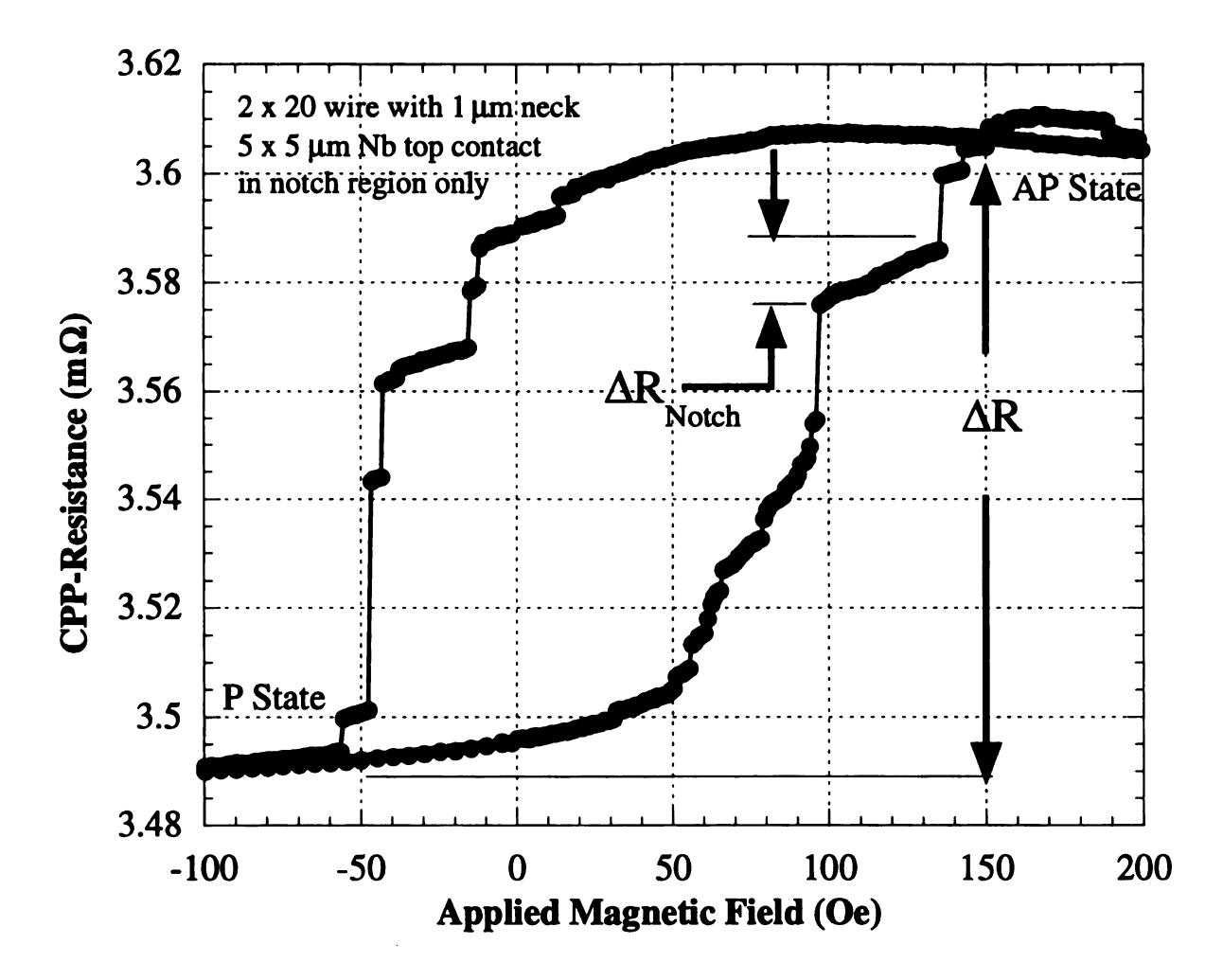


Figure 4.7: A 5 μ m contact on the small wire configuration for a Co₉₁Fe₉ EBSV (t_{CoFe} = 12 nm). The large plateaus in between the P and AP states are likely the domain wall trapping. ΔR_{Notch} is roughly the same for both intermediate states. Based on the total ΔR and the resistance noise, one can locate the domain wall in this sample to about 10 nm.

the superconductor to study only the notch area.

The results from this modified sample were again better, but still unsatisfactory. Again, non-reproducible results were shown. However, there were indications that the samples did exhibit some behavior of domain wall trapping. As shown in Figure 4.7, there is a wide plateau located in equivalent spots on opposite sides of the hysteresis loop. There are still smaller plateaus located seemingly at random. The largest steps, though, are located in proportion to where the square contact is situated in the notch.

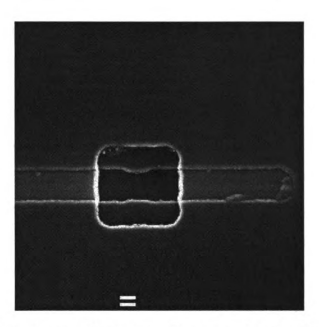


Figure 4.8: An SEM picture of a Type-IV sample. Notice that the top contact (square) is off center. The location of the notch in top contact region determines where the intermediate state will occur in the MR transition.

Note that the location of the large intermediate state is not half way in between the P and AP states. This is in agreement with the observation that the top contact is not perfectly centered over the notch, as shown in Figure 4.8. Furthermore one can estimate from the data of Figure 4.7 that the standard deviation of the resistance noise is $\sim 240~\rm n\Omega$. As the wall sweeps through the region of the 5- μm contact, the overall resistance change in R is $\Delta R = 0.12~\rm m\Omega$. Thus one can resolve the motion of the wall to $\sim 10~\rm nm$ (= 5 $\mu m \times 240~\rm n\Omega$ / 0.12 mΩ). Of course, further averaging of R measurements would improve the ability to resolve small motions in the average position of the wall. Also making the contact smaller should improve the resolution. In Figure 4.7, the quantity ΔR_{notch} (= 0.12 mΩ) provides an estimate of the average motion of the wall while it is trapped. One obtains $\sim .5~\mu m$ (= 5 $\mu m \times 0.012~\rm m\Omega$ / 0.12 mΩ) which is 50% of the neck length in the sample (Figure 2.3), a very reasonable result.

4.3 E-beam Lithography Samples

Since photolithography had been pushed to its resolution limits with the contact aligner, the patterning process was adapted to an electron beam procedure. Now a bilayer resist was used to pattern an Al mask on the sample. That mask shaped the multilayer by ion milling, and the entire substrate was planarized with SiO. In addition, since the size of the samples was approaching sub-micron dimensions, the geometry of the sample was changed to eliminate vias. The sample was instead initially sputtered with a very thick top Au layer (150 nm) that protrudes from the insulating layer. Contact will then be much easier to achieve with the top superconducting Nb.

Initially samples exhibited significantly increased coercive fields, similar to the EBSV transport study of Chapter 3. However, this problem was significantly reduced by improving the thermal contact between the substrate and its copper heat sink during ion milling and SiO deposition. Thermal grease was placed between the substrate and a blank Si substrate in the sample holder to ensure good thermal anchoring. Also, the blank Si substrate had grease applied between it and the Cu heat sink. This arrangement was successful in reducing the damage to the samples. The grease was removed by ultrasonic agitation in an acetone bath.

Also the layout of the sample was changed (Figure 4.9). E-beam lithography allows flexibility in the geometry of the exposure, and the previously mentioned improvements in domain wall injection [42, 43] were incorporated into the design. In addition, the size of the sample has now shrunk to a size where experiments done before have shown domain wall trapping in Ni₈₄Fe₁₆, so that material may be used again in an EBSV.

This procedure was successful in producing 1 and 2 μ m wide geometries. The results were promising. As shown in Figure 4.10 and 4.11, a single major plateau is usually observed in each transition from the P to AP state and vise versa in a Ni₈₄Fe₁₆EBSV with $t_{Py}=12$ nm. The plateaus are now more reproducible and appear

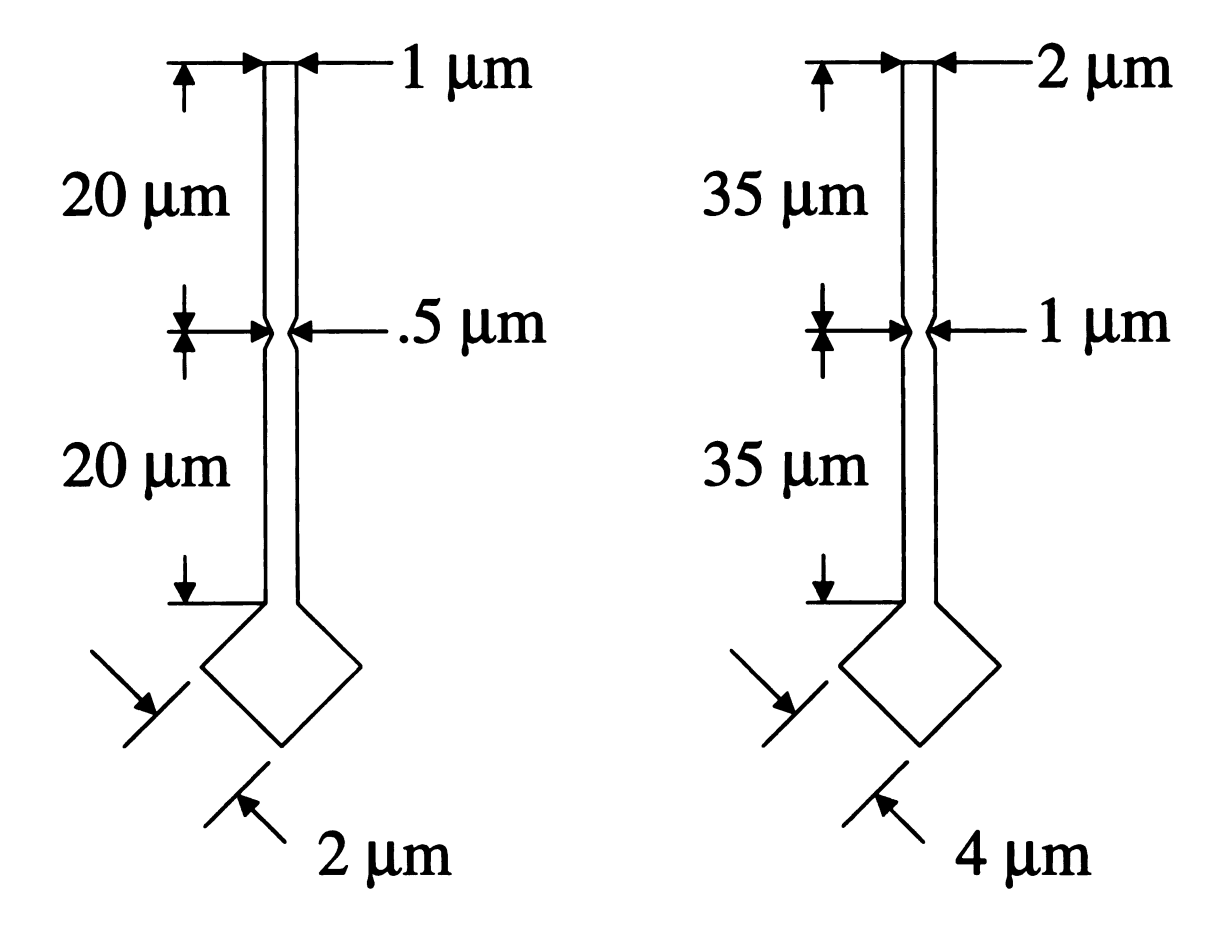


Figure 4.9: The pattern for e-beam lithographed samples. A diamond at the end of each wire is patterned to provide a source of domain wall injection. The aspect ratio of each wire has also been increased to facilitate single domain wires. Ideally the wide wire would have 40 μ m segments, but the pattern would exceed the range of the writing microscope.

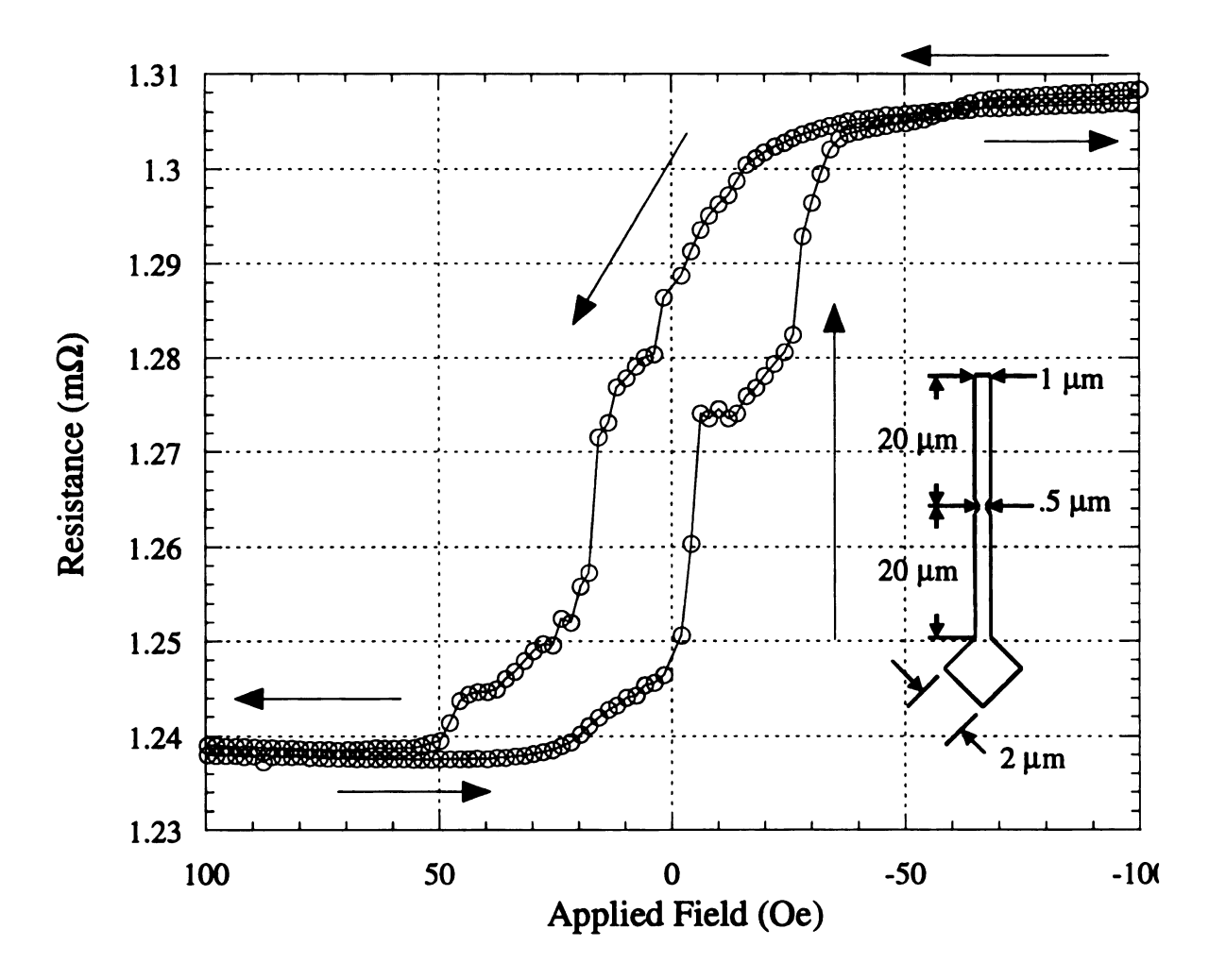


Figure 4.10: A single MR curve for a $Ni_{84}Fe_{16}EBSV$ ($t_{Py}=12$ nm). Notice the intermediate state located nearly at the half way point.

at a point halfway between the P and AP state, as expected. Note that the top Nb contact covers the whole sample, so the CPP-MR is sensitive to domain wall motion everywhere. In spite of this, it is gratifying to see plateaus at the expected intermediate position. Also note the area of the diamond-shaped pad is only 10% of the total area of the narrow wire.) It appears that this particular size of sample will yield the results desired (Figure 4.11). However, only by restricting the measurements to the notch region can fully realize the potential of this experiment be fully realized.

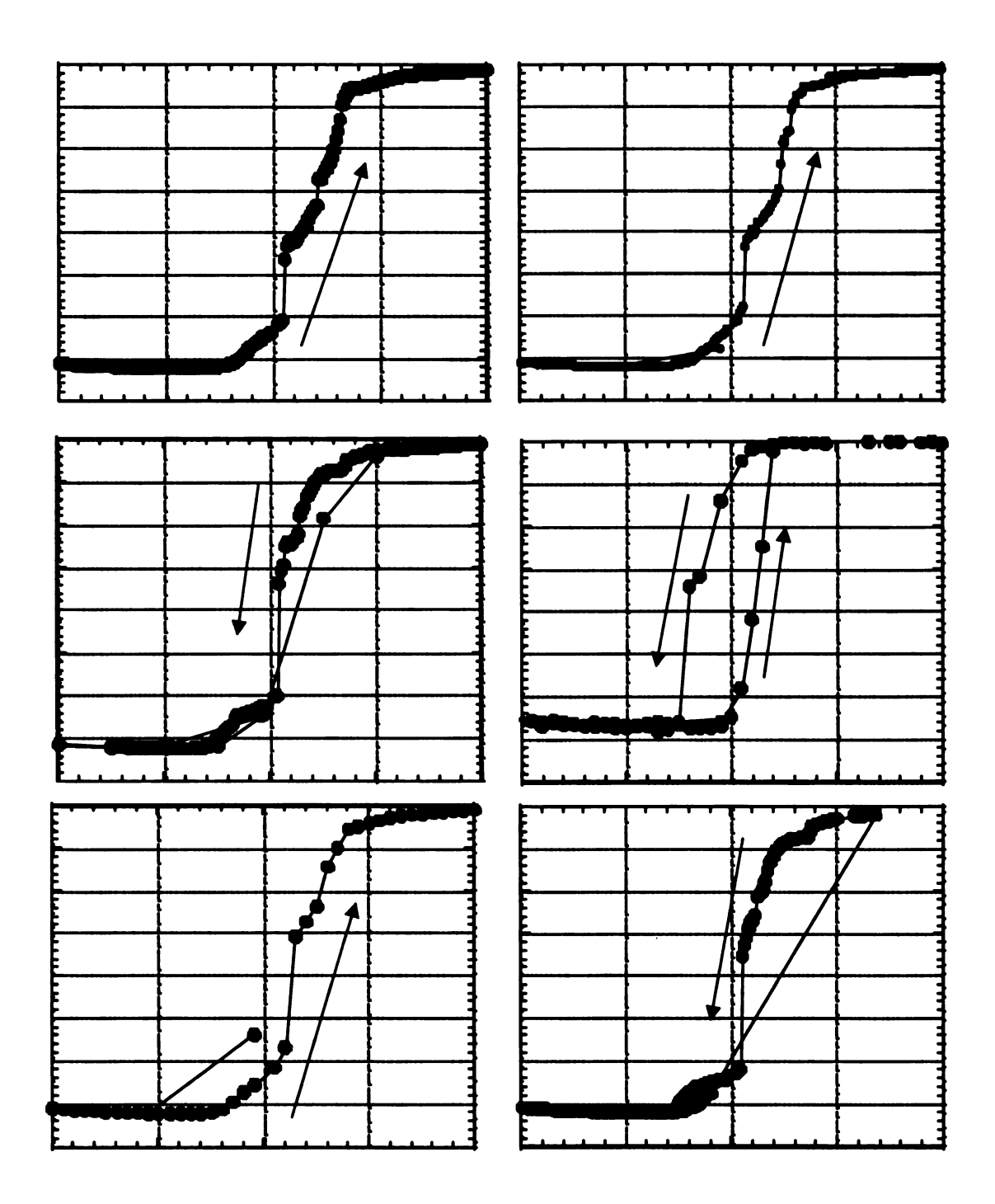


Figure 4.11: Repeated MR curves for a single sample 1 μ m wide (Py EBSV with t_{Py} = 12 nm). The trapping appears reproducible. Complete curves were not obtained in some cases due to problems with the electronics.

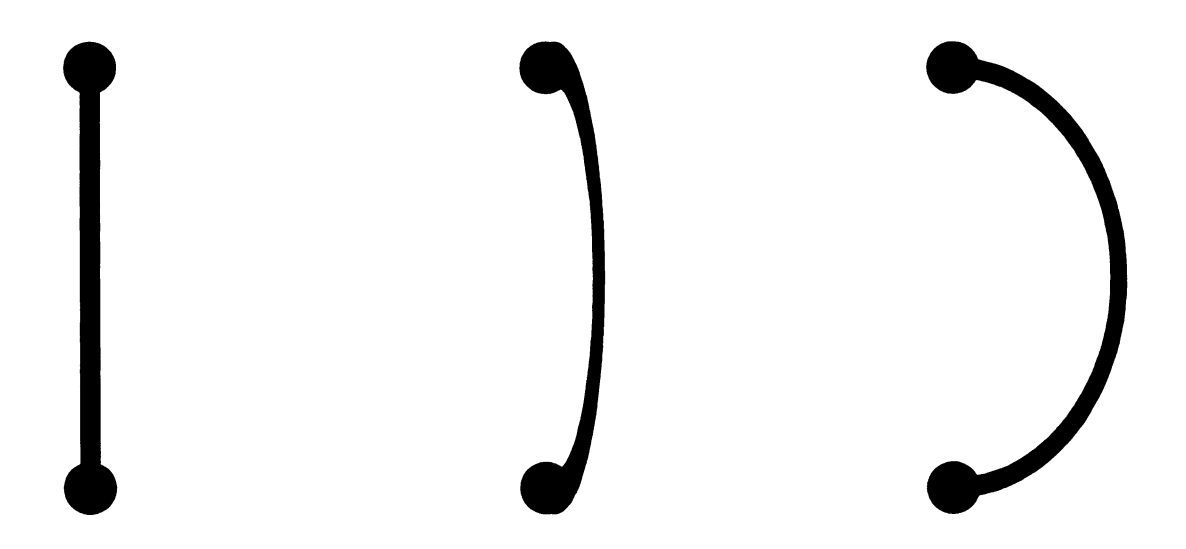


Figure 4.12: The motion of a domain wall (grey) after it becomes pinned by defect or geometry (black circles). The ends of the wall tend to stay fixed while the center will bow out.

4.4 Results

For all the results one thing is clear. When the intermediate state is achieved, this state is not 'flat,' but instead the resistance continues to change in same direction as before, usually at a lesser rate as the field is changed. This could be due to bowing of the domain wall. When a domain wall becomes trapped in the notch, the ends are very strongly pinned while the center will move forward (Figure 4.12). This will lead to the effect described above.

For the larger samples there also appeared to be multiple domains. Co is likely to become single domain only at large aspect rations [44]. From the information in this paper, it is unlikely that the photolithography samples patterned for this study were single domain. However, the e-beam samples are of the proper size and aspect ration to be single domain. Given the problems associated with photolithography at this resolution, it is probably best to continue the e-beam study and develop a method to place top Nb contact only in certain regions.

Chapter 5: Conclusions

A successful attempt was made to fabricate samples with areas of CPP current flow down to the micron size using superconducting contacts, but with macroscopic sizes for the ferromangetic layers. The sample properties were relatively unchanged. Although the coercive and saturation fields for some samples were increased, these changes can be minimized by refined techniques described here. The CPP GMR for both $Co_{91}Fe_{9}$ and $Ni_{84}Fe_{16}$, two materials important for applications, is unchanged in the samples with micron size contacts. The samples showed excellent P and AP states down to $4 \ \mu m^{2}$ top contact sizes. Although it may be possible to push the lithography further by adopting a larger wafer size to ensure a more uniform resist when spinning, the results may only give an improvement in resolution of less than 50%. It would be better, if further studies are needed, to adopt the electron beam techniques described for the domain wall trapping to produce top Nb contact sizes down into the sub-micron range.

The study of domain wall trapping is only in its infancy. Now that a reliable method for producing samples exits, further studies of the behavior of the domain wall can be done. From the initial Co₉₁Fe₉ work done with photolithography, it is clear that domain wall trapping was occurring to varying degrees. For the final electron-beam fabricated sub-micron wires, it is fairly clear that more reproducible trapping is occurring.

The final step in this process in to perfect a technique to place the Nb only in the notch region using e-beam lithography. Then it would be possible to gain further insight into domain wall trapping by controlling the shape and position of the notch. It has also been proposed to look for telegraph noise in the CPP-MR while the domain wall is trapped, a possible signature of domain wall tunnelling between pinning sites. Now that a procedure exists to produce samples, these studies can be done. So far in

this project no magnetic force microscopy (MFM) studies of the trapped walls have been made. This will be an important study to do for the future.

To accomplish this goal a new sample design (Figure 5.1) is proposed. By using a new photomask layout along with e-beam alignment, one should be able to select the areas of the wire to be studied and have only $\sim 1~\mu\text{m}$ -wide Nb top contacts (Figure 5.1.)

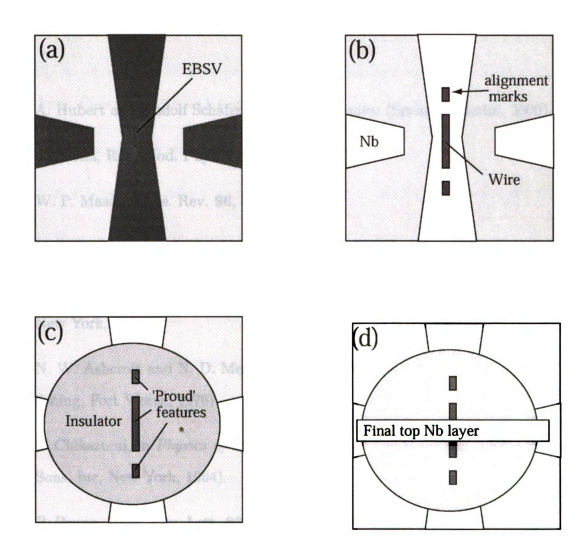


Figure 5.1: A proposed top view of the new fabrication to put Nb only in certain areas of the sample. (a) Photolithography patterned leads are made by sputtering an entire EBSV onto a substrate photoresist mask. The mask allows features down to several μ m to be patterned. Note: extensions of these patterned leads to mm size contact pads are not shown here. (b) Using the unattached leads as rough alignment marks, a wire mask feature is patterned on the center lead by e-beam lithography. The sample is then ion milled to the bottom Nb (Au coated) leaving the EBSV structure only underneath the mask (including alignment marks). (c) The sample is planarized. (d) The alignment marks are used to align a pattern (photo- or e-beam lithography) that will expose the notch region and a connection to the remaining leads. Sputtering Nb into the exposed region completes the sample.

Bibliography

- [1] A. Hubert and Rudolf Schäfer, Magnetic Domains (Springer, Berlin, 2000).
- [2] C. Kittel, Rev. Mod. Phys. **21**, 541 (1949).
- [3] W. P. Mason, Phys. Rev. **96**, 302 (1954).
- [4] M. I. Darby and E. D. Isaac, IEEE Trans. Magn. 10, 259 (1974).
- [5] C. Kittel, Introduction to Solid State Physics, 7 ed. (John Wiley & Sons, Inc, New York, 1996).
- [6] N. W. Ashcroft and N. D. Mermin, Solid State Physics (Saunders College Publishing, Fort Worth, 1976).
- [7] S. Chikazumi, in *Physics of Magnetism*, edited by S. H. Charap (John Wiley & Sons, Inc, New York, 1964).
- [8] P. Bruno, Phys. Rev. Lett. 83, 2425 (1999).
- [9] T. Ono, H. Miyajima, K. Shigeto, and T. Shinjo, Appl. Phys. Lett. 72, 1116 (1998).
- [10] T. Ono et al., J Appl. Phys. 85, 6181 (1999).
- [11] M. N. Baibich et al., Phys. Rev. Lett. 61, 2472 (1988).
- [12] G. Binasch, P. Grünberg, F. Saurenbach, and W. Zinn, Phys. Rev. B 39, 4828 (1989).
- [13] S. S. P. Parkin, N. More, and K. P. Roche, Phys. Rev. Lett. 64, 23042307 (1990).

- [14] W. P. Pratt, Jr. et al., Phys. Rev. Lett. 66, 3060 (1991).
- [15] S.-F. Lee et al., Phys. Rev. B 52, 15426 (1995).
- [16] M. A. M. Gijs, J. B. Giesbers, S. K. J. Lenczowski, and H. H. J. M. Janssen, Appl. Phys. Lett. 63, 111 (1993).
- [17] W. Vavra et al., Appl. Phys. Lett. 66, 2579 (1995).
- [18] J. A. Katine, F. J. Albert, and R. A. Buhrman, Appl. Phys. Lett. 76, 354 (2000).
- [19] L. Piraux et al., Appl. Phys. Lett. 65, 2484 (1994).
- [20] A. Blondel, J. P. Meier, B. Doudin, and J.-P. Ansermet, Appl. Phys. Lett. 65, 3019 (1994).
- [21] K. Liu, K. Nagodawithana, P. C. Searson, and C. L. Chien, Phys. Rev. B 51, 7381 (1995).
- [22] M. C. Cyrille et al., Phys. Rev. B 62, 3361 (2000).
- [23] J.-E. Wegrowe et al., Phys. Rev. Lett. 82, 3681 (1999).
- [24] T. Valet and A. Fert, Phys. Rev. B 48, 7099 (1993).
- [25] A. Fert, J. Duvail, and T. Valet, Phys. Rev. B 52, 65136521 (1995).
- [26] J. Bass and W.P. Pratt, Jr., J. Magn. Magn. Mater. 200, 274 (1999).
- [27] M. A. M. Gijs and G. E. W. Bauer, Adv. Phys. 46, 285 (1997).
- [28] A Barthélémy, A. Fert, and F. Petroff, Giant Magnetoresistance in Magnetic Multilayers (Elsevier, New York, 1999).
- [29] C. Fierz et al., J. Phys.: Condens. Matter 2, 9701 (1990).
- [30] J. Y. Gu, R. D. Slater, and William P. Pratt, Jr., unpublished.

- [31] J. M. Slaughter, W. P. Pratt, Jr., and P. A. Schroeder, Review of Scientific Instruments 60, 127 (1989).
- [32] D. J. Adelerhof et al., Physica C 209, 477 (1993).
- [33] K. Eid, R. D. Slater, and J. A. Caballero, unpublished.
- [34] L. I. McCann, unpublished.
- [35] E. H. Blevis, R. D. Mathis Comapny.
- [36] R. D. Slater, personal conversations with JOEL Tech Support.
- [37] R. D. Slater, J. A. Caballero, R. Loloee, and W. P. Pratt, Jr., J Appl. Phys. Accepted, December (2001).
- [38] A. Reilly et al., J. Magn. Magn. Mater. 195, L269 (1999).
- [39] M. Oonk, Master's thesis, Michigan State University, 1997.
- [40] S. D. Steenwyk et al., J. Magn. Magn. Mater. 170, L1 (1997).
- [41] L. Vila et al., J Appl. Phys. 87, 8610 (2000).
- [42] K. Shigeto, T. Shinjo, and T. Ono, Appl. Phys. Lett. 75, 2815 (1999).
- [43] K. S. T. Okuno, T. Shinjo, Y. Suzuki, and T. Ono, J Appl. Phys. 88, 6636 (2000).
- [44] E. Seynaeve et al., J Appl. Phys. 89, 531 (201).
- [45] J. A. Caballero, unpublished notes.

